UNIVERSITY OF CALIFORNIA, SAN DIEGO

Biological Applications of Synthetic Nanomachines

A dissertation submitted in partial satisfaction of the requirements for the degree
Doctor of Philosophy

in

Bioengineering

by

Daniel Robert Kagan

Committee in charge:

Professor Michael J. Heller, Chair
Professor, Joseph Wang, Co-Chair
Professor Sadik C. Esener
Professor Xiaohua Huang
Professor Andrea Tao
Professor Liangfang Zhang

2012

The Dissertation of Daniel Robert Kagan is approved, and it is acceptable in quality and form for publication on microfilm and electronically:

_____

_____

_____

_____

_____

Co-Chair

_____

Chair

University of California, San Diego

2012

DEDICATION

This dissertation is dedicated to my loving parents, Daniel Ralph Kagan and Susan Carol Kagan, and brother Kristopher Ryan Kagan who have made countless sacrifices so I could freely pursue my dreams. And to my future wife, Kelly Elaine Nugent, for her love, support and understanding through all of my struggles and successes.

EPIGRAPH

"The federal government has sponsored research that has produced a tomato that is perfect in every respect, except that you can't eat it. We should make every effort to make sure this disease, often referred to as 'progress', doesn't spread."

Andy Rooney

TABLE OF CONTENTS

LIST OF FIGURES

LIST OF TABLES

LIST OF VIDEOS

ACKNOWLEDGEMENT

First, I would like to thank Professor Joseph Wang for his advice, and support which made my dissertation possible. His enthusiasm and persistence have inspired me and have allowed me to accomplish more than I ever would have expected as a graduate student. I would like to also thank my Chair Professor Michael Heller for his advise, support and help throughout my graduate school classes and dissertation.

During my time in Dr. Wang's Lab, I have been fortunate to have collaborated and worked with so many great graduate students, post-docs, faculty members and undergraduate students. Many of these people I have been fortunate to publish with and I will acknowledge them all at the end. I would like to give a special thanks to a few specific individuals who were especially instrumental in my development and this dissertation. First and foremost, I would like to thank Dr. Shankar Balasubrumanian a great friend, colleague, mentor, and teammate who was instrumental in discussing many great ideas and helping to see them to fruition. I would like to thank Dr. Susana Campuzano, a bright, energetic and hard working future scientistic leader who helped with all the bioisolation projects and is amazing with anything that needs functionalization. I would like to acknowledge my fellow graduate students Wei Gao and Joshua Windmiller whose wisdom have made me a better scientist. I would also like to thank graduate students (Michael Benchimol, Corbin Clawson, Che-Ming Jack Hu, Adam Young, Ludovic Vincent, and Nikhil Rao) for collaborating on several projects even though not all succeeded. Finally, I would like to thank all of the undergraduates that I have helped advise (Maria Zimmerman, Maria Cardona, Dae

Kang, Nicole Lim, Beke Chuluun, and Rodger Yuan,); they all have promising careers ahead and I have learned more from them than I could ever give back.

Separately, I would like to thank the Siebel Foundation for the financial and networking resources and support over the past year and the Bioengineering department at UCSD, its faculty and administration staff.

Chapter 1 is based, in part, on the material as it appears in Analyst, 2011, by Susana Campuzano, Daniel Kagan, Jahir Orozco, and Joseph Wang; in part on material from Small, 2009, by Shankar Balasubramanian, S., Daniel Kagan, Kalian Manesh, Percy Calvo-Marzal, Gerd Flechsig, and Joseph Wang; in part on material from Chemical Communications, 2009, by Percy Calvo-Marzal, S., Kalian Manesh,Daniel Kagan, Shankar Balasubramanian, and Joseph Wang; and in part on material from ACS Nano, 2009, by Kalian Manesh, Maria Cardona Rodger Yuan, Michael Clark, Daniel Kagan, Shankar Balasubramanian, and Joseph Wang. The dissertation author was the primary investigator and co-author of these papers.

Chapter 2.1 is based, on the material as it appears in JACS, 2009, by Daniel Kagan, Percy Calvo-Marzal, Shankar Balasubramanian, Sirilak Sattayasamitsathit, Kalian Manesh, Gerd Flechsig and Joseph Wang; and Chapter 2.2 is based on material from Nature Communications 2009, by Shankar Balasubramanian, Daniel Kagan, Kalian Manesh, Percy Calvo-Marzal, Gerd Flechsig, and Joseph Wang; in part on material from Chemical Communications, 2010, by Jie Wu, Shankar Balasubramanian, Daniel Kagan, Kalian Manesh, Susana Campuzano, and Joseph

Wang. The dissertation author was the primary investigator and co-author of these papers.

Chapter 3.1 is based on the material as it appears in Nanoletters, 2011, by Daniel Kagan, Susana Campuzano, Shankar Balasubramanian, Filiz Kuralay, Gerd Flechsig, and Joseph Wang; Chapter 3.2 is based on the material as it appears in Nanoletters, 2012, by Susana Campuzano, Jahir Orozco, Daniel Kagan, Maria Guix, Wei Gao, Sirilak Sattayasamitsathit, Jonathon Claussen, Arben Merkoçi, and Joseph Wang, J.; Chapter 3.3 is based on the material as it appears in Angewandte Chemie, 2011, by Shankar Balasubramanian, Daniel Kagan, Jack Hu, Susana Campuzano, Maria Jesus Lobo-Castañon, Nicole Lim, Dae Kang, Maria Zimmerman, Liangfang Zhang, and Joseph Wang,; Chapter 3.4 is based on the material as it appears in Analyst, 2011, by Jahir Orozco, Susana Campuzano, Daniel Kagan, Ming Zhou, Wei Gao, and Joseph Wang, The dissertation author was the primary investigator and co-author of these papers.

Chapter 4.1 is based on the material as it appears in Small, 2010, by Daniel Kagan, Rawiwan Laocharoensuk, Maria Zimmerman, Corbin Clawson, Shankar Balasubramanian, Dae Kang, Daniel Bishop, Sirilak Sattayasamitsathit, Liangfang Zhang, and Joseph Wang; Chapter 4.2 is based on the material as it appears in Small, 2012, by Wei Gao, Daniel Kagan, On Shun Pak, Corbin Clawson, Susana Campuzano, Beke Chuluun-Erdene, Eric Shipton, Eric Fullerton, Liangfang Zhang, Eric Lauga, and Joseph Wang; Chapter 4.3 is based on the material submitted to Nature Nanotechnology, 2012, by Daniel Kagan, Mike Benchimol, Jonathan

Claussen, Beke Chuluun-Erdene, Sadik Esenser, and Joseph Wang. The dissertation author was the primary investigator and co-author of these papers.

Chapter 5 is part based in on the material as it appears in Angewandte Chemie, 2011, by Daniel Kagan, Shankar Balasubramanian, and Joseph Wang, and in part based on material submitted to Nature Nanotechnology, 2012, by Daniel Kagan, Mike Benchimol, Jonathan Claussen, Beke Chuluun-Erdene, Sadik Esenser, and Joseph Wang. The dissertation author was the primary investigator and co-author of these papers.

VITA

2006	Bachelor of Science, Rutgers University
2010	Master of Science, University of California, San Diego
2012	Doctor of Philosophy, University of California, San Diego

PUBLICATIONS

* Denotes Equal Contribution

1. Campuzano, S.; Orozco, J.; Kagan, D.; Guix, M.; Gao, W.; Sattayasamitsathit, S.; Claussen, J.; Merkoçi, A.; Wang, J.; Bacterial Isolation by Lectin-Modified Microengines. *Nano Letters.* **DOI:** 10.1021/nl203717q

2. Gao, W. *; Kagan, D. *; Pak, O. S.; Clawson, C.; Campuzano, S.; Chuluun-Erdene, E.; Shipton, E.; Fullerton, E. E.; Zhang, L.; Lauga, E.; Wang, J. Cargo-Towing Fuel-Free Magnetic Nanoswimmers for Targeted Drug Delivery." *Small,* **2011**, DOI: 10.1002/smll.201101909.

3. Campuzano, S.; Kagan, D.; Orozco, J.; Wang, J. Motion-based Sensing and Biosensing using Electrochemically-Propelled Nanomotors. *Analyst*, **2011**,*136,* 4621-4630.

4. Orozco, J. *; Campuzano, S. *; Kagan, D. *; Ming, Z. *; Gao, W.; Wang, J. Dynamic Isolation and Unloading of Target Proteins by Aptamer-Modified Microtransporters. *Anal. Chem.*, **2011**, *83*, 7962-7969.

5. Kagan, D.*; Campuzano, S.*; Balasubramanian, S.*; Kuralay, F.; Flechsig, G.-U.; Wang J. Functionalized Micromachines for Selective and Rapid Isolation of Nucleic Acid Targets from Complex Samples. *Nano Letters.* **2011**, *11*, 2083-2087.

6. Balasubramanian, S.*; Kagan, D.*; Hu, C. J.; Campuzano, S.; M. Jesus Lobo-Castañon, Lim, N.; Kang, D. Y.; Zimmerman, M.; Zhang, L.; Wang, J. Micromachine-enabled capture and isolation of cancer cells in complex media. *Angew. Chem. Int. Ed.* **2011**, *50*, 4161-4164.

7. Kagan, D*, Balasubramanian, S.*, Wang, J. Chemically Triggered Swarming of Gold Microparticles. *Angewandte Chemie,* **2011**, *50*, 503-506.

8. Kagan, D.; Laocharoensuk, R.; Zimmerman, M.; Clawson, C.; Balasubramanian, S.; Kang, D.; Bishop, D.; Sattayasamitsathit,S.; Zhang, L.; Wang, J. Rapid Delivery of Drug Carriers Propelled and Navigated by Catalytic Nanoshuttles. *Small* **2010**, *6*, 2741–2747.

9. Wu, J.; Balasubramanian, S.; Kagan, D.; Manesh, K. M.; Campuzano, S.; Wang, J. Motion-Based Sensing of DNA. *Nat. Commun.* **2010** 1:36 doi: 10.1038/ ncomms1035.

10. Manesh, K.M.; Cardona, M.; Yuan, R.; Clark, M.; Kagan, D.; Balasubramanian, S.; Wang, J; Template-Assisted Fabrication of Salt-Independent Catalytic Tubular Microengines. *ACS Nano*, **2010**, *4*, 1799-1804.

11. Kagan, D.; Calvo-Marzal, P.; Balasubramanian, S., Sattayasamitsathit, S.; Manesh, K. M.; Flechsig, G.; Wang, J.; Chemical Sensing based on Catalytic Nanomotors: Motion-based Detection of Trace Silver. *J. Am. Chem. Soc.* **2009**, *131,* 12082–12083.

12. Calvo-Marzal, P.; Manesh, K. M.; Kagan, D.; Balasubramanian, S.; Cardona, M.; Flechsig, G.; Posner, J.; Wang, J.; Electrochemically-Triggered Motion of Nanomotors. *Chem. Comm.* **2009**, *n/a*, 4509–4511

13. Balasubramanian, S.; Kagan, D.; Manesh, K. M.; Calvo-Marzal, P.; Flechsig, G.; Wang, J. Thermal Modulation of Nanomotor Movement. *Small.* **2009**, *5,* 1569–1574.

14. Zhang, K.; Kagan, D.; DeBois, W.; Robinson, R.; Bliskovsky, V.; Vass, W.; Zhang, S.; and Mock, B. Mndal, a new interferon-inducible family member, is highly polymorphic, suppresses cell growth, and may modify plasmacytoma susceptibility. *Blood.* **2009**, *114,* 2952-60.

15. Kagan, D.*; Benchimol, M.*; Claussen, J.*; Chuluun-Erdene, E.; Esesner, S.; Wang, J.; Ultrasound Triggered Microbullets for Tissue Penetration. In Preparation.

FIELDS OF STUDY

Major Field: Bioengineering and Nanoengineering

Studies in Bioengineering and Nanoengineering
Professor Joseph Wang

ABSTRACT OF THE DISSERTATION

Biological Applications of Synthetic Nanomachines

by

Daniel Robert Kagan

Doctor of Philosophy

University of California, San Diego, 2012

Professor Michael J. Heller, Chair
Professor Joseph Wang, Co-Chair

The field of synthetic nano/microscale propulsion devices has been rapidly expanding because of their ability to possess many key features necessary for bioanalytical applications on biological microchip devices and targeted *in vivo*

delivery. Past studies focused on developing powerful and easily controllable motors by investigating different propulsion schemes (e.g. electrophoretic, bubble release, magnetically propelled) for use in physiological environments. These engineering advancements and the nanomotors inherit capabilities have allowed for their use in three research areas: motion-based biosensing, cellular and biomolecular isolation, and targeted drug delivery.

The first research area investigates a unique speed increase of electrophoretically propelled nanomotors when in the presence of silver ions. Au/Pt nanomotors propel by the electrocatalytic decomposition of H_2O_2 fuel. While most metal ions resulted in a decrease in speed to near Brownian levels, Ag^+ has shown a steady increase in speed from 10μm/s to 52μm/s over the micro-molar range. This phenomenon was exploited by tagging nucleic acid detector probes with Ag nanoparticles when conducting simple sandwich assays. This resulted in a cheap, fast, and sensitive, motion-based readout of the concentration-dependent DNA target present on the sandwich assay.

The second area of research involved the bioisolation of nucleic acids, protein, bacteria, and cancer cells by bubble-based microrockets. These microrockets contain a platinum interior to catalyze peroxide fuel and can be easily functionalized with antibodies and nucleic acid capture probes to isolate target biomolecules. The motion of these micro-isolation devices creates convection for faster isolation and can be used to transport the biomolecules to a clean environment.

The third area of research is focused on targeted drug delivery by various

propulsion methods. The ability of nanomotors to transport PLGA and liposome drug vesicles to cancer cells is shown *in vitro*. A powerful ultrasound-triggered propulsion mechanism is used to fire microscale bullets through various tissues, which is necessary for more advanced delivery methods.

Future experiments including modeling the behavior the micro-isolation devices, developing collective behavior nanomotor schemes, and using ultrasound microbullets for *in vivo* bladder cancer studies are still necessary to develop true commercial applications from this promising field.

Chapter 1 Introduction

1.1 Biomotors: The Foundation of the Nanomotor Field

Many people contribute Richard Feynman's Caltech speech "There is plenty of room at the bottom," as the founding moment of the nanotechnology field. There he stated, "So I want to build a billion tiny factories, models of each other, which are manufacturing simultaneously, drilling holes, stamping parts.." Although his concept of nanomachines was novel in the 1960's, we fully understand now that biomotors in the body have been perfected for billions of years. For this reason many scientist have tried to harness the great power of nanoscale biomotor for use in larger analytical devices.[1]

There are currently dozens of different biomotors and hundreds of genes, which contribute to the creation of these machine-based protein structures.[2] The three major biomotors are myosin II, kinesin, and dynein, but only the first two have been heavily exploited for in.vitro applications. Viscous forces usually dominate over

inertia forces causing movement to result in very low Reynolds numbers due to their size and slow velocity. To provide directional movement and avoid complete Brownian motion, these biomotors move along set tracks such as microtubules (kinesins and dyneins) and actin (myosin). It is known that myosin, kinesin, and dynein have very similar features. Although the specific mechanism for movement along their respective filaments are different, movement in both causes results from small angstrom size changes in the converter domain resulting in nanometer size steps due to long lever arms. One key similarity of the three movements is that all convert biochemical energy in the form of Adenosine-5'-triphosphate (ATP) into mechanical energy through the use of ATP hydrolysis.[2]

One major difference between kinesin and myosin is that kinesins spends 90% of the time in the tightly bound state with two ends bound as it transports large vesicles to cellular organelles at a rate of 1-2um/s, while myosin spends only 5% of the time bound tightly while moving at a higher rate of 8 um/s. This is necessary as myosin often plays a role in cellular structure reorganization, which needs to be a fast process especially in muscle contraction. Overall, the speed and precision of these biomotors is necessary and crucial for the essential tasks like cellular restructuring, and vesicle transport.[2]

In order to move to the nano-level and many scientists have tried to harness the capabilities of these nanomotors for various *in. vitro* application. The use of biomotors has many advantages, which include the use of ATP, which is abundant and compatible in a biological environment as well as the ability to genetically alter them

and mass produce using common cloning techniques.[1] Additionally, Spetzer[3] discovered that motor proteins can produce minimal forces 5-4500 pN and when combined together can generate forces in the kNs, thus enabling them to transport large cargos. One of the first, most well-known instances of combining the biomotor mechanism with synthetic parts is seen in Carlo Montemagno's use of the F_1F_0 ATP synthase.[4] This membrane protein typically uses free energy from the electrochemical proton gradient across the membrane to synthesis cellular ATP from ADP and P producing 80% of the organisms usable energy. F_0 Component responsible for pumping protons across the membrane. The c-ring acts as a shaft to turn the $(aB)_3$ ring of F_1 domain which synthesis ATP. The $(aB)_3$ ring which makes up the F1 segment has three spots for ADP, ADP +P, ATP and rotates during ATP synthesis. When separated from F_0, F_1-ATPase acts in the opposite direction, thereby hydrolysing ATP and turning the (aB) ring in a rotary fashion. This generates 64 pN of torque and can be measured using the addition of a gold nanorod and looking at the light scattering as it changes with time.[5,6] These bio-synthetic hybrid nanopropellors offer many possibilities as a potential motor or nano-energy capturing or providing device.[7]

Biomotors (kinesin, myosin) have also been exploited in many recent purposes for a variety of *in.vitro* applications. One major use has been to create *in vitro* tracks for cargo transport in a Polydimethylsiloxane (PDMS) microfluidic device for the purpose of creating a biomotor-based Lab-on-Chip device. The immobilization of both microtubules and kinesin have been used, but an inverted motility assay involving the self-assembly of avidinated kinesin through controlled flow and the use of a

microtubule as carrying device is more commonly used.[2] One major reason for this is that microtubules make for a better carrying device since they have the ability to attach cargo all throughout there length. It have been demonstrated that a kinesin-coated PDMS surface can transport a fluorescently labeled microtubule randomly throughout the surface. Aggregated time-lapse images reveal that the microtubule has the inability to travel up the drastic incline present in the center circle thereby making this a potential topological graphing tool.[8] Past research has also show the ability to attach cargo to these microtubule transport devices by using streptavidin, antibodies, magnetic or DNA linkers. Using, biotin/streptavidin binding, biomolecules such as DNA, viruses, nanoparticles, bio/flourescent probes, and antigens have the ability to be picked up and transported.[9] Recently, Hess's group has shown how the movement of microtubules along a kinesin-coated PDMS track has enabled the on-the-go pickup, tag, and detection of antigens thereby removing the typical washing steps in a double antibody sandwich assay.[10] Additionally, cellular movement has also been exploited for developing microengines/turbines; a silicon rotor has been shown to be turned when adding glucose to the mycoplasma bacteria containing well; the bacteria's circular motion has been able to generate considerable torque will moving the at 2 rpm.[11]

One of the major challenges involving any nanomotor is the ability to properly control its speed and direction. One common way to control direction is through the patterning of kinesin along the PDMS. Speed has been generally controlled through genetically modifying the biomotor so that it can be stopped through an inhibitor (pH

or Ca^{2+} sensitive) or in the case of the F_1-ATPase, a nickel nanorod.[2,5] The development of temperature control kinesins have shown that at low temperature the polymer surface sterically interferes with kinesin and microtubule interactions. Additionally, the use of electric fields to direct positive end of microtubles to kinesin coated gold surface. The final way motion has been controlled has been through the use of activated fuel or caged-ATP.[9] Here, UV light is essential to cleave the aromatic ring on the ATP into a useable from necessary for the movement of kinesin. This UV control cases a start and stopping semi-reversible reaction changing the microtubule speed from 800 nm/s to 0.001 nm/s when not in the presense of UV light.

While biomotors have great potential, they have many current disadvantages in that they have a limited lifetime outside the body and can only work in a limited range of conditions similar to the body (pH, ionic strength, temperature). This makes it difficult for use in large scale *in vitro* applications. Additionally, their current utilization has been generally restricted *in vitro* applications as it would be hard to imagine patterning kinsein or laying down microtubles within an organism. Additionally, the biomotor speed has shown to be too slow (1-2 μm/s)[1,2,10] for many *in vivo* drug delivery applications. These disadvantages are some of the reasons why the Wang group and others have turned to synthetic nanomotors to fulfill Feynman's dream for multipurpose nanomachines.

1.2 Introduction to Synthetic Nanomotors and Propulsion Mechanisms

As stated in the last section, biomotors have many deficiencies, thereby opening the door to the development of synthetic nanomotors. The concept of small nanomotors where first introduced with Whitesides[12] millimeter scale microswimmers which move away from small oxygen bubbles formed as a result of the hydrolysis of hydrogen peroxide fuel. Since his 2002 publication, researchers have created many different types of nano/micromotors. As previously mentioned, the hydrodynamic regime in which nanomotors propel is characterized by a very low Reynolds number, a dimensionless parameter that refers to the relative scale of an object, its inertial forces (numerator) and the viscous forces (denominator). The Reynolds number is (Equation 1):

$$R = \frac{vL\rho}{\eta}, \qquad (1)$$

where *v* is the velocity of the fluid , L refers to the particle dimension, ρ is the specific gravity of the fluid, and η is its viscosity. Although dominating viscous forces primarily lead to Brownian motion, axial propulsion and controlled changes in momentum have been accomplished by a variety of complex/theoretical propulsion schemes as described below and seen in Figure 1.1.[13]

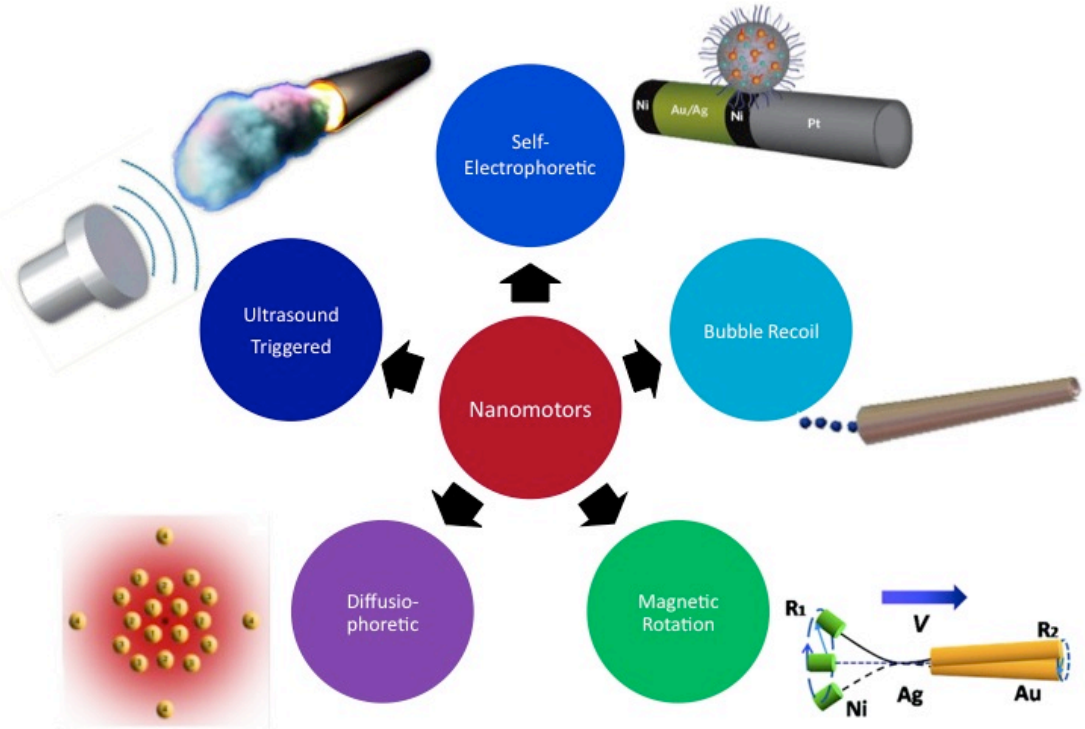

Figure 1.1 Figure schematically depicts the many different nano/micromotor propulsion schemes that researchers use to move in low Reynolds number environments.

Five major general mechanisms for propulsion will be introduced here, which pertain to the current and future projects described in Chapters 2-4. One of the first approaches was to explore the use of a fuel, mainly hydrogen peroxide, as a way to convert chemical energy to mechanical movement. The first method used and described here is self-electrophoresis. Similar to biomotors using the hydrolysis of ATP for movement, many synethic nanomotors have used the hydrolysis of H_2O_2 for its movement. The major difference is that biomotors exploit small protein

conformation changes after hydrolysis as a method for propulsion and nanowire motor. While a number of mechanism including an oxygen gradient (*e.g.* diffusiophoretic mechanism), bubble propulsion (refuted) and interfacial tension mechanism have been proposed for how multi-segment nanowire motors are propelled in H_2O_2, the below electrophoretic mechanism has been the most widely accepted. Under the proposed mechanism the platinum segment on the bi-catalytic nanomotor oxidizes the hydrogen peroxide forming both protons and electrons. The electrons are directionally conducted through the metal to the Au segment and used to aid the reduction of peroxide. It is believed that ion migration from the electrons and following protons would cause fluid flow in the interfacial region and a corresponding slip velocity, which ultimately is responsible for the motility of the self-electrophoretic object.[14-17]

The second complex mechanism used to describe the motion of nanomotors is the self-diffusiophoretic mechanism. This theoretical mechanism can be described as the movement of a nanoparticles/motors by the asymmetric catalysis or movement of the fuel contents. This mechanism is typically used to describe how a monocomponent Pt janus particle can move without the presence of another active metal.[18] Howse proposes that as long as the reaction provides more products than reactants consumed than the asymmetric surface on the particle will form a subsequent gradient in the interfacial region resulting in diffusion limited propulsion.[19,20] Furthermore, Sen[21] mentions how this mechanism can be used to explain non-Brownian movement when the products are ions. He suggests that if the products released are ionic in nature and diffuse at different rates, the possibility exists that a very localized ionic gradient can

form resulting in the electrophoretic movement of the particle. This mechanism has been further used to explain the swarming of Au particles in mixed fuel and could be critical to the development of collective behavior and smart motor schemes (See Chapter 5). One major drawback to these ion flow based mechanisms is their inherit limitation for use in high ionic strength environments. This limitation has been traditionally attributed to the shielding of ionic charges needed for constant propulsion by the surrounding ions in solution.

The third and easiest mechanism to understand is the use of bubbles to propel the nanomotor forward (Figure 1.1). Recently, Mei's[22,23] group has shown that by using this powerful technique that there microrockets can be propelled at speeds of 2 mm/s. The microengines are unidirectionally self-propelled by the recoiling of highly accumulated gas microbubbles produced on the inner catalytic Pt surface in the presence of peroxide. As the platinum (Pt) converts the peroxide to oxygen gas and water inside the microtube it forms oxygen bubbles which expand to the larger opening where they are ejected and released with a force dependent on the formation rate, and tubular aspect ratio, and surface tension. Due to the conservation of momentum the microbullets are propelled forward once the bubbles are released.[24] In order for this mechanism to be successful, the bubbles must be allowed to expand in the tube by use of a conical shaped tube thereby creating a larger bubble-drag force (used to propel the rocket after bubble release) than the tube drag force which correlates with the cross sectional area. It is understood that an optimum amount of surfactant is needed to release the bubble from the slightly hydrophobic platinum

surface. Too much surfactant, leads to bubbles smaller than the tubular diameter, and the subsequent smaller bubble drag force was shown to halt propulsion. One major advantage the bubble mechanism has is that it is salt independent. This attribute allows it to become applicable to biological-based in vitro assays as shown in Chapter 3. Additionally, it has been shown that this method is very versatile leading to similar microrocket bubbling strategies with different inner catalysts (catalase),[25] fuels (acids)[26] and sizes (ranging from 6 to 500 μms).[27]

The fourth mechanism, the magnetic field technique, differs from the previous methods because it is not fuel based. The use of a magnetic field based propulsion has been exploited in the asymmetrically cobalt covered SiO2, cork screws.[28] Through the use of complex Lab View programming, a tri-axial Helmholtz coil is used to generate a homogeneous magnetic field of ~50 Gauss rotating at frequencies of up to 170 Hz. which can be automated to drive the swimmer in all 3- dimensions.[28] This fuel-less approach possess many possibilities for future *in vivo* studies. Additional studies including ones by the Wang group have been able to use a simple rotating magnetic paired with a strategically placed, stationary block magnetic to provide directional and controlled nanowire motion.[29] This particular scheme exploits the asymmetric movement of the nanowire object, which arises from a flexible, peroxide treated, Ag segment. Further studies have been able to utilize a similar Helmholtz coil to continuously control and direct the movement of various nanowire motors containing a flexible segment.[30]

The newest propulsion mechanism, arising from a collaboration with the Wang and Esener groups of UC San Digo, is the acoustic droplet vaporization (ADV) method for using ultrasound to fire micromachines at ultrafast rates as if they were bullets.[31] This method demonstrates, for the first time, a nano/micromotor propulsion scheme with the power necessary to penetrate, deform, and cleave tissue —opening the door for targeted drug delivery and precision nanosurgery. It utilizes ultrasound/acoustic droplet vaporization, which directionally propels nano/microscale motors with high velocity and in a bullet-like fashion (*i.e.*, 100 times faster than the state-of-the-art with an average velocity of over 6 m/s), and it demonstrates the first use of an on-board fuel source in the form of biocompatible, perfluorocarbon emulsions specifically immobilized within the nano/micromotors — eliminating the need for external, chemical fuel sources (*e.g.*, hydrogen peroxide, HCl, hydrozine) that severely restrict use in real-world applications. In essence, ultrasound triggers the on board perfluorocarbon emulsions to instantly vaporize and expand out of the microrocket shape at such a fast rate that it shoots like a bullet. Many micromachine shapes and sizes can be considered for conducting ADV experiments since the emulsion type/size and ultrasound pulse length/power can easily be varied. This process is limited to the onboard fuel and in general we observed that the microbullet would only fire 2-3 times. Due to the medically safe, deeply penetrative, and clinically ubiquitous nature of ultrasound, it is likely that further use of ADV propelled devices could make a high impact on the medical field that could lead to highly targeted *in*

vivo drug delivery, artery cleaning, gene regulation schemes, and cancer therapeutics with higher specificity and accuracy than the current state-of-the-art technologies.

1.3 Advancements in Synthetic Nanomotors Design

Over the past ten years the field of nanomotors has started to grow rapidly averaging around 30+ papers a year. With the increase of interest has come many different nano/micrometer models using a variety of propulsion mechanisms as seen in the last section. Scientists have explored the use of using SiO_2 E-beam deposition,[28] Janus particles,[20] porous metal nanowire[18] and rotatory-based motors[32,33] and more. However, here we will go into greater detail regarding the nanomotors presently used in our laboratory. The use of bi-segment, Sen's catalytic nanowires24 is one of the first true nanomotors to be developed. As previously, mentioned these nanomotors use a self- electrophoretic mechanism to promote movement after catalytic decomposition of hydrogen peroxide fuel. The development of these wires is a creative approach, which yields millions of nearly identical wires per preparation. As seen in Figure 1.2, the catalytic nanomotors are prepared by electrodepositing the corresponding metals into an alumina membrane template (Whatman, Maidstone, U.K.).

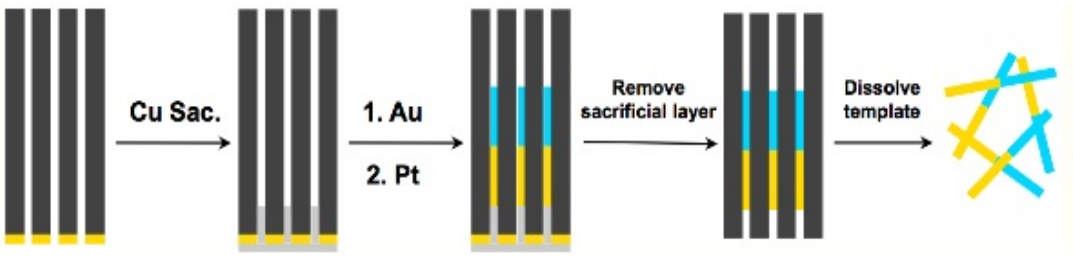

Figure 1.2 Schematic illustrating the steps involved in the template-based deposition of synthetic nanomotor wires into a polycarbonate or alumunia membrane.

In detail, the length of each nanomotor segment was obtained by controlling the electrodeposition charge, while its diameter (~220 nm) was predetermined by the pore size of the membrane. A thin gold film was first sputtered on the branched side of the membrane to serve as a working electrode. The membrane is assembled in a plating cell with aluminum foil serving as an electrical contact for the subsequent electrodeposition. In order to synthesize well-shaped cylindrical nanomotors, a sacrificial silver layer is electrodeposited into the branched area (~1-2 μm thickness) of the membrane using a silver plating solution (1025 RTU@4.5 Troy/Gallon; Technic Inc., Anaheim, CA). A total charge of 2 coulombs (C) at −0.9 V (vs. Ag/AgCl, reference electrode and using a Pt wire counter electrode) is plated using a potentiostat machine. This is followed by an electrodeposition of gold (1.5C) from a gold plating solution (Orotemp 24 RTU RACK; Technic Inc.) at −0.9 V (vs. Ag/AgCl) and the galvanostatic plating of platinum (Platinum Plating Solution RTP; Technic Inc) at −2 mA for 50 min. This typical process has been optimized to create 2 μm Au/Pt nanomotors using a 25mm alumina membrane. Other metals, and conductive polymers have been used to alter the content and function of these nanomotors and they require specific conditions. After plating, the Au sputtered layer is mechanically removed by polishing and the Ag sacrificial layer is dissolved in 35% Nitric Acid; finally, the alumina membrane is dissolved in 3M NaOH, thereby releasing the nanomotors from the membrane. Repeated centrifugation and wash cycles (D.I. Water) are conducted bringing the nanomotor containing solution to a neutral pH.[13,14,36]

This procedure is the basis for the development of the first catalytic nanowire motors used in Chapter 2. As previously mentioned these nanomotors use hydrogen peroxide decomposition and an electrophoretic mechanism for movement.[10] Using this fabrication method and propulsion mechanism, the Sen Group tested to see if combinations other catalytic transition metals would also lead to motion.[34] He tested bi-segment combinations of Rh, Pt, Ni, Pd, Au, Ru, Ag, and Co and discovered that average nanomotor speed directly correlated with the mixed potential difference between the two metals tested (Ru/Pt) showed the greatest difference and subsequent largest speed (30 um/s). Sen's group also discovered the nanomotor speed negatively correlates with ion concentration and that even 10 uM solutions of NaCl can result in the inhibition of movement. As previously mentioned, this phenomenon is most likely due to the ionic shielding and subsequent collaspe of the ionic flow which is said to propel these motors. Such an observation is very important as physiological conditions typically lie in the 150mM range, thereby making these nanomotors generally incompatible with most biomolecular or in.vivo experiments.[34,35]

Although bi-segment nanomotors have salt restrictions it is thought that faster, more powerful nanomotors could be used for *in vitro* applications like movement/transport in a lab-on-chip device.[2,16] Previous research in our group has shown that the incorporation of CNT into the Pt segment leads to an increase in the current density of that segment and an overall increase in the average nanomotor speed from 10 to 50 μm/s.[36] In a similar fashion to Sen's work, changing the metal content by using varying compositions of Ag/Au alloy concentrations, leads to varying

average nanomotor speeds of up to 75 μm/s.[37] Such motors were used for initial drug loaded vesicle towing experiments shown in Chapter 4.1

In addition, to changing the nanomotor composition scientists have tested using alternative fuels to affect both nanomotor speed and the environment in which they work in. The Wang group has also previously shown that the combination of using faster Au/(CNT/Pt) with Hydrazine/Peroxide fuel can increase the peroxide consumption rate and increase the overall nanomotor speed to 100um/s or an amazing 50 body lengths per second. In addition to changes in synthetic fuels, scientists have attempted to use biofuels as a way to control movement. Ideally, one long sought after mechanism would involve the consumption of glucose by glucose oxidase enzymes to produce peroxide which is then used by catalase to produce oxygen bubbles or ion flow.[38] As the body has a relatively high level of glucose this mechanism has much potential. Results from the below figure and similar experiments conducted in our lab have shown that the oxygen needed to form the peroxide is rate limiting inhibits movement in solution. However, in order for fuel-driven nanomotors to be successfully incorporated *in vivo*, other biological fuels need to be explored. One major challenge is that enzymes have evolved over time to prevent the production of bubbles, and are generally inactive for pH solutions where their products form bubbles as is the case with Urease enzyme.

Due to this innate salt inhibition problem, a bulk of the early experiments were designed to develop nano/microscale motors with different propulsion mechanisms. First, a simplified template-assisted layering approach for preparing catalytic conical

tube microjet engines based on sequential deposition of platinum and gold on an etched silver wire template followed by dicing and dissolution of the template was used (See Figure 1.3) The method allows for detailed control over the tube parameters and hence upon the performance of the microengine. The exact length and dimensions of the microcone are controlled by the dicing step, while the degree of concavity is controlled by the etching conditions (such as etching time and concentration of nitric acid). The conical shape of the wire template (after the nitric acid etching) is clearly indicated from the figure. Such concave geometry curvature minimizes the turbulent flow inside the micromotor and provides a favorable gradient for forward propulsion.[39] It also increases efficiency of the oxygen-bubble production and the overall controlled fluid flow. The recoiling bubble propulsion mechanism of the tubular microengine, associated with the ejection of internally generated oxygen microbubbles when in the presense of hydrogen peroxide fuel, and thereby addresses the ionic-strength limitation of catalytic nanowire motors, leading to a salt-independent movement. Similar rates of bubble generation (5 bubbles/s) and motor speeds (180-200 μm/s) were observed in salt-free and salt-rich (1 M NaCl) media when tested in 5% H_2O_2. Plating of an intermediate nickel layer also facilitated magnetically guided motion as well as the pickup and transport of large (magnetic) "cargo". Due to its large size (30 μm in diameter by 150 μm in length) the addition of surfactants only decreased the bubble size, preventing forward motion. This correlates to an average change of 5 degrees along the length. Minimizations in the length were

considered as we suspect the largest opposing force to the axial motion provided by the release of the bubble is the friction of the microrocket on the glass surface.

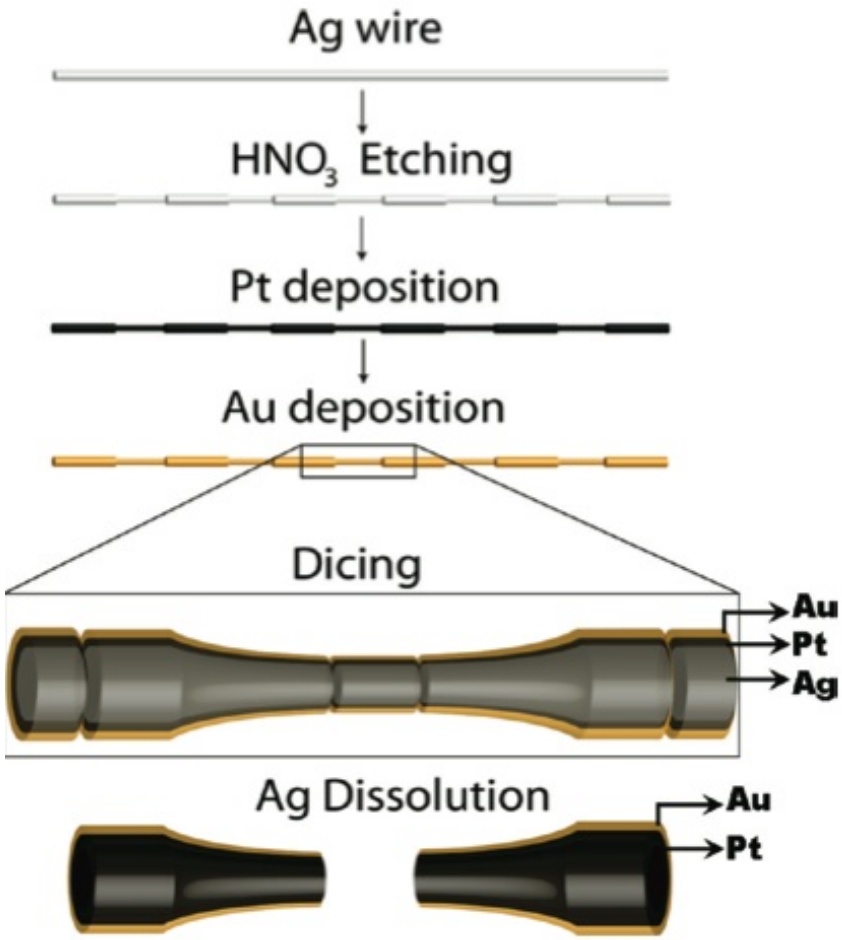

Figure 1.3 Schematic illustrating the steps involved in the template-assisted preparation of the tubular microcone engine. This scheme depicts a visual un- derstanding of the silver template preparation, electroplating of the Pt and Au layers, dicing of the coated wire, and dissolution of the silver template. Ni- tric acid dissolves the silver wire, creating concave geometry, which remains when Pt and Au are electroplated.

Although the template-based microrocket was relatively quick and easy to develop, it was hard to create multiple replicas and smaller scale motors (sub-cellular). Therefore much of the bioisolation experiments (presented in Chapter 3) have been

conducted using a modified protocal from the Schmidt laboratory (Figure 1.4).[22,23] It has been previously shown that these rockets can be mass produced and go at speeds up to 2mm/s using a bubble-based mechanism. As previously shown using the large template microrockets, a bubble-based mechanism using a Pt metal interior and peroxide fuel can be quite effective. In similar fashion, we were able to use a modified protocol to rolled-up tubular membranes by conducting sequential, angled electron beam deposition of Ti, Fe, Au, Pt (in order) onto a lithography patterned 2 μm thick photoresist. This works due to the inherit buildup of stress at the photoresist/metal interface due to the angled deposition. Upon the instant dissolution of the photoresist in an organic solvent, the raised and stressed metal instantly rolls-up. To prevent collapse and allow for the dissolution of remaining organics, critical point drying and additional ozone steps are performed. The rockets are then mechanically removed and ready to be used. Fortunately, this protocol can be optimized for size, shape, speed, and fuel efficiency by changing the photoresist thickness, the patterned shape, the amount of deposited material and angle that the metal is deposited on the substrate. Further optimization has led to microrockets ranging from 30-500 μm in length, and using as little at 0.2% fuel.[25] Additionally, by eliminating the interior Pt segment we were able to electrostatically bind perfluorocarbon emulsions to the Au interior; this was the foundation for the ultrasound-triggered microbullet experiments explained later in detail (Chapter 4.3).

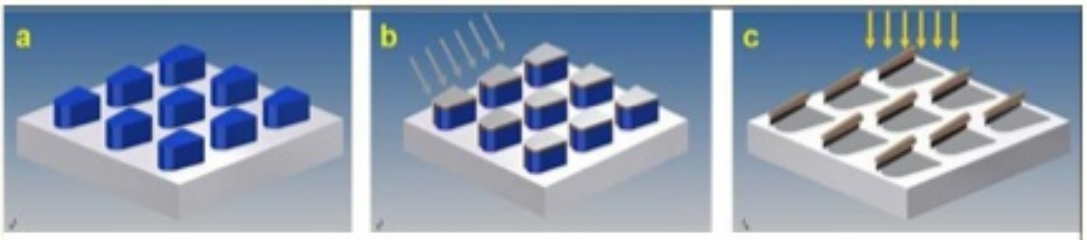

Figure 1.4 Schematic illustrating the steps involved in developing rolled up microtube engines (microrockets) including: photoresist lithography (a), angled electron beam deposition (b), and photoresist dissolution resulting in arrayed rolled up structures (c).

As shown in Chapter 3.4, the template and electron beam deposition approaches were further combined to develop ultrafast microrockets (up to 10 mm/s), which are under 10 μm in length and 1 μm in diameter. Microtube engines were prepared by electrodepositing sequential layers into a cyclopore polycarbonate membrane, which contains numerous double-cone-shaped micropores with a maximum diameter of 2 μm Standard electrodepostion of an outer PANI layer and inner Pt layer was conducted via a a similar 3-electrode set-up to that of the nanowire catalytic motors. In brief, A 75 nm gold film was first sputtered on one side of the porous membrane to serve as working electrode. PANI was electropolymerized onto the sides of the pores using a plating solution containing 0.1 M H_2SO_4, 0.5 M Na_2SO_4, and Pt was galvanostatically deposited for 3600 sec at a constant current of -2 mA using a commercial platinum plating solution. After electrodeposition, the gold film was removed by hand polishing with alumina nanoparticles. The membrane was then dissolved and repeatedly washed in methylene chloride, ethanol and ultrapure water. To add a magnetic layer, the wires solution were then evaporated onto glass slides before the sequential deposition of 10 nm Ti (adhesion layer), 26 nm Ni (magnetic layer). This last step did reduce the yield and average motor speed by half. While

these template motors have their advantages, often bio-applications require or benefit from larger motors.

Finally, with an ultimate goal of *in vivo* targeted delivery many researchers have focused on magnetically driven motors. As previously mentioned the core to developing a magnetic approach is it assymmetic spinning design. The nanowire motors used for drug delivery applications as shown in Chapter 4.2 are one of the fastest and most capable magnetically driven micromachines. They were prepared using the same template-directed electrodeposition protocol, in which a silver film (for working electrode) was first sputtered on one side of the porous alumina membrane before plating Cu (sacrificial), Au (protective and functionalizable), Ag (flexible) and Ni (magnetic) segments into a 200 nm-diameter cylindrical pores. The wires are then released from the membrane, the Ag is made flexible by peroxide incubation and the wires are repeatable washed. The resulting nanomotors have a single rigid 1.5 μm-long Ni segment, a 4 μm-long flexible silver segment and a 0.3 μm-long gold segment (for protecting the Ni), giving a total nanowire length of 5.8 μm. They are capable of moving up to 10 μm /s using a f = 10 Hz, H = 10 G, rotating magnetic Helmholtz coil. Although smaller in size and biocompatible, they are still not small enough to pass between cells and are not powerful enough to penetrate through tissues. For this reason, the lab is continuing to look at new propulsion mechanisms such as ultrasound-triggered (Chapter 4.3) for targeted drug delivery experiments.[40]

1.4 External Temporal and Spatial Control of Synthetic Nanomotors

In order to have viable applications, nanomotors must be able to be controlled both spatially and temporally. For this reason, our lab has used a number of techniques including potential, temperature, and magnetic fields to control both the speed and the direction. Sen's group was the first to show that through the use of an external magnetic to guide Ni incorporated nanowires.[41] The Wang group then subsequently showed that the use of two magnets could potentially stop, turn the the nanomotors, and let them loose for on-demand change of directions.[42] Sen's group has also shown that peroxide-soaked PDMS can cause a chemotaxis, thereby drawing large amounts of nanomotors to the fuel enriched area. Further details below, outline the advancements of external stimuli on controlling nano/microscale motor movements.

Motion control is essential for various applications of man-made nanomachines. One of the first environmental changes that we looked at were the effect of changes in localized temperature.[43] The ability to control and regulate the movement of catalytic and bisegment nanowire motors is illustrated by applying short heat pulses that allow the motors to be accelerated or slowed down. The accelerated motion observed during the heat pulses is attributed primarily to the thermal activation of the redox reactions of the H_2O_2 fuel at the Pt and Au segments and to the decreased viscosity of the aqueous medium at elevated temperatures. Unlike hot wire electrochemistry where the wire serves as the heated working electrode, the heated

wire served here acts solely as the heat source for controlling the solution temperature in the plane of the nanomotors. In order to provide a localized heat source, a 25 μm gold wire was placed 30 μm above the plane of the nanomotors. The estimation of localized temperature was quite a complicated process relying on the earlier simulations of the temperature profile around a heated wire (25 μm diameter) in vertical[44] and horizontal[45] orientations. Based on the simulations of Beckmann et al.[45] and earlier temperature calibrations for 25-μm Au[46] wires, interpolated temperature values for different heating currents between 0 and 700 mA and heat-source distances ranging from 15 to 70 μm. This allowed us to add an instanteous, and controllable heat profile to the solution by turning on and off the known current.

The thermally modulated motion during repetitive temperature on/off cycles is highly reversible and fast, with speeds of 14 and 45 μm s^{-1} at 25 and 65 °C, respectively (Figure 1.5). A wide range of speeds can be generated by tailoring the temperature to yield a linear speed–temperature dependence. Through the use of nickel-containing nanomotors, the ability to combine the thermally regulated motion of catalytic nanomotors with magnetic guidance was also demonstrated. Such on-demand control of the movement of nanowire motors holds great promise for complex operations of future manmade nanomachines and for creating more sophisticated nanomotors. This study was further investigated by Oliver Schmidt's group using tubular microengines in a temperature controlled channel and for similar reasons the catalytic rate and bubble formation rate increased, thereby resulting in microrockets moving at speeds of 10 mm/s.[47]

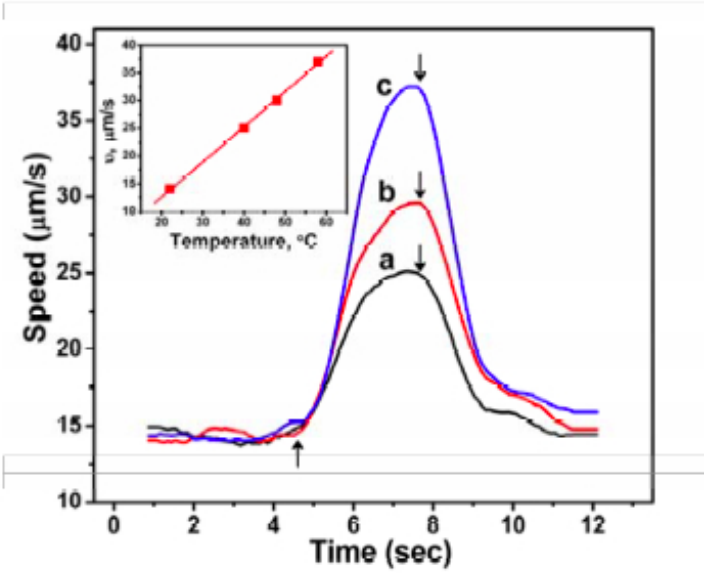

Figure 1.5 Speed-time profiles of Au-Pt nanomotors during different 3-sec heat pulses to 40 (a), 48 (b) and 58 (c) °C in a 5 wt% H2O2 solution. The arrows (around 5 and 8 sec) correspond to the time of switching the heating current 'on' and 'off', respectively.

In addition to a reversible 'on' and 'off' switching of the nanomotor motion, it is possible to tune the applied potential for regulating the movement of catalytic nanomotors. The electrochemically-controlled movement of catalytic nanomotors involves electrolytic reactions of the H_2O_2 and O_2, and reflects primarily the role of the oxygen generated and consumed at these potentials. Figure 1.6 shows the ability to use potential control for reversibly starting and stopping the motion of catalytic nanomotors. It displays velocity time profiles for 10-sec potential pulses of +1.0 and -0.4 V (vs. Ag|AgCl|100 mM KCl reference) in a 5 wt% H_2O_2 fuel solution. A dramatic speed acceleration, from 4 to 22 μm/s, is observed upon stepping the potential from +1.0 V to -0.40 V. The nanomotor speed decreases rapidly upon switching the

potential back to +1.0 V, reaching a value of 5 μm/s (down to Brownian motion) within 10 sec. Note that the speed of these nanomotors without an applied potential corresponded to 9 μm/s.

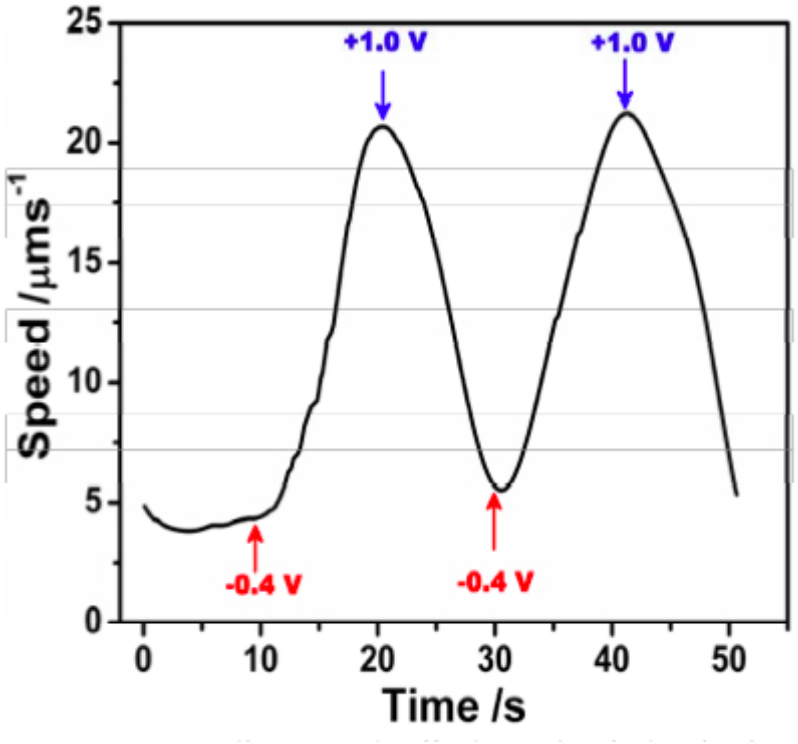

Figure 1.6 Cyclic 'on' and 'off' electrochemical activation of the nanomotor motion upon switching the applied potential (+1.0 to 0.4 V, indicated by arrows) at 10 s intervals in a 5 wt% H2O2 solution.

These changes in speed likely reflect bulk redox reactions of electroactive substances, particularly that of the H_2O_2 fuel and dissolved O_2 involved in the nanomotor movement.[34] Linear sweep voltammetry using a gold-fiber electrode, in the presence and absence of H_2O_2 and dissolved O_2 revealed that the reduction processes of O_2 and H_2O_2 start at potentials more negative than -0.1 V and +0.1 V, respectively, with the oxygen displaying a peak potential of -0.4 V (not shown). The oxygen reduction signal was substantially smaller than the peroxide one, reflecting their vastly

different concentrations in bulk (1.5 M peroxide vs. 1 mM oxygen).[34] Furthermore, it is suspected that oxygen concentrations in particular played the largest role in changes in nanomotor speed because scanning voltammetry on the gold fiber electrode in the anodic direction revealed that starting around +0.40 V H_2O_2 was oxidized forming oxygen. Due to the large excess of H_2O_2 in solution, peroxide oxidation could lead to process saturation of localized oxygen concentration. Similarly, by eliminating or saturating the oxygen in the peroxide fuel and nanomotor solutions before mixing, the Au-Pt nanomotors traveled 22 μm/s vs. 4 μm/s, respectively. This phenomenon is best explained by the observed decrease in mixed potential difference between the Pt and Au nanomotor segments, because of the oxidation of the Pt segment making it less efficient in reducing the peroxide fuel. In conclusion, this study helped further characterize the properties of nanomotors by showing the electrochemically-induced 'on/off' switching of the motion of catalytic nanomotors, along with a fine tuning of the motor speed through control of the applied potential due through the production or removal of localized oxygen in the solution. More importantly, the study shows how an external source can uniformly effect the motion of nanomotors.

Advancements in nanomotors have also enabled nanomotors to pickup, transport and release cargo as it travels through a PDMS channel, thereby providing a proof-of-concept for nanomotor driven Lab-on-Chip devices.[42] This introduction provides insight into existing motor propulsion schemes, their evolution, inherit challenges, and external mechanisms for controlling their spatial and temporal movements.

1.5 Potential for Nano/micromotor Based Biological Applications

There still lies a great need for the development of DNA detection scheme which can be used for the detection of diseases in the medical arena, accelerated response to bioterrorism threats, and early and accurate detection of DNA markers. Although there are currently many suitable DNA detection devices that can be used to accurately identify different concentrations of DNA, many limitations including: cost, complexity, sensitivity to contamination, the ability to detect multiple samples and lack of portability still exist.[48] These are all issues with the current gold standard for DNA detection, Polymerase Chain Reaction. In short, PCR is a technique used to amplify the DNA in solution through the use of DNA polymerase enzymes and site specific primers. Conventionally, amplified DNA can then be fluorescently labeled, run out on a Southern Blot, or quantified using a technique called real-time PCR.[49,50] Ultimately, this powerful technique can be used to detect low levels of DNA, but is very costly and susceptible to contamination. Since the greatest need for DNA detection are areas like the private practitioner's office, battlefield, ground zero for bio-threat, and third world countries are usually inaccessible it is very important that future detection and isolation schemes be made to be both portable and cost efficient.[48] In addition, to test for DNA markers, antigens can be used to detect proteins or the presence of a foreign disease or bio-threat. In this field, the ELISA assay (enzyme-linked immunosorbent assay) is what is most readily used. This assay essentially

harnesses the power of enzymes attached to antibodies that bind directly to the antigens. These enzymes are then used to convert a reactant into some detectable signal that is antigen concentration dependent. Unfortunately, this technique is not very sensitive, is susceptible to photobleaching, uses rather expensive reagents, and the quantitative detection usually uses a spectrophotometer machine which is not portable.[48,51] For these reasons scientists have been looking at using nanotechnology as a means to develop a cheap, accurate, sensitive and portable DNA and/or protein detection device.

Scientists have investigated the use of nanomaterials, because small metal nanoparticles have specific optical, and plasmonic properties that make them ideal for multiplex detection.[48] Although rather expensive to initially produce, nanoparticles can be generally created in large batches making them very cost efficient. The ability to show the multiplexing capabilities of nanomaterials was shown by the Nei[52] group who showed through the use of varying ratios of CdSe quantum dots (nanomaterial which absorbs overlong range but emits at a sharp peak having an inherit color) that you could potentially detection millions of different DNA targets at the same time. In general, one of the most prominent DNA detection techniques being explored is the use of a sandwich assay.[53] First, a captured probe DNA is attached to a gold surface, where it can bind to the target DNA. If present, a detector probe with attached Au nanoparticle can be used to signal target concentration through the inherent surface plasmonic properties (colorimetric change based on size and aggregation of Au nanoparticles). The use of silver enhancement of Au nanoparticles allows for detection

down to the fmolar level by using a flatbed scanner (scanometric technique).[54] The use of nanowire barcodes, magnetic particles, Q-Dots, and nanoparticles are continually combined and advanced for the purpose of advancing the sensitivity and multiplexing capabilities of nanomaterial DNA detection.[55] However, many of these techniques are timely, and not affordable.

Overall, the use of motion has recently started to emerge as a useful biodetection tool. Recently, the rotation of biological ATPase motors has been exploited for detecting nucleic acid targets.[4,5] Additionally, the movement of microtubules along a kinesin- coated PDMS track has enabled the on-the-go pick up, tag, and detection of antigens thereby removing the typical washing steps in a double antibody sandwich assay.[10] Recent efforts have demonstrated the ability of synthetic nanomotors to convert chemical energy or external energy sources into autonomous motion.[56,57] In particular, the efficient electrochemical propulsion of catalytic bisegment nanowires1[13,15,18,35,42] and microtube engines[22,23] has been demonstrated in the presence of hydrogen peroxide fuel. Such nanowire and microtube motors display high power and speed, along with a precise motion control and can be easily modified to impart new functionalities.

The ability of electrochemically-propelled nanomotors to respond to their surrounding environment (as previously shown in the presence of external stimuli) has opened the door for developing new motion-based detection platforms. Novel motion-based signal transduction involving changes in the speed or distance of nanowire motors induced by the target analyte[58] or by a specific biomolecular interaction,[59] can

thus be realized. Such motion-based transduction relies on the use of an optical microscope for tracking changes in the speed of nanowire motors in the presence of the target analyte, hence obviating the need for sophisticated analytical instruments. Specific biorecognition events can thus be translated into useful speed/distance signals where the binding event leads to a change in the motion.

Efficient isolation of target biomaterials from a complex mixture represents one of the most challenging tasks in biology. Biological targets, ranging from nucleic acids to proteins and cancer cells, are typically isolated from raw biological samples by using laborious, time-consuming and/or expensive protocols.[61,61] Receptor-functionalized nanomachines can provide a fundamentally new concept for addressing the challenge of isolating biological targets from complex body fluids and transporting them to a clean environment for downstream analysis. Such nanomachine-enabled target isolation offers considerable promise for diverse biotechnological and bioanalytical applications, and for designing miniaturized lab-on-chip systems, integrating the capture, transport and release operations.

Finally, scientist across disciplines has been searching for new solutions for targeted drug delivery and treatment. Many approaches have involved masking drug-loaded nanocarriers such as PLGA to make them more biocompatible. One approach would be to utilize active transport to ensure localized targeted delivery. Recent studies have shown the ability of different artificial nanomotors to transport various types and sizes of cargo, *e.g.*, drug-loaded liposomes, in a complex channel with or without a hydrostatic flow.[62,63] The high towing power and accurate motion control

allow the nanomotors to load multiple cargos and transport them through complex microchannel networks to desired locations in the microchip. These develops provide the basis for the biological experiments to presented in the upcoming chapters.

Chapter 1 is based, in part, on the material as it appears in Analyst, 2011, by Susana Campuzano, Daniel Kagan, Jahir Orozco, and Joseph Wang; in part on material from Small, 2009, by Shankar Balasubramanian, S., Daniel Kagan, Kalian Manesh, Percy Calvo-Marzal, Gerd Flechsig, and Joseph Wang; in part on material from Chemical Communications, 2009, by Percy Calvo-Marzal, S., Kalian Manesh,Daniel Kagan, Shankar Balasubramanian, and Joseph Wang; and in part on material from ACS Nano, 2009, by Kalian Manesh, Maria Cardona Rodger Yuan, Michael Clark, Daniel Kagan, Shankar Balasubramanian, and Joseph Wang. The dissertation author was the primary investigator and co-author of these papers.

1.6 References

1. Hess, H.; Battered, G. Nanotoday. **2005**, 2, 23.
2. Johnson, A. Molecular Biology of the Cell. Garland. New York; **2008**
3. Li, F.; Redick, S.D.; Erickson, H.P.; Moy, V.T.; *Biophysical Journal.* **2003**, *84*, 1252.
4. Bachand, G. D., and Montemagno, C. D., Biomed. Microdevices. **2000**, 2 (3), 179.
5. Schmidt, J. J., and Montemagno, C. D., *Annu. Rev. Mater. Res.* **2004** *34*, 315.
6. Liu, H., Schmidt, J.J.; Bachand, G.D.; Rizk, S.S.; Looger, L.L.; Hellinga, H.W.; Montemagno, C. D., Nat. Mater. 2002 1, 173-177.
7. Schmidt, J. J., Jiang, X.; Montemagno, C. Nano Lett. 2002, 2, 1229-1233.
8. Hess, H., Clemmons, J.; Howard, J.; Vogel, V. Nano Lett. 2002, 2, 113-116
9. Goel, A.;Vogel.V. *Nature Nano.* **2008***, 3*, 463
10. Fischer, T., Agarwal, A. & Hess, H. *Nat. Nanotechnol.* **2009***, 4,* 162-166.
11. Heuvel, M.G.L.; Dekker, C. Science, 2007, 317, 333.
12. Schwartz, A.; Bowden N.; Whitesides, G.W. *Angew. Chem., Int. Ed.,* **2002***, 41*, 652.
13. Mirkovic, T.; Zacharia, N. S.; Scholes, G. D.; Ozin, G. A.; *Small* **2010** *6,* 159–167.
14. Paxton,W; Sen, A.; Mallouk, T. *E. Chem. Eur. J.* **2005***, 11,* 6462.
15. Paxton, W. F. et al. J. Am. Chem. Soc. 2004, 126, 13424
16. Wang, J.; Manesh, K. M. *Small* **2010***, 6,* 338–345.
17. Ebbens, S. J.; Howse, J. R. *Soft Matter* **2010***, 6,* 726–738.
18. Ozin, G. A.; Manners, I.; Fournier-Bidoz, S.; Arsenault, A. *Adv. Mater.* **2005***, 17*, 3011– 3018.
19. Ruckner, G.; Kapral, R.; *Phys. Rev. Lett.* **2007***, 98,* 150603.
20. Howse, J. R.; Jones, R. A. L.; Ryan, A. J.; Gough, T.; Vafabakhsh, R.; Golestanian, R., *Phys. Rev. Lett.* **2007,** 99, 48102.
21. Ibele, M.; Mallouk, T. E.; Sen, A. *Angew. Chem., Int. Ed.* **2009**, *48*, 1408.

22. Solovev, A. A.; Mei, Y. ; Bermúdez Ureña, E.; Huang, G.; Schmidt, O. G. *Small* **2009**, *5*, 1688–1692.

23. Mei, Y.; Huang, G.; Solovev, A. A.; Bermúdez Ureña, E.; Mönch, I.; Ding, F.; Reindl, T.; Fu, R. K. Y.; Chu, P. K.; Schmidt, O. G. Adv. *Mater.* **2008**, *20*, 4085–4090.

24. Li, J.; Huang, G.; Ye, M.; Li, M.; Liu, R.; Mei, Y. *Nanoscale,* **2011***, 3,* 5083-5090.

25. Sanchez, S.; Solovev, A.A.; Mei, Y.; Schmidt, O.G. *J. Am. Chem. Soc.*, **2010**, 132, 13144–13145.

26. Gao, W.; Uygun, A.; Wang, J. *J. Am. Chem. Soc.* **2012,** 134, 897-900.

27. Gao, W.; Sattayasamitsathit, S.; Orozco, J.; Wang, J. *Journal of the American Chemical Society* **2011,** 31, 11862-11864.

28. Ghosh A.; Fischer, P. *Nano Lett.,* **2009***, 9,* 2243-2246.

29. Gao, W.; Sattayasamitsathit, S.; Manesh, K. M.; Weihs, D.; Wang, J., *J. Am. Chem. Soc.* **2010,** 132, 14403–14405.

30. Pak, O. S.; Gao, W.; Wang, J.; Lauga, E. *Soft Matter* **2011***, 7,* 8169.

31. Kagan, D.; Benchimol, M.; Claussen, J.; Chuluun-Erdene, E.; Esener, S.; Wang, J.; *Nature Nano.* Submitted

32. Gibbs, J. G.; Zhao, Y.-P. Small. **2009**, 5, 2304–2308.

33. Wang, Y.; Feh, S.-T.; Byun, Y.; Lammert, P. E.; Crespi, V. H.; Sen, A.; Mallouk, T. E. *J. Am. Chem. Soc.* **2009**. *131,* 9926–9927

34. Wang, Y.; Hernandez, R. M.; Bartlett, D. J.; Bingham, J. M.; Kline, T. R.. Sen, A.; Mallouk, T. E. *Langmuir* **2006**, *22*, 10451.

35. Kline, T. R.; Paxton, W. F.; Mallouk, T. E.; Sen, A.; *Angew. Chem. Int. Ed*. **2005**, *44*, 744–746.

36. Laocharoensuk, R. ; Burdick, J.; Wang, J. *ACS Nano* **2008***, 2,* 1069–1075.

37. Demirok, U. K.; Laocharoensuk, R.; Manesh, K. M.; Wang, J. *Angew. Chem., Int. Ed.* **2008**, *47*, 9349.

38. Pantarotto, D.; Browne W. R.; Feringa, B. L. *Chem. Commun.* **2008***, n/a* 1533-1535.

39. Paxton, W. F.; Baker, P. T.; Kline, T. R.; Wang, Y.; Mallouk, T. E.; Sen, A. *J. Am. Chem. Soc.* **2006***, 128*, 14881–14888.

40. Gao, W.; Kagan, D.; Pak, O. S.; Clawson, C.; Campuzano, S.; Chuluun-Erdene, E.; Shipton, E.; Fullerton, E. E.; Zhang, L.; Lauga, E.; Wang, J., Cargo-Towing Fuel-Free Magnetic Nanoswimmers for Targeted Drug Delivery. *Small* **2011**.

41. Sundararajan, S.; Lammert, P. E.; Zudans, A. W.; Crespi, V. H.; Sen, A. *Nano Lett.* **2008***, 8,* 1271–1276.

42. Burdick, J.; Laocharoensuk, R.; Wheat, P. M.; Posner, J. D.; Wang, J. *J. Am. Chem. Soc.* **2008***, 130*, 8164– 8165.

43. Balasubramanian, S.; Kagan, D.; Manesh, K. M.; Calvo-Marzal, P.; Flechsig, G.; Wang, J. *Small* **2009***, 5,* 1569–1574.

44. Frischmuth, K.; Visocky, P.; Gründler, P. *Int. J. Eng. Sci.* **1996***, 34,* 523.

45. Beckmann, A.; Coles, B.A.; Compton, R.G.; Gründler, P.; Marken, F.; Neudeck, A. *J. Phys. Chem. B* **2000***, 104,* 764-768.

46. Flechsig, G.-U.; Korbut, O.; Gründler, P. *Electroanalysis* **2001***, 13*, 786.

47. Sanchez, S.; Solovev, A. A.; Harazim, S. M.; Schmidt, O. G., *J. Anal. Chem. Soc.* **2011,** 133, (4), 701-703.

48. Rosi, N.; Mirkin, C. *Chem. Rev.* **2005***, 105,* 1547−1562

49. Tyagi, S.; Kramer, F. R. *Nat. Biotechnol.* **1996***, 14*, 303-306.

50. Duggan, D. J.; Bitttner, M.; Meltzer, P.; Trent, J. M. *Nat. Genet. Suppl.* **1999***, 21,* 10-18.

51. Hirsch,L.R.; Jackson,J.B.; Lee,A.; Halas,N.J.; West, *J. Anal. Chem.* **2003***, 75,* 2377-2380.

52. Han, M.; Gao, X.; Su, J. Z.; Nie, S. *Nat. Biotechnol.* **2001***, 19,* 631.

53. Yguerabide, J.; Yguerabide, E. E. J. *Cell. Biochem.* **2001**, 37, 71.

54. Taton, T. A.; Mirkin, C. A.; Letsinger, R. L. *Science* **2000***, 289,*1757.

55. Nam, J.-M.; Stoeva, S.; Mirkin, C. A. *J. Am. Chem. Soc.* **2004***,*126, 5932.

56. Mallouk, T. E.; Sen, A. *Sci. Am.* **2009***, 300,* 72–77.

57. Wang, J. *ACS Nano* **2009**, *3*, 4-9.

58. Kagan, D.; Calvo-Marzal, P.; Balasubramanian, S.; Sattayasamitsathit, S.; Manesh, K. M.; Flechsig, G.-U.; Wang, J. *J. Am. Chem. Soc.* **2009***, 131,* 12082– 12083.

59. Wu, J.; Balasubramanian, S.; Kagan, D.; Manesh, K. M.; Campuzano, S.; Wang, J., *Nat. Commun.* **2010,** 1, 36.60.

60. Adams, A. A.; Okagbare, P. I.; Feng, J.; Hupert, M. L.; Patterson, D.; Göttert, J.; McCarley, R. L.; Nikitopoulos, D.; Murphy, M. C.; Soper, S. A. *J. Am. Chem. Soc.* **2008***, 130,* 8633–8641.

61. Duarte, G. R. M.; Price, C. W.; Littlewood, J. L.; Haverstick, D. M.; Ferrance, J. P.; Carrilho, E.; Landers., J. P. *Analyst* **2010***, 135,* 531

62. Kagan, D.; Laocharoensuk, R.; Zimmerman, M.; Clawson, C.; Balasubramanian, S.; Kang, D.; Bishop, D.; Sattayasamitsathit, S.; Zhang, L.; Wang, J. *Small* **2010***, 6,* 2741– 2747.

63. Sanchez, S.; Solovev, A. A.; Harazim, S. M.; Schmidt, O. G. *J. Am. Chem. Soc.* **2011***, 133*, 701– 703.

Chapter 2 Nanomotor Motion-based Sensing

2.1 Silver Ion Sensing

2.1.1 Silver Ion Sensing Introduction

Considerable recent efforts have been devoted to the development of artificial nanomotors.[1-3] In particular, fuel-driven bisegment Au-Pt nanowires exhibit autonomous self-propulsion due to electrocatalytic decomposition of hydrogen peroxide fuel.[1-5] Such autonomous motion of catalytic nanowire motors holds great promise for exciting applications ranging from drug delivery, nanoscale assembly and transport, or motion-based biosensing.[1-3]

This section reports the first example of using catalytic nanomotors for motion-based chemical sensing, and particularly for specific detection of trace silver ions. During recent experiments in our laboratory involving electrochemically triggered motion of catalytic nanowire motors,[6] we observed unusual speed acceleration associated with silver ions generated at a pseudo silver- wire reference electrode

placed in the vicinity of the nanowire motors. Such an unexpected specific silver effect upon the speed of catalytic nanomotors has been exploited in the present work for designing a new motion-based silver sensing protocol. The new protocol relies on the use of an optical microscope for tracking the speed of nanowire motors and offers highly selective, sensitive, and simple measurements of trace silver based on direct visualization.

2.1.2 Silver Ion Sensing Experimental Methods

2.1.2.1 Nanomotor Preparation

The gold/platinum nanomotors were prepared by sequential electrodeposition of gold and platinum into 200-nm-diameter nanopores of a 60 μm-thick alumina membrane template (Catalog No. 6809-6022; Whatman, Maidstone, U.K.). A thin gold film was first sputtered on the branched side of the membrane to serve as a working electrode. The membrane was assembled in a Teflon plating cell with aluminum foil serving as an electrical contact for the subsequent electrodeposition. A sacrificial copper layer was first electrodeposited into the branched area of the membrane using a 1 M cupric sulfate pentahydrate solution ($CuSO_4.5H_2O$; Sigma-Aldrich, St. Louis, MO), using a charge of 10 Coulombs and a potential of -1.0 V (*vs*. Ag/AgCl reference electrode) along with platinum wire as a counter electrode. Subsequently, Au segment was plated from a gold plating solution (Orotemp 24 RTU RACK; Technic Inc., Anaheim, CA) and electrodeposited at a total charge of 1.5 Coulombs and a potential of -0.9 V. Platinum was then deposited galvanostatically

using a current of -2 mA for 50 min from a platinum plating solution (Platinum RTP; Technic Inc). The resulting Au-Pt nanowires had a length of around 2 μm. The sputtered gold layer and the copper sacrificial layer were simultaneously removed by mechanical polishing using cotton tip applicators soaked with 0.5 M $CuCl_2$ solution in 20% HCl. The nanomotors were then released by immersing the membrane in 3 M NaOH for 30 minutes. The synthesized nanomotors were separated from solution using by centrifugation at 10,000 rpm for 5 min and washed repeatedly with ultrapure water (18.2 MΩ cm) until a neutral pH was achieved. Between the washing steps the nanomotors solution was mixed with ultrapure water and briefly sonicated (2-5 seconds) to ensure the complete dispersion of nanomotors in the washing water. All nanomotors were stored in ultrapure water at room temperature and their speed was tested before each experiment.

To prepare, 2 μm monocomponent nanowires, Pt was deposited for 70 min and Au was deposited for 2.5 C using the method described above. To study the deposition of Ag, bimetallic and monocomponent nanowires were individually mixed with 5% H_2O_2 and 50 μM $AgNO_3$ for different times. The residual silver ions and peroxide were removed by repeated washing with ultrapure water. Energy dispersive X-ray analyses (EDX) of the nanowires were performed using Phillips XL30 ESEM instrument to confirm the metal composition of nanowires.

2.1.2.2 Experimental Procedures

To study the effect of silver ion (and of other cations) upon the motion of Au-Pt nanowire motors, the nitrate salts of the various metals were mixed with the

nanomotor/fuel solution. Metal nitrate salts were purchased from Sigma or Fisher with a purity of 99.99% (or higher) to minimize potential impurity effects. The speed of the nanowire motors was examined in a solution prepared by mixing 50 μl of equal parts (1:1:1) of the diluted nanomotors suspension, the metal nitrate solution, and a freshly prepared 15 wt% H_2O_2 solution. A 10 μl aliquot of this solution was then added to the glass slide for immediate video acquisition.

The tracking of nanomotors was performed following the protocol reported earlier.[7] An inverted optical microscope (Nikon Instrument Inc., Eclipse TE2000-S) equipped with a 20x objective, a Photometrics CoolSnap CF camera (Roper Scientific, Duluth, GA) and MetaMorph 7.1 software (Molecular Devices, Sunnyvale, CA, USA) was used for capturing videos at a frame rate of 10 fps. This software calculates the instantaneous velocity by tracking the object's center-to-center displacement from frame to frame. The program averages the instantaneous velocities over the 50 frames tracked to yield an overall average speed. Usually 5 videos from randomly selected glass slide areas (200 μm X 200 μm) were recorded to ensure accurate population sampling. Approximately, 20 random nanomotors were tracked for 50 frames to obtain a representative nanomotor speed. To distinguish between Brownian and non-Brownian motions, the motion of the nanomotors was compared to that observed without fuel. Typically, nanomotors in water display a Brownian motion, i.e. tumbling and/or sideways motion, with speeds of ~3 μm/s.

2.1.3 Silver Ion Sensing Results and Discussion

Figure 2.1.1A displays traces of Au-Pt nanomotors (over a 3 s period), taken from videos of the nanowires in the presence of 11 different cations (100 μM each), along with the peroxide fuel. Of these cations, 10 caused a significant speed reduction, including a Brownian motion or a slower non-Brownian motion (with speeds ranging from 0.3 to 7.1 μm s-1). Such slow speed (compared to an actual speed of ~10 μm/s observed without these salts) is consistent with the self-electrophoresis mechanism for the propul- sion of catalytic nanomotors,[8] where the speed decreases linearly with the solution conductivity.[9] In contrast, the nanomotors move over a dramatically longer path in the presence of silver (shown in the middle), displaying an average speed of 52 μm/s. Also shown in Figure 2.1.1B is the histogram depicting the average speed of the nanomotors in the presence of the different cations tested. These data, along with the corresponding Supporting Video 2.1, clearly illustrate the remarkably selective acceleration in the presence of silver. Adding other cations (e.g., Pb2+ or K+ up to 5 μM) had only slight reductions in the speed signal in the presence of the silver analyte. Apparently, the presence of a silver ion can greatly minimize the ionic-strength limitation of catalytic nanomotors. A high speed of ~20 μm/s was maintained in the presence of 0.1 mM K+ (compared to a slower motion of 7 μm/s observed for K+ without the silver). Higher (>mM) salt concentrations, however, led to the expected conductivity-induced speed diminution.

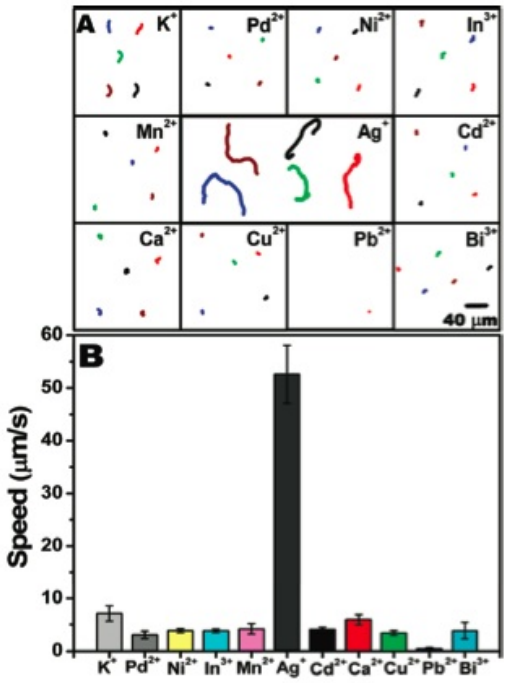

Figure 2.1.1 Motion of Au-Pt catalytic nanomotors in a 5% H2O2 solution containing 11 common cations. (A) Image displaying 3 s track lines for the movement of 5 randomly selected nanomotors in 11 different 100 μM metal-nitrate salt solutions (of K+, Pd2+, Ni2+, In3+, Mn2+, Ag+, Cd2+, Ca2+, Cu2+, Pb2+, and Bi3+). (B) Corresponding bar graph comparing the average nanomotor speed (conditions same as those in A). Error bars for $n = 20$.

The highly selective motion-based response is characterized also with a defined concentration dependence, with the speed (or distance) providing the quantitative information. Figure 2.1.2A-D and Video 2.1 display track lines of the catalytic nanomotors (over a 2 s period) obtained in the presence of different silver concentrations (0, 1, 10, and 100 μM; A-D). These traces indicate clearly that the nanomotors travel longer distances (ranging from 19 to 104 μm) upon increasing the silver concentration. Such paths correspond to speeds ranging from 9.6 μm/s (without silver) to 52 μm/s (at 100 μM silver). Also shown in Figure 2.1.2E is a calibration plot of the speed vs silver concentration over the 10-9 to 10-4 M range. Such a plot displays a defined concentration dependence over the 0.5 to 100 μM range, along with

a negligible concentration effect at lower Ag(I) levels. Note that the behavior observed in Figure 2.1.2 is conflicting to what is commonly expected upon increasing the salt concentration.[9]

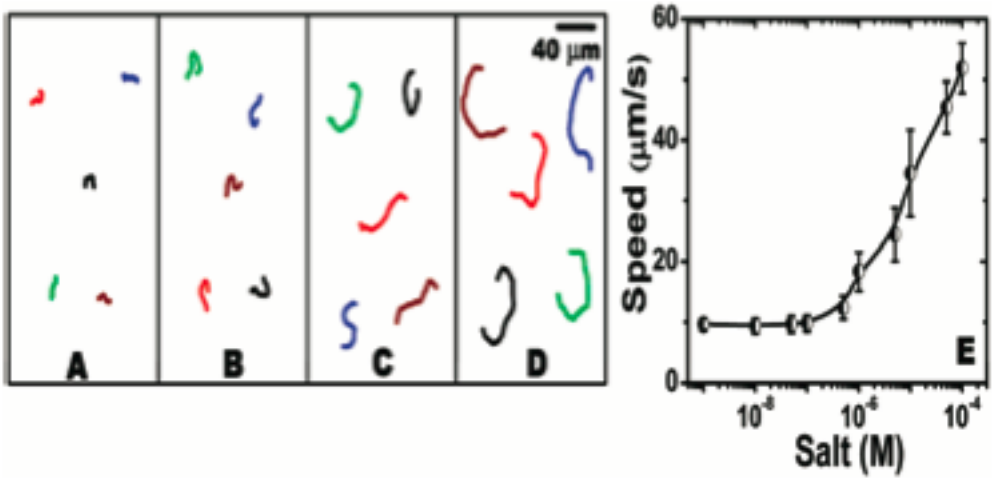

Figure 2.1.2 Track lines of nanomotors illustrating the distances traveled by five Au-Pt nanowires in the presence of different Ag(I) concentrations: 0 (A), 1 (B), 10 (C), and 100 (D) μM, along with 5 wt % H2O2 fuel solution. (E) A calibration curve for Ag(I) over the micromolar range (0.5-100 μM). Other conditions same as those in Figure 1.

Several possible mechanisms have been considered to explain the unusual acceleration of Au-Pt nanomotors in the presence of silver ions. The most promising explanation relies on the under-potential deposition (UPD) of silver on the Au-Pt nanowires. With the addition of silver ions, these ions adsorb over the nanowire surface and are then reduced in the presence of hydrogen peroxide. Energy dispersive X-ray spectroscopy (EDX) measurements con- firmed the presence of metallic silver over the Pt and Au segments of the nanowires (at 13 and 0.4 Ag atomic %, respectively), following a 0.5 h exposure to the silver nitrate/hydrogen peroxide solution. A clear change of the color of the Pt segment was observed from analogous SEM experiments. No such compositional or color changes were observed in the

presence of silver alone (without hydrogen peroxide). As will be illustrated below, a similar silver deposition was observed on platinum and gold nanorods. In addition, nanomotors exposed to a 100 μM Ag(I)/5% H2O2 solution for 0.5 and 24 h, followed by a thorough wash with nanopure water, displayed high speeds of 20 and 35 μm/s, respectively, in a fresh silver-free 5% H2O2 solution. These data confirm that the deposited Ag(0), rather than the dissolved Ag(I), is responsible for the accelerated motion. The possibility of depositing Ag(0) by UPD onto gold nanorods and platinum surfaces was discussed by several groups.[10-12]

Such silver deposition onto catalytic nanowires can lead to differences in the surface and catalytic properties (and hence to a faster axial speed). Deposition of silver onto the Au segment increases the mixed potential difference (ΔE) between the anodic and cathodic segments, leading to an accelerated nanomotor motion in a manner similar to that reported recently for high-speed alloy nanomotors.[13] Similarly, the silver deposition onto the Pt segment may make it more catalytically active. The accelerated electrocatalytic decomposition of hydrogen peroxide was indicated also by the sharp decline of the motor speed following a 10 min exposure to the silver ion (compared to a longer ~30 min period observed without silver). The faster speed was then restored upon restoring the initial fuel level.

To isolate the role of the individual segments upon speed acceleration, the motility of monocomponent Pt and Au nanorods was examined in the presence of silver nitrate. Surprisingly, monocomponent Pt rods displayed a dramatic acceleration from 3.5 to 22.6 μm/s in the presence of 10 μM silver ion. Monocomponent Au

nanorods, in contrast, display a Brownian motion in the presence and absence of Ag(I). The EDX data of Figure 2.1.3 confirm the presence of silver on monocomponent Pt and Au nanowires, with Ag(0) values of up to 18 and 10 (Ag atomic %), respectively. Apparently, the Ag(0) deposition onto mono-component platinum nanowires leads to the asymmetry (bimetal character) essential to induce the electrocatalytic propulsion. This is in agreement with a recent hydrogen peroxide based fuel cell study where a Pt-Ag (anode-cathode) combination exhibits the highest current density compared to other anode-cathode combinations, including Au-Ag.[14] Similarly, it was reported that Au-Ag bimetallic nanowire motors have a very slow speed of 6 μm/s. The self-diffusiophoresis mechanism[9] may also be considered for explaining the silver effect. Here, the deposition of silver over the nanomotors increases the localized gradient of reaction products around the nanomotors, leading to a diffusiophoretic movement of the nanomotor.[15-17] Such an ionic gradient around the nanomotors results in a net electric field in solution that facilitates the increased speed.

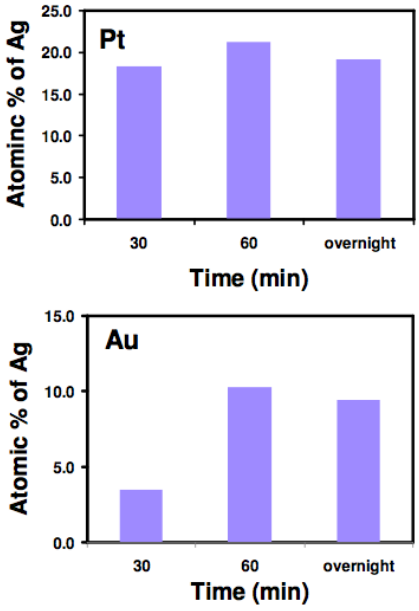

Figure 2.1.3 Atomic % of Ag on monocomponent Pt and Au nanowires obtained from EDX measurements. In all experiments, monocomponent Pt and Au nanowires were individually mixed with 5% H2O2 and 50 μM AgNO3 and analyzed at different times.

2.1.4 Silver Ion Sensing Conclusions

In summary, we have described the first example of motion-based chemical sensing involving fuel-driven nanomotors. Effective measurements of trace Ag(I) have been accomplished based on the dramatic and specific acceleration of bimetal nanowire motors in the presence of this ion. While these initial data clearly demonstrate the utility of catalytic nanomotors for measuring micromolar concentrations of silver, additional work is required toward a better understanding of the unusual silver effect or the defined concentra- tion dependence and for adapting the new concept for practical real-life applications. The presence of silver also facilitates the operation of catalytic nanomotors in conducting media that were not accessible earlier to catalytic nanomotors. While the new concept of motion-based

sensing has been illustrated for trace measurements of Ag(I), we anticipate that it would lead to a wide range of novel sensing protocols. Current efforts in our laboratory examine new bioaffinity displacement assays based on the ability of a target biomolecule to trigger the movement of an anchored nanomotor. We expect that such motion-based bioassays would lead to remarkable sensitivity, reflecting the ability to detect single-binding events.

2.2 DNA Sensing

2.2.1 DNA Sensing Introduction

Wide-scale genetic testing requires the development of easy-to-use, fast, inexpensive, miniaturized analytical devices. DNA hybridization biosensors commonly rely on different types of optical,[18,19] electrochemical[20,21] and mechanical[22] transducers to convert duplex formation recognition events into useful analytical signals. Nanomaterial tags have greatly benefited such bioassays through amplified or multiplexed measurements.[23,24] However, autonomously propelling nanoscale materials have not been exploited for biosensing applications.

Chemically powered nanomotors, particularly bisegment Au–Pt nanowires, exhibit autonomous propulsion because of the electro- catalytic decomposition of hydrogen peroxide fuel.[25–29] Previous efforts in the field of synthetic nanomotors have concentrated on increasing their speed and power and in imparting precise motion control and cargo-towing capabilities. Factors influencing the nanomotor speed, including motor and fuel compositions, along with new motor capabilities, have been reviewed elsewhere.[25–27] Recently, we discovered an unusual increase in the speed of catalytic nanowire motors in the presence of silver ions.[30]

In this section, a fundamentally new nanomotor-based biodetection platform is presented for specific DNA and RNA detection. Silver- induced nanomotor speed enhancement is used in a sensitive, rapid and simple hybridization assay. Our motion-based hybridization sandwich assay relies on the duplex formation of the nucleic acid target with a thiolated DNA capture probe and a silver nanoparticle-tagged detector

probe (SH-DP-Ag NPs). Subsequent dissolution of the Ag nanoparticle tags in the hydrogen peroxide fuel releases Ag ions, which, on adding an aliquot of the unmodified nanomotor solution, causes a substantial increase in their speed. The higher the concentration of the nucleic acid target, the more the silver nano- particles (Ag NPs) that are captured, and the greater the nanomotor speed. The resulting distance signals allow convenient measurements of the DNA target down to the attomole level. This new nanomotor concept may be readily expanded for detecting protein markers in connection with antibody or aptamer receptors. The motility of motor proteins has been proposed recently for transporting and detecting target biomolecules.[31,32] However, there are no reports on using synthetic nanomotors for transducing biorecognition events into motion. Such artificial nanomachines address the limitations of using biological motors, including a limited lifetime *in vitro* and a narrow functioning range of environmental conditions.[26]

2.2.2 DNA Sensing Experimental Methods

2.2.2.1 Reagents

Silver nanoparticles (diameter 20 ± 5 nm given by the manufacturer) were purchased from Ted Pella (cat no. 15705-20SC). MCH, sodium dodecyl sulphate (SDS), DTT, trizma hydrochloride (Tris-HCl), ethylenediamine- tetraacetic acid and bovine serum albumin were obtained from Sigma-Aldrich and used without further purification. The blocking agent casein was obtained from Pierce.

The buffer solutions used were as follows: The DNA immobilization buffer was 10 mM Tris-HCl, 1 mM ethylenediaminetetraacetic acid and 0.3 M NaCl (pH

8.0). The hybridization buffer (HB) was a 1 M phosphate buffer solution containing 2.5% bovine serum albumin and 0.05% casein (pH 7.2). The storage buffer for SH-DP-Ag NPs contained 10 mM phosphate buffer, 300 mM NaCl and 0.01% SDS (pH 7.2).

The sequences of the oligomers used for the detection of synthetic 30-mer oligonucleotides or *E. coli* 16S rRNA targets are given in the Table 2.2.1 All thiolated oligonucleotides were purchased from Integrated DNA Technologies. Other oligonucleotides, that is, the complementary and non-complementary targets, were obtained from Thermo Fisher Scientific. According to the sandwich protocol, SH-CP was immobilized on the gold surface, whereas SH-DP was conjugated with Ag nanoparticle tags.

Bacterial strains of *E. coli* (NEB 5-α) and *K. pneumoniae* (KP210) were obtained from the University of California, Los Angeles. The isolates were stored at −80 °C and were freshly lysed before each experiment.

2.2.2.2 Preparation of Nanomotors

The Au–Pt nanomotors were prepared by sequential electrodeposition of gold and platinum into 200-nm-diameter nanopores of a 60 μm-thick alumina membrane template (cat. no. 6809-6022, Whatman).[20] Briefly, the branched side of the membrane was sputtered with a thin gold film, followed by electrodeposition of a sacrificial copper layer from a 1 M cupric sulphate pentahydrate solution (CuSO4.5H2O, Sigma-Aldrich), using a charge of 10 C and a potential of − 1.0 V (versus Ag/AgCl reference electrode), along with a platinum wire counter electrode. Subsequently, the Au

segment was plated from a gold plating solution (Orotemp 24 RTU RACK; Technic) and electrodeposited at a total charge of 1.5 C and a potential of − 0.9 V. Platinum was then deposited galvanostatically using a current of − 2 mA for 50 min from a platinum plating solution (Platinum RTP; Technic). Similarly, magnetic Au–Ni–Au–Pt nanomotors were prepared by introducing a ferromagnetic Ni segment. Following an initial deposition of gold segment at 0.75 C, Ni was electrodeposited at − 1.0 V for 2 C (versus Ag/AgCl) from a plating solution (20 g l − 1 NiCl2 6H2O, 515 g/l $Ni(H2NSO3)_2$ 4H2O and 20 g/l H_3BO_3 (buffered to pH 3.4)). Subsequently, the second gold segment (0.75 C) and a platinum segment were electrodeposited as above. The sputtered gold layer and the copper sacrificial layer were sequentially removed by mechanical polishing using cotton tip applicators soaked with 0.5 M $CuCl_2$ solution in 20% HCl. The nanomotors were then released by immersing the membrane in 3 M NaOH for 30 min. The synthesized nanomotors were separated from solution by centrifugation at 2,300 *g* for 5 min and washed repeatedly with ultrapure water (18.2 MΩ cm) until a neutral pH was achieved. Between the washing steps, the nanomotor suspension was mixed with ultrapure water and briefly sonicated to ensure the complete dispersion of nanomotors. All nanomotors were stored in ultrapure water at room temperature and their speed was tested before each experiment to identify potential nanomotor ‘malfunction’.

2.2.2.3 Conjugation of SH-DP with Ag NPs

The SH-DP-Ag NPs were prepared in accordance with earlier studies.[41-44] The silver colloid (0.12 nM given by the manufacturer) was concentrated ten times by centrifugation (16,770 *g*, 15 min) and redispersed in nanopure water to yield a final concentration of 1.2 nM. Appropriate aliquots of SH-DP were added (final concentration 10 μM) to 100 μl of the 1.2 nM Ag NPs solution and incubated for 2 h. The SDS solution (1%) and 100 mM (pH 7.2) phosphate buffer solution were added to the above mixture to reach final concentrations of 0.01% and 10 mM, respectively. The solution was kept for gentle shaking overnight. Small aliquots of 2 M NaCl were added over 48 h to raise the final NaCl concentration to 500 mM, followed by another overnight incubation. Subsequently, the excess of SH-DP was removed by centrifugation (24,150 *g*, 10 min) and redispersed in storage buffer, a procedure repeated three times.

2.2.2.4 Assembling the capture probe at the gold surface

DNA hybridization was performed on an array of 16 gold electrodes (each 2.5 mm diameter; GeneFluidics.). Initially, 10 μM of freshly prepared DTT was added to SH-CP (0.5 μM) in immobilization buffer and allowed to stand for 10 min. A 6 μl aliquot of this SH-CP solution was drop cast to cover each Au sensor and stored overnight at 4 °C in a humidified environment. After washing with ultrapure water, the probe-modified Au sensors were treated with 6 μl of the 1 mM MCH aqueous solution for 50 min to obtain a ternary self-assembled monolayer. Finally, the sensors were thoroughly rinsed with ultrapure water and dried under nitrogen.

2.2.2.5 DNA hybridization assay

The DNA detection strategy is illustrated in Figure 2.2.1 Different concentrations of the DNA target (or non-complementary and mismatched oligos) were prepared in HB. Aliquots (4 μl) of this target solution were cast on each SH-CP-modified gold sensor and incubated for 15 min. After the sensors were slightly rinsed by ultrapure water and dried by N2, a 4 μl of SH-DP-Ag NPs conjugation solution was cast on each sensor and was incubated for 30 min. After incubation, each sensor was thoroughly rinsed and sub- sequently washed with ultrapure water in a shaker (300 r.p.m.) for 5 min and dried with N_2. These sensors were immediately used for the nanomotor-based hybridization assay

2.2.2.6 Bacterial 16S rRNA hybridization assay

The bacterial 16S rRNA target, derived from single-step bacterial lysis,[37] was detected using the same SH-CP and Ag NPs- modified detector probe, in a manner similar to the synthetic 30-mer target DNA detection. The bacteria were initially lysed by resuspending the appropriate pellet containing ~107 CFU bacteria in 10 μl of 1 M NaOH and incubating for 5 min.

A 50 μl aliquot of HB was added to this 10 μl bacterial lysate, leading to genetic material corresponding to ~107 CFU per 60 μl (final pH 7.8). This solution was serially diluted in HB to provide different concentrations of bacterial genetic material (16S rRNA). Aliquots (4 μl) of this raw bacterial target were cast on each capture probe-modified sensor for 15 min, followed by hybridization with SH-DP-Ag NPs, and washing, dissolution and detection steps. All procedures were carried out at

room temperature.

2.2.2.7 Nanomotor motion-based readout for hybridization detection

Silver-ion-induced motion-based sensing protocol described earlier[30] was used for detecting DNA and *E. coli* 16S rRNA. For this purpose, 5 μl of H_2O_2 (30%) was dropped on the sensor modified with the sandwich-hybridized duplexes for 2 min to dissolve Ag NPs to Ag^+. The assay was completed by mixing the above Ag^+ enriched H_2O_2 fuel solution with equal volume of freshly prepared nanomotors in ultrapure water. The resulting mixed solution was then added to the glass slide for immediate video acquisition and tracking. Nanomotors were tracked following the protocol reported earlier.[30,45] An inverted optical microscope (Nikon Instrument, Eclipse TE2000-S) equipped with a 40x objective, a Photometrics CoolSnap CF camera (Roper Scientific) and MetaMorph 7.1.7 software (Molecular Devices) was used for capturing videos at a frame rate of 10 fps. This software calculates the instantaneous velocity by tracking the object's center-to-center displacement from frame to frame. Usually, five videos from randomly selected glass slide areas (200 μm×200 μm) were recorded to ensure accurate population sampling. Approximately, 20 random nanomotors were tracked for 50 frames to obtain a representative nanomotor speed. Bonferroni-corrected analyses of variance (ANOVAs) ($P < 0.05$) and power calculations were performed on all data sets to determine the detection limit and identify statistically significant concentrations.

2.2.3 DNA Sensing Results and Discussion

2.2.3.1 Motion-based nucleic acid detection assay

The principle behind motion-based nucleic acid detection using catalytic nanomotors is illustrated in Figure 2.2.1. Initially, a gold electrode is modified with a ternary monolayer composed of a thiolated capture probe (SH-CP), mercaptohexanol (MCH) and dithiothreitol (DTT). The presence of a complementary nucleic acid target leads to duplex formation and subsequent capture of a SH-DP-Ag NP. After the washing step to remove the excess unbound SH-DP-Ag NPs, hydrogen peroxide is added, leading to rapid dissolution of the captured nanoparticle tags into silver ions. The Ag^{+}-enriched fuel is separated from the surface of DNA modified gold electrode and directly added to an equal volume of freshly prepared nanomotor solution, thereby leading to a change in their speed and hence to concentration-dependent nanomotor distance signals. Such signals can be easily and directly traced using optical microscopes, hence obviating the need for sophisticated analytical instruments.

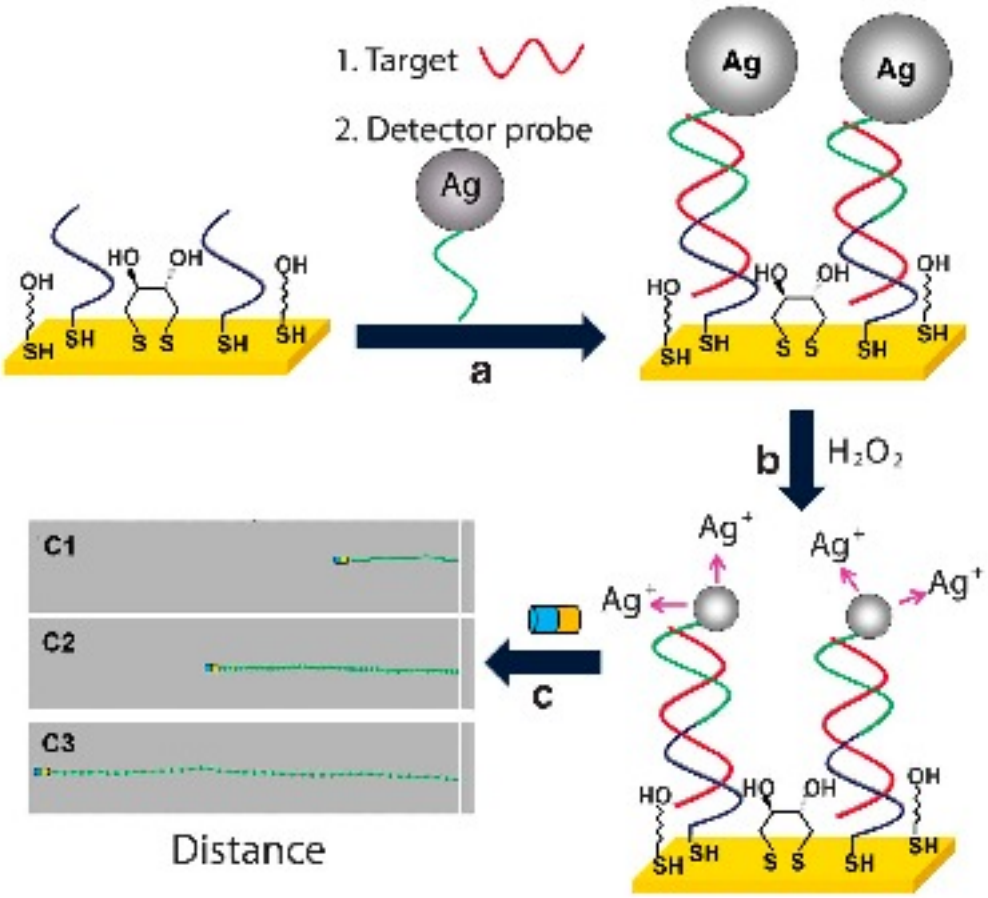

Figure 2.2.1 Motion-based nucleic acid detection. (a) Hybridization of the target and capture of the Ag nanoparticle-tagged detector probe in a typical sandwich assay on the ternary SH-CP/DTT + MCH surface, including washing of unbound SH-DP-Ag NPs. (b) Dissolution of silver nanoparticle tags in the peroxide fuel, leading to Ag+-enriched fuel. (c) Visual detection of the motion of the catalytic nanowire motors in the resulting Ag+-enriched fuel. C1, C2 and C3 represent hypothetical and increasing target nucleic acid concentrations.

2.2.3.2 Ag NP-induced nanomotor acceleration

Silver nanoparticle tags, commonly used in optical[34] or electrochemical[28] DNA detection, are rapidly dissolved in the hydrogen peroxide fuel and the resulting silver ions lead to a dramatic speed increase in nanomotors, in accordance with early observations.[30] The accelerated motion of catalytic nanomotors in the presence of Ag NPs is illustrated in Figure 2.2.2a–c. It compares traces of three Au–Pt nanomotors, taken over a period of 1 s, in the presence of 10% H2O2 fuel without (Fig. 2.2.2a) and

with 40pM Ag NPs (Fig. 2b). The nanowires exposed to nanoparticles travel substantially longer distances compared with those present in the fuel solution not containing nanoparticles (49.2 versus 7.7μm; Fig. 2c), thereby reflecting a 6.4-fold speed enhancement. The complete and instantaneous dissolution of Ag NPs in the peroxide fuel was confirmed by UV–Visible spectroscopy (Figure 2.2.3). A silver ion concentration of 40 μM was estimated from the number of ions released by a 40 pM silver nanoparticle solution (based on the packing density ratio). The speed increase (to around 50μms−1) observed for this Ag^{+} concentration correlates well with the expected silver effect.[30]

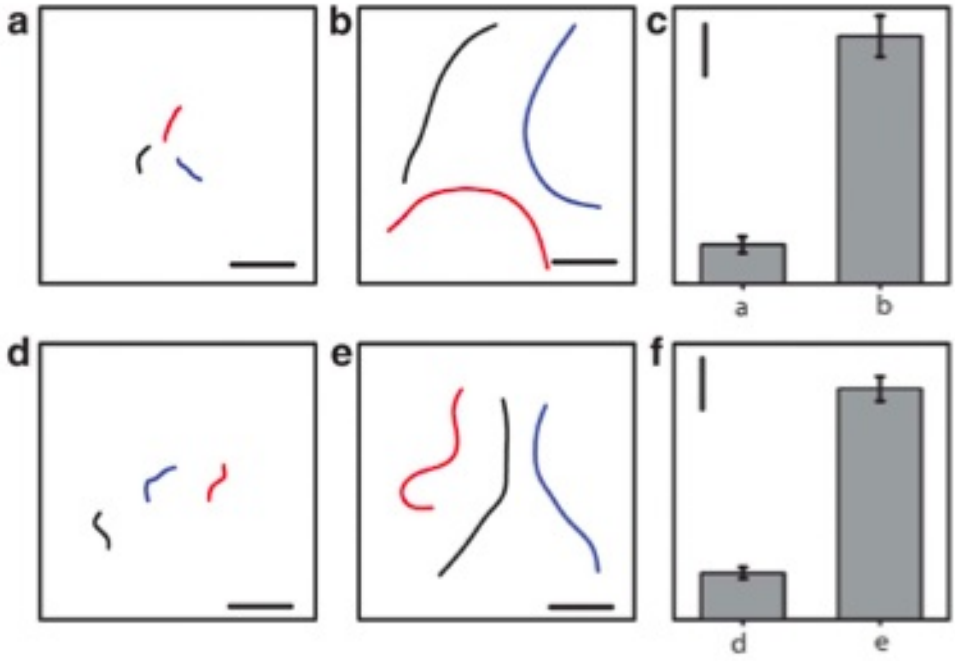

Figure 2.2.2 Tag-induced nanomotor acceleration. Track lines of nanomotors illustrating the distances travelled by three Au–Pt nanowires over a 1 s period in the presence of 10% H2O2 (a) and 10% H2O2 containing 40 pM Ag nanoparticles (b). Scale bar, 10 μm. The corresponding column graphis shown in c. Traces of three nanomotors over a 1 s period in the presence of 15% H2O2 following complete hybridization assays using 0 nM (d) and 100 nM target DNA (e). The corresponding column graph is shown in f. Error bars estimated as a triple of the standard deviation (n = 20).

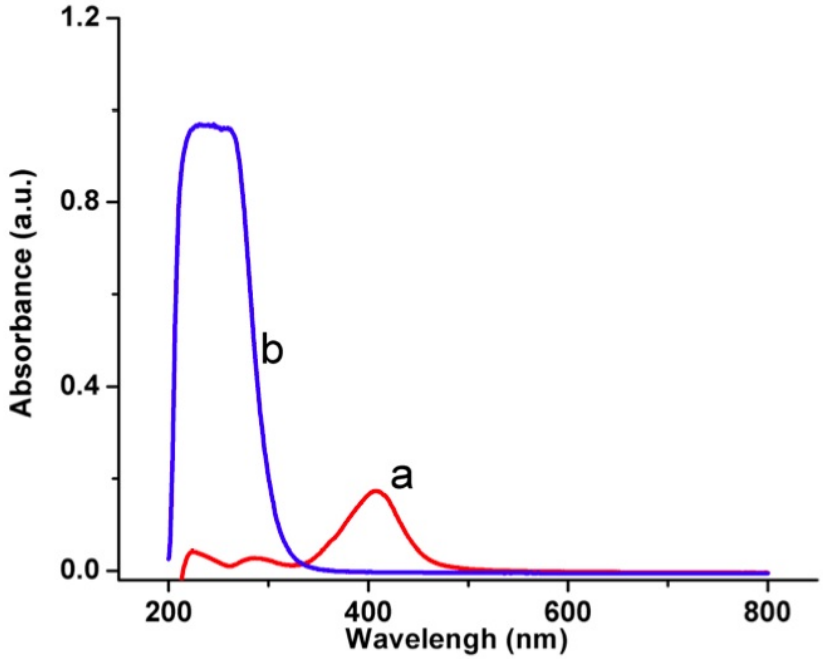

Figure 2.2.3 Spectra illustrating complete dissolution of Ag nanoparticles. Spectra for 400 pM Ag nanoparticles water solution recorded **(a)** before and **(b)** after adding the 10% H2O2 solution. (Spectra was taken after diluting the 30 µl parent solution to 500 µl using distilled water).

2.2.3.3 Motion-based detection of DNA and *Escherichia coli* 16S rRNA

The instantaneous dissolution of metal nanoparticles in the fuel solution and the resulting silver-induced accelerated motion are the bases for using nanomotors to detect nucleic acid hybridization. Figure 2.2.2d–f compares traces of three Au–Pt nanomotors swimming (over a period of 1s) in the peroxide fuel solution after complete hybridization assays with 0 and 100 nM DNA target (Fig. 2.2.2d, e, respectively). The 100 nM DNA target leads to an average travel distance of 45.9 µm (Fig. 2.2.2e), compared with the 9.2 µm signal observed for the control hybridization experiment without target (Fig. 2.2.2d). Similar traces recorded for intermediate DNA target concentrations of 10 pM, 100 pM, 1 nM and 10 nM yielded increasing speeds of 11.5, 18.7, 24.9 and 31.5 µm/s, respectively. The resulting calibration plot (Figure

2.2.4) shows a clear concentration dependence.

Straight-line distance signals of 'racing nanomotors', accomplished by incorporating a ferromagnetic nickel segment into the nanowire motors[36] along with a directed magnetic alignment, provide an extremely convenient and attractive quantitation of the DNA targets. The optical images of Figure 2.2.4a illustrate such straight-line hybridization signals, recorded over a 4s period, for 4 μl samples containing increasing levels of the DNA target over the 40 amol–400 fmol range (that is,10 pM – 100 nM), along with the control (0 DNA) solution. Such directional motion control allows for a clear visual comparison of the distance readouts of the different DNA concentrations. As expected, longer signals—ranging from 37.2 to 144.0μm — are observed upon increasing the DNA concentration. A well-defined concentration dependence is therefore obtained over the broad 40 amol – 0.4 pmol range (Fig. 2.2.4a) Straight-line distance signals of the Au–Ni–Au–Pt nanomotors in connection with the different DNA concentrations, and hence the attractive performance of the new motion bio-detection platform. The nanomotor distance signal for the 40 amol DNA solution was shown to be statistically different when compared with a control, with an average speed of 9.3 μm/s (versus 7.3 μm/s, respectively). This detection limit compares favorably with those reported for other nanostructure-based DNA assays.[23] Such a value is particularly impressive, considering the simplicity of the developed methodology and the absence of any deliberate amplification protocol, such as Ag enhancement or target PCR. Even lower levels of the DNA target could be detected by recording the distance signals over longer time, thereby making small concentration

differences more discernable (in a manner reminiscent of increasing the electrophoresis gel running time to distinguish between similarly sized fragments).

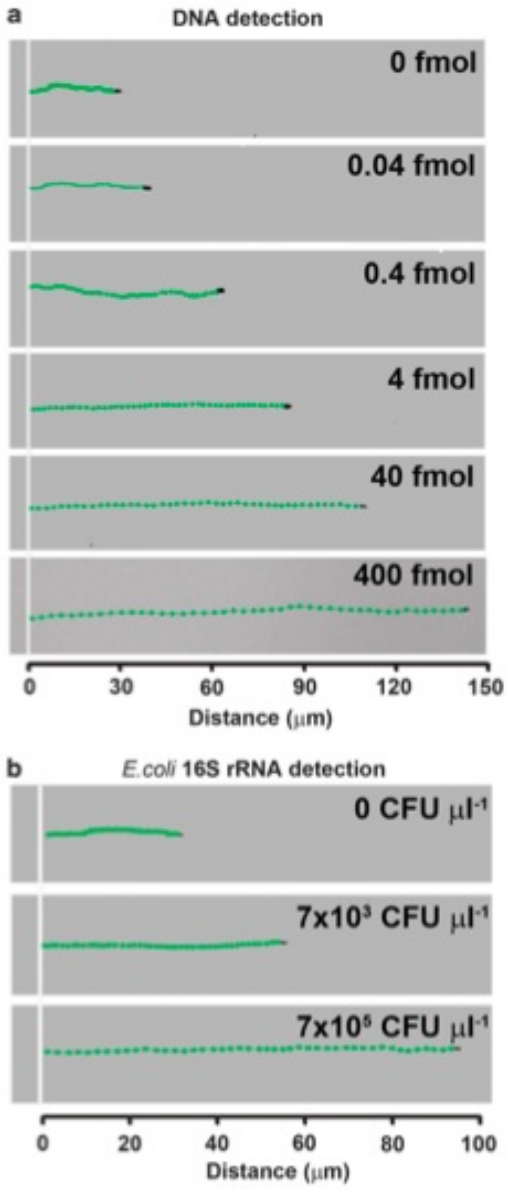

Figure 2.2.4 Nanomotor racing for quantitative nucleic acid detection. Motion-based DNA detection of different levels of synthetic target (a) and of E. coli 16S rRNA (b) corresponding to different cell concentrations (CFU, colony-forming units). Optical images superimposed with straight-line track lines illustrating the distance travelled by the corresponding Au–Ni–Au–Pt nanomotors over a 4 s period.

The practical utility of this new motion-driven DNA assay was illustrated using the same capture and detector probe for the detection of 16S rRNA which is released from *E. coli* pathogenic bacteria and obtained from a previously reported sample preparation.[37,38] Figure 2.2.4b and Supporting Video 2.2 show catalytic nanomotors 'racing' following hybridization assays using different bacterial lysate solutions corresponding to different *E. coli* cell concentrations: 0, 7×10^3 and 7×10^5 CFU/μl, leading to average distance signals of 32, 56 and 96 μm, respectively (Fig. 2.2.4b). The results indicate a sensitive detection of the genetic material corresponding to around 2,000 *E.coli* CFU/μl level.

2.2.3.4 Specificity and precision studies

The specificity of the motion- sensing protocol was examined by challenging the system with excess of various non-complementary and mismatched oligonucleotides. Figure 2.2.5 shows distance signals to 0 (a), 100pM (c) and 10 nM (f) of target DNA, along with the nanomotor response to a large excess of non-complementary and mismatched oligonucleotides (b, d and e). As expected, the system responds favorably to the target DNA with well-defined distance signals of 18.7 and 31.5 μm for the 100 pM and 10 nM levels, respectively. In contrast, a huge excess (1μM) of non-complementary (Fig. 2.2.5 b) and three-base mismatched (Fig. 2.2.5 d) oligonucleotides displays a negligible change in the response (compared with the control signal without the nucleic acid; Fig. 2.2.5 a). Only the two-base mismatched DNA (Fig. 2.2.5 e) yields a defined signal of 14.7μm (compared with 31.5μm for a similar level of the complementary DNA target, Fig. 2.2.5 f). Such

response reflects the partial duplex formation of the mismatch, hence the capture of the Ag NP 'accelerating' tags. The movement of nanomotors after hybridization assays with 1000 nM non-complementary oligonucleotides, 0 nM (control experiment) and 100 pM of target DNA revealed significant movement in target samples when compared to the excess controls. Overall, the data of indicates that the motion detection platform offers high specificity, reflecting the negligible non-specific adsorption of the SH-DP-Ag NPs onto the mixed self-assembled monolayer on the gold surface. The small background contributions compare favorably with those of analogous nanoparticle-based bioassays.[34,35] Further discrimination against more closely mismatched oligonucleotides, such as single mismatched DNAs, could be achieved by stringent control of hybridization conditions or by using highly specific peptide nucleic acid capture probes.[39]

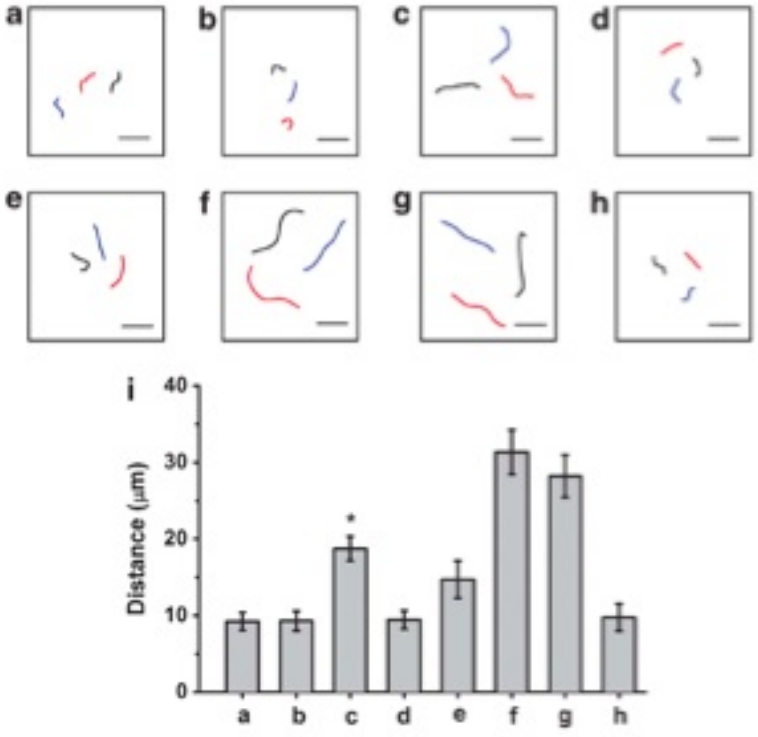

Figure 2.2.5 Specificity of the motion-driven nucleic acid detection. Track lines illustrating the distances travelled by three nanomotors over a 1 s period in 15% H2O2 after hybridization with 0 nM target DNA (normal control) (a), large excess (1 μM) of a non-complementary DNA (b), 100 pM of the DNA target (c), large excess (1 μM) of a three- base mismatched oligonucleotide (d), 10 nM two-base mismatched oligonucleotide (e), 10 nM target DNA (f), 16S rRNA corresponding to 5×105 CFU μl − 1 E. coli (g) and 16S rRNA corresponding to 7×105 CFU μl − 1 K. pneumoniae (h). Scale bar, 10 μm. The corresponding column graph was shown in i. Error bars estimated as a triple of the standard deviation (n = 20). *Indicates a significance value of $P < 0.001$.

The specificity of the motion-driven bioassay was also tested using a biological control, *Klebsiella pneumoniae*, another Gram-negative pathogenic Enterobacteriaceae.[40] As illustrated in Figure 2.2.5 g, h, and contrary to the signal of *E.coli* 16S rRNA (average speed of 28.2 μm/s, Fig. 2.2.5 g), the nanomotor response to the presence of *K. pneumoniae* 16S rRNA (average speed of 9.7 μm/s, Fig. 2.2.5 h) is similar to that observed for the negative control (without target, average speed of 9.2 μm/s, Fig. 2.2.5 a). This shows the high specificity of the motion bioassay towards the *E. coli* 16S rRNA target (versus other non- complementary bacterial RNAs) and to

the absence of non-specific adsorption of SH-DP-Ag NPs. These results show the high specificity of the selected capture probe for binding only 16S rRNA in *E. coli* lysates, despite the potential conservation of the 16S rRNA gene.

The precision of the new motion-driven biodetection platform was also examined. Well-defined and reproducible speed signals are observed, leading to a favorable relative standard deviation of 5.66% (n=10). Similarly, nanomotor speed variability between three different experimental batches revealed negligible differences ($P < 0.05$) in connection with the 1 nM DNA target.

2.2.4 DNA Sensing Conclusions

We have shown the first example of practical realization of synthetic nanomotors as a bioanalytical tool, in connection with the detection of DNA and bacterial rRNA. Such motion-based DNA sensing relies on the use of an optical microscope for directly tracking changes in the speed of unmodified nanowire motors. The silver-ion-induced nanomotor acceleration reflects the sandwich formation among the capture probe, complementary target and the SH-DP-Ag NPs. The nanoparticle-induced nanomotor acceleration reflects the dramatically enhanced speed of catalytic nanomotors in the presence of silver ion. The resulting motion-driven biodetection strategy offers sensitive and selective, easily measured distance readouts down to the 40 amol DNA level and the ability to directly detect raw bacterial ribosomal RNA without isolation or purification steps. Unlike common nanoparticle-based silver enhancement DNA optical[34] or electrochemical[35] hybridization assays, the nanomotor method requires no such particle enlargement (and hence is not susceptible to non-

specific Ag precipitation) and relies on portable, simple and low-cost instrumentation. Motion-based biosensing can be expanded to multiplexed measurements of multiple targets by encoding functionalized nanomotors with a multi-stripe barcode segment. The template nanowire preparation route allows adding a multistripe Ag–Au section to the Au–Pt nanomotor, thus facilitating rapid reflectivity identification. An internal standard could also be used in the new motion detection to facilitate the quantitation of the nucleic acid target and address rare potential variations between nanomotor batches. It is also worth noting that the new nanomotor speed transduction facilitates the collection of multiple readings in a single experiment, thereby contributing to the overall reliability of the proposed protocol. The sensitivity and selectivity could be even further enhanced by recording the distance signals over longer periods of time and by using specific peptide nucleic acid probes, respectively. As the sensitivity of real-life nucleic acid measurements is commonly limited by non-specific adsorption signals, we used here a new multi-component ternary monolayer that effectively minimizes such non-specific background contributions compared with commonly used binary monolayers. A huge excess of non-complementary DNA or rRNA from a different bacteria thus has a negligible effect on the fully complementary target (DNA or rRNA) distance signals.

Motion-driven biosensing represents a new paradigm in bioanalysis, as it relies for the first time on speed and distance as the analytical signals. Although the concept has been presented in connection with motion-based DNA biodetection and Ag NP tags, it may be extended to the detection of a broad range of target biomolecules in

connection with different biomolecular interactions and motion transduction principles. Such new approaches to transduce the biomolecular recognition event into nanomotor motion are currently being examined in our laboratory. The distance signals can be translated into analytical results using low-cost microscopic readers, thereby making the new method affordable and attractive for low-resource settings. Owing to its attractive features, we expect that the new motion-based signal transduction will lead to a host of new and powerful biosensing applications, including clinical diagnostics, biothreat detection, food safety and forensic analysis.

Chapter 2.1 is based, on the material as it appears in JACS, 2009, by Daniel Kagan, Percy Calvo-Marzal, Shankar Balasubramanian, Sirilak Sattayasamitsathit, Kalian Manesh, Gerd Flechsig and Joseph Wang; and Chapter 2.2 is based on material from Nature Communications 2009, by Shankar Balasubramanian, Daniel Kagan, Kalian Manesh, Percy Calvo-Marzal, Gerd Flechsig, and Joseph Wang; in part on material from Chemical Communications, 2010, by Jie Wu, Shankar Balasubramanian, Daniel Kagan, Kalian Manesh, Susana Campuzano, and Joseph Wang. The dissertation author was the primary investigator and co-author of these papers.

2.3 References

1. Kline, T. R.; Paxton, W. F.; Mallouk, T. E.; Sen, A. *Angew. Chem., Int. Ed.* **2005**, *44*, 744.

2. Wang, J. *ACS Nano* **2009**, *3*, 4-9.

3. Ozin, G. A.; Manners, I.; Fournier-Bidoz, S.; Arsenault, A. *Adv. Mater.* **2005**, *17*, 3011.

4. Paxton, W. F.; Sen, A.; Mallouk, T. E. *Chem. Eur. J.* **2005**, *11*, 6462.

5. Burdick, J.; Laocharoensuk, R.; Wheat, P. M.; Posner, J. D.; Wang, J. *J. Am. Chem. Soc.* **2008**, *130*, 8164.

6. Calvo-Marzal, P.; Manesh, K. M.; Kagan, D.; Balasubramanian, S.; Cardona, M.; Flechsig, G.-U.; Posner, J.; Wang, J. *Chem. Commun.* **2009**, 4509.

7. Wang, Y.; Hernandez, R. M.; Bartlett, D. J.; Bingham, J. M.; Kline, T. R.. Sen, A.; Mallouk, T. E. *Langmuir* **2006**, *22*, 10451.

8. Paxton, W. F.; Baker, P. T.; Kline, T. R.; Wang, Y.; Mallouk, T. E.; Sen, A. *J. Am. Chem. Soc.* **2006**, *128*, 14881.

9. Mascaro, L. H.; Santos, M. C.; Machado, S. A. S.; Avaca, L. A. *J. Chem. Soc., Faraday Trans.* **1997**, *93*, 3999.

10. Orendorff, C. J.; Murphy, C. J. *J. Phys. Chem. B* **2006**, *110*, 3990.

11. Niidome, Y.; Nakamura, Y.; Honda, K.; Akiyama, Y.; Nishioka, K.; Kawasaki, H.; Nakashima, N. *Chem. Commun.* **2009**, 1754.

12. Demirok, U. K.; Laocharoensuk, R.; Manesh, K. M.; Wang, J. *Angew. Chem., Int. Ed.* **2008**, *47*, 9349.

13. Yamazaki, S.; Siroma, Z.; Senoh, H.; Ioroi, T.; Fujiwara, N.; Yasuda, K. *J. Power Sources* **2008**, *178*, 20.

14. Ibele, M.; Mallouk, T. E.; Sen, A. *Angew. Chem., Int. Ed.* **2009**, *48*, 1.

15. Anderson, J. *Annu. Re*V. *Fluid Mech.* **1989**, *21*, 61.

16. Howse, J. R.; Jones, R. A. L.; Ryan, A. J.; Gough, T.; Vafabakhsh, R.; Golestanian, R. *Phys. Re*V. *Lett.* **2007**, *99*, 048102.

17. Laocharoensuk, R., Burdick, J., Wang, J., *ACS Nano* **2008,** *2*, 1069.

18. Piunno, P. A. E.; Krull, U. J.; Hudson, R. H. E.; Damha, M. J.; Cohen, H. *Anal. Chem.* **1995***. 67,* 2635–2643.

19. Ferguson, J. A.; Boles, T. C.; Adams, C. P.; Walt, D. R. *Nat. Biotechnol.* **1996***, 14,* 1681–1684.

20. Wang, J. *Nucl. Acids Res.* **2000***, 28*, 3011–3016.

21. Gooding, J. J. *Electroanalysis.* **2002***, 14,* 1149–1156.

22. Okahata, Y.; Matsunobu, Y.; Ijiro, K.; Mukae, M.; Murakami, M.; Makino, K. *J. Am. Chem. Soc.* **1992***, 114*, 8299–8300.

23. Rosi, N. L.; Mirkin, C. A. *Chem. Rev.* **105***, 2005*, 1547–1562.

24. Wang, J. *Small,* **2005** *1,* 1036–1043.

25. Mallouk, T. E.; Sen, A. *Sci. Am.* **2009***, 300,* 72–77.

26. Ozin, G. A.; Manners, I.; Fournier-Bidoz, S.; Arsenault, A. *Adv. Mater.* **2005***, 17,* 3011–3018.

27. Wang, J. *ACS Nano.* **2009***, 3,* 4–9.

28. Paxton,W.F.; Kistler, K.; Olmeda, C.C.; Sen, A.; Angelo, S.A.; Cao, Y.; Mallouk, T.E.; Lammert, P.E.; Crespi, V.H. *J. Am. Chem. Soc***. 2004** *126,* 13424–13431.

29. Mirkovic, T.; Zacharia, N. S.; Scholes, G. D.; Ozin, G. A.; *Small* **2010** *6,* 159–167.

30. D. Kagan, P. Calvo-Marzal, S. Balasubramanian, S. Sattayasamitsathit, K. M. Manesh, G.-U. Flechsig and J. Wang, *J. Am. Chem. Soc.*, 2009, **131**, 12082–12083.

31. York, J.; Spetzler, D.; Xiong, F.; Frasch, W. D.; *Lab Chip* **2008***, 8*, 415–419.

32. Fischer, T.; Agarwal, A.; Hess, H.; *Nat. Nanotechnol.* **2009***, 4,* 162–166.

33. Hess, H.; Bachand, G. D.; *Mater. Today* **2005***, 8,* 22–29.

34. Cao, Y. W. C.; Jin, R. C.; Mirkin, C. A.; *Science* **2002***, 297*, 1536–1540.

35. Wang, J.; Polsky, R.; Danke, X.; *Langmuir* **2001***, 17,* 5739–5741.

36. Liao, J. C. Mastali, M.; Gau, V.; Suchard, M.A.; Moller, A.K.; Bruckner, D.A.; Babbitt, J.T.; Li, Y.; Gornbein, J.; Landaw, E.M.; McCabe, E.R. Churchill, B.M.; Haake, D.A.; *J. Clin. Microbiol.* **2006,** *44,* 561–570.

37. Wu, J.; Chumbimuni-Torres, K.Y.; Galik, M.G.; Thammakhet, C.; Haake, D.A.; Wang, J.; *Anal. Chem.* **2009***, 81,* 10007–10012.

38. Wang, J.; Nielsen, P.E.; Jiang, M.; Cai, X.; Fernandes, J.R.; Grant, D.H.; Ozsoz, M.; Beglieter, A.; Mowat, M.; *Anal Chem.* **1997,** *69,* 5200– 19.

39. Kline, T. R.; Paxton, W. F.; Mallouk, T. E.; Sen, A.; *Angew. Chem. Int. Ed*. **2005**, *44*, 744–746.

40. LaGier, M. J.; Scholin, C.A.; Fell, J.W.; Wang, J.; Goodwin, K.D.; *Mar. Pollut. Bull.* **2005***, 50,* 1251–1261.

41. Tokareva, I.; Hutter, E.; *J. Am. Chem. Soc.* **2004***, 126,* 15784–15789.

43. Thompson, D. G.; Enright, A.; Faulds, K., Smith, W. E.; Graham, D.; *Anal. Chem.* **2008***, 80,* 2805–2810.

44. Lee, J. S.; Lytton-Jean, A. K. R.; Hurst, S. J.; Mirkin, C. A.; *Nano. Lett.* **7***, 2007,* 2112–2115.

45. Pal, S.; Sharma, J.; Yan, H.; Liu, Y.; *Chem. Commun.* **2009,** *40,* 6059–6061.

Chapter 3 Biomolecule and Cell Isolation by Synthetic Nanomotors

3.1 DNA Isolation

3.1.1 DNA Isolation Introduction

Nucleic acid extraction is the critical first step for many biomedical and clinical diagnostic applications. While numerous methods have been developed for macroscale nucleic acid extraction, their adaptation to microscale devices is challenging and requires fundamentally new concepts to address their requirements of high efficiency, simplicity, low sample volumes, and low cost.[1,2] In this section we describe the use of self-propelled micromachines that are functionalized with a nucleic acid probe to selectively and rapidly capture, isolate, and transport target nucleic acids from raw biological samples to a clean location for subsequent analysis without sample processing steps. Recent advances in chemically powered synthetic nanomotors[3-8] have made these devices promising tools for addressing many biological challenges. For example, we illustrated directed drug delivery[9] and motion

based sensing and biosensing[10,11] based on the use of catalytic nanowire motors. Previously, functionalized biomotors (kinesin) have demonstrated the ability to transport DNA strands along microtubule tracks in artificial environments.[12,13] However, these biological nanomotors have yet to demonstrate biomolecular isolation in complex biological matrices.

3.1.2 DNA Isolation Experimental Methods

3.1.2.1 Reagents and Solutions

6-Mercaptohexanol (MCH) and sodium cholate (NaCh) were purchased from Sigma- Aldrich. Bovine serum albumin (BSA), human serum (from human male AB plasma), KCl, Na2HPO4, K2HPO4.3H2O and NaCl were purchased from Sigma-Aldrich. Streptavidin-Coated Fluorescence Microspheres (210 nm mean diameter CP01F/8905) were purchased by Bangs Laboratories Inc. Reagents were used without any further purification.

All synthetic oligonucleotides used were purchased from Integrated DNA Technologies Inc. (San Diego, CA) and are listed in Supporting Table S2 of the Supporting Information. Bacterial strains of *Escherichia coli* NEB 5-α (New England Biolabs) and clinical isolates of *K. pneumoniae* (KP210) were obtained from the University of California-Los Angeles (UCLA), Clinical Microbiology Laboratory, with approval from the UCLA and Veterans' Affairs institutional review boards and appropriate Health Insurance Portability and Accountability Act exemptions. The isolates were received in centrifuge tubes and were stored at -80 °C until use.

Overnight bacterial cultures were freshly inoculated into Luria broth (LB) and grown to logarithmic phase as measured by the optical density at 600 nm. Concentrations in the logarithmic-phase specimens were determined by serial plating.

The buffer solutions used in this study were as follows: the DNA immobilization buffer (IB) was 1XPBS (pH 7.2) and the hybridization buffer (HB) was a 1 M phosphate buffer solution containing 2.5% (w/v) bovine serum albumin (pH 7.2). All chemicals used were of analytical-grade reagents, and deionized water was obtained from a Millipore Milli-Q purification system (18.2 MΩ cm). Human urine and saliva samples were collected daily and diluted appropriately in HB just before the experiment.

3.1.2.2 Microrockets fabrication

The Ti/Ni/Au/Pt microtube rockets were prepared by modifying previously reported lithographic protocols.[14,15] Briefly, a positive photoresist (Microposit S1827, Microchem, Newton, MA) which serves as a sacrificial layer, was spin-coated on a silicon wafer at 3000 rpm for 60 seconds. The coated-wafer was baked at 115 °C for 60 seconds and exposed to UV light with an MA6 mask aligner for 35 seconds to create pre-defined patterns. Exposed patterns were developed using a MF-321 developer for 90 seconds and thoroughly washed with DI water. Metallic layers of Ti: 10 nm, Ni: 15 nm, Au: 5 nm and Pt: 10 nm were deposited sequentially using an e-beam evaporator under high vacuum conditions (<10-4 Pa). The e-beam substrate holder was tilted to 50° in order to asymmetrically deposit metals on the patterns.

Upon selective removal of the exposed photoresist layer using MF-1165 (Rohm & Haas, Marlborough, MA), the prestressed metallic layers self-assemble into microtubes. The microrockets were washed and stored in isopropanol before undergoing critical-point drying to maintain structural integrity. A thin (~60 nm) gold layer was sputtered onto the rolled-up microtubes to facilitate surface functionalization with the binary SHCP+MCH self-assembly monolayer (SAM).

3.1.2.3 Microrockets modification

The external gold surface of the microrockets was modified by an overnight immersion in a 10 μM SHCP solution prepared in IB. After washing with ultrapure water, the microrockets modified with the SHCP were treated with a 0.1 mM MCH solution (also in IB) for 10 min to obtain a SHCP+MCH SAM. Finally, the modified microrockets were washed for 60 s with ultrapure water, entirely detached from substrates and placed in IB. All incubation steps were carried out at room temperature. It is important to note that such SHCP+MCH-modified microrockets can be used for isolation of nucleic acid if they are stored (up to 2 weeks) in IB at 4^{o}C.

3.1.2.4 DNA isolation and detection

The DNA isolation and detection protocol involved a duplex formation between the microrocket-surface confined probe and the biotinylated target DNA labeled with the streptavidin-fluorescence particle tag. Different concentrations of the DNA target were prepared in the HB and incubated for 30 min at room temperature with the commercial streptavidin- fluorescence particles diluted 60 times before

exposure to the modified-microrockets. The same protocol was used for the testing with the NC or 3-MM sequences. Experiments were carried out at room temperature.

3.1.2.5 Bacterial 16S rRNA isolation and detection

The bacteria detection strategy involves "sandwich" hybridization of target 16S rRNA released from the bacterial cell to specific capture and detector probes. The bacteria were lysed by resuspension of the appropriate pellet containing ~107 CFU bacteria in 10 μL of 1 M NaOH and incubation for 5 min.[16,17] A 50 μL of Biotin-DP (0.25 μM) in HB was added to this 10 μL bacterial lysate, leading to genetic material corresponding to ~107 CFU per 60 μL. This solution was left to incubate 15 min at room temperature (for homogeneous hybridization in solution) and seriallydiluted in the Biotin-DP (0.25 μM) to provide different concentrations of bacterial genetic material (16S rRNA). The resulting solution was incubated with the fluorescence particle tags following the same protocol described earlier for the synthetic target DNA. All procedures were carried out at room temperature.

3.1.2.6 Isolation of target nucleic acid from complex samples

A mixture of SHCP+MCH-modified microrockets (2 μL), sodium cholate (0.1-1.0% (w/v) in IB, 2 μl) and samples under study (2 μL) was added to a freshly cleaned glass slide. To this, 2 μL of nucleic acid solution (synthetic DNA or bacterial rRNA conjugated with the fluorescence nanoparticles) and 2 μL of H2O2 were added (final peroxide concentration ranging between 1 to 5% (w/v) depending on the matrix samples assayed). The microrockets were allowed to move randomly in the above

solution to pick up the target nucleic acid during the desired time and in the moment of video acquisition the microrockets were magnetically guided to localize them in the observation window. Videos were captured using CoolSNAP HQ2 camera, 20×objective (unless mentioned otherwise) and acquired at the frame rate of 10 using the Metamorph 7.1 software (Molecular Devices, Sunnyvale, CA). A Nikon Eclipse 80i upright microscrope with B2-A FITC filter was used to capture fluorescence images and videos. An estimation of the captured nucleic acid-tagged particles coverage on the microrocket is provided by analyzing the corresponding time lapse images using the software ImageJ.

3.1.2.7 PDMS channels preparation

Polydimethylsiloxane (PDMS) was hand-mixed in a 10:1 polymer: fixing agent ratio using a commercial Sylgard 184 Silicone elastomer kit (Dow Corning Corporation, Midland, MI). PDMS was poured over a glass Petri dish, degassed in a vacuum desiccator, and baked at 110°C for 15 min. Holes of 3 mm were punched in peach well using a steel rod (Technical innovations, Brazoria, TX). The PDMS network had 2 reservoirs of 3 mm wide and 1.5 mm tall with a channel length of approximately 6 mm. The resultant structures and glass slides were exposed to UVO ozone (Jetline Co., Irvine, CA) at a gas flow rate of 3 sccm for 3 min, pressed together and baked for another 10 min at 110°C to complete the bonding process. The PDMS channel was washed with ultra pure water to ensure the removal of any residual dust and dried properly under nitrogen before starting the experiments.

3.1.2.8 Experiments in PDMS channels

A mixture of the HB and H2O2 (final concentration 3% (w/v))/sodium cholate (final concentration 0.25% (w/v)) was prepared and transferred to the PDMS channel until filling the channel. An appropriate volume of the modified-microrockets and fluorescence labeled-nucleic acid solution (4 μL of each) was added to the 'dirty' well simulating a real sample; a slightly higher volume of the aforementioned mixture was added to the clean well in order to generate a hydrostatic pressure gradient (for minimizing the diffusion from the dirty well to the clean well). After allowing movement of the modified microrockets in the sample well during the desired time, they were magnetically guided across the channel to the 'clean' reservoir. Ambient light and digital adjustments to brightness and contrast were used to visualize the nucleic acid functionalized with the fluorescence tags, micromotor and PDMS channel at the same time. Tracking, magnetic guidance and visualization techniques are the same as described above.

3.1.2.9 Stability of the microrockets' modification and performance of hybridization in the presence of the fuel

In order to validate the stability of the modification and nucleic acid hybridization in the presence of the fuel (5% (w/v) H2O2 and 1% (w/v) NaCh), we performed additional electrochemical experiments.[15] Such experiments were designed to compare the performance of the hybridization with the target DNA in pure HB, in HB containing 5% (w/v) of H2O2, and in HB containing 5% (w/v) of H2O2 and 1%

(w/v) of sodium cholate.

This conventional electrochemical detection strategy involves a sandwich hybridization assay where the immobilized capture probe anchors the target DNA to the sensor, and the detector probe signals the presence of the target through a reporter molecule.[15] Binding of the capture and detector probes to the nucleic acid target creates a three-component "sandwich" complex on the sensor surface. The fluorescein-modified detector probe enables binding of an antifluorescein-conjugated horseradish peroxidase reporter enzyme to the target probe complex. Under the use of a redox enzyme cosubstrate (3,3',5,5' tetramethylbenzidine, TMB) and a fixed potential between the working and reference sensor electrodes, the horseradish peroxidase- mediated redox cycle is detected by the electrochemical sensor in the form of a current. The amplitude of this electroreduction current reflects the concentration of the target-probe complexes on the sensor surface.[19] The presence of H2O2 and sodium cholate had a minimal effect on the background noise, with nearly the same hybridization signal for the 1 nM target DNA. These results confirm that the SHCP+MCH SAM is stable under working conditions used for the microrocket's locomotion and also that the nucleic acid hybridization is not compromised by the presence of the fuel. However, we have noticed that high H2O2 concentrations (>7% (w/v)) caused the catalytic bubbling to occur at both ends. Additionally, increasing the level of the surfactant to 10% (w/v) enhanced the aggregation of fluorescent particles.

3.1.2.10 Estimation of the volume of fluid mixed by the microrockets' bubbling

After measuring the span of the tracer particles affected by 10 microrockets moving at 100 μm/s it appears that the fluid convection at any one time spans 200-300 μm wide, 200-300 μm in length and for the sake of simplicity 200-300 μm in height/depth. This equates to 8-27 nL. Assuming that it travels 100 μm in one second, it will mix a new 4-9 nL every second. It is important to note that the mixing capabilities of the microrockets can vary with the fuel and surfactant concentration as increased level of the surfactant can create a higher number of smaller bubbles but reduce the microrockets' speed,[20] while increased hydrogen peroxide concentration can increase the rate.

3.1.2.11 Performance of microrockets after prolonged movement

Practical nucleic acid isolation applications require that effective motor propulsion is maintained in complex matrices. In order to know the movement capabilities of the modified microrockets we have carried out additional experiments by allowing them to move in different biological samples over longer periods of time. For the prolonged movement of modified microrockets in HB, 100% human serum and 10% urine and saliva we used a 1:4 dilution to include the microrockets and fuel. The speed of most microrockets is only slightly affected by the biological media even after longer periods of time. In some cases the microrockets' speed increased overtime, which could be due to a better wetting of the inner catalytic surface. It should be noted in this point that the fuel concentration required for proper movement of the

microrockets is dependent on the specific biological matrix. Prolonged movement in highly viscous samples like serum and saliva may require slightly higher concentrations of H2O2 and NaCh. Although microrockets can travel and isolate target nucleic acids in undiluted urine and saliva, the biological samples were diluted to statistically measure their speed and effectiveness after 30 minutes (microrockets traveled on average 10 minutes in these undiluted samples). Such modified microrockets, with capability to move in these biological media during longer times, are able to cover distances as long as 10 cm. The relatively large standard deviation is most likely attributed to slight fabrication differences between rockets rather than the effect of the media on the rocket speed. We are exploring ways to develop uniform and efficient microrockets. The capability of prolonged movement may help to scan/raster the same sample many times. This could effectively concentrate the sample and increase the isolation probability in samples containing low levels of the target nucleic acid. Finally, our new 'defect-free' ternary SAM biosensor interfaces,[19] offer remarkable discrimination against non-specific surface interactions.

3.1.2.12 Oligonucleotides Used

All sequences (5' to 3')

Thiolated capture probe, SHCP: Thiol-TAT TAA CTT TAC TCC

Detector probe, Biotin-DP: CTT CCT CCC CGC TGA-Biotin

Complementary target*: Biotin-TCA GCG GGG AGG AAG GGA GTA AAG

TTA ATA

Non-complementary sequence: Biotin-CT GGG GTG AAG TCG TAA CAA GGT AAC CGT AGG GGA AC

NC 3-Base mismatched sequence, 3-MM:Biotin-TCA GCG GGG AGG AAG GGA GTC ACG TGA ATA

*The sequence of the 30-mer complementary target DNA is a copy of partial region of the *E. coli* 16S rRNA gene (position 432-461 according to the 5' to 3' nucleotide sequence). The probe pair (SHCP and Biotin-DP) was designed to be fully complementary to both synthetic target DNA and the partial region of the *E. coli* 16S rRNA targets.[16]

3.1.3 DNA Isolation Results and Discussion

3.1.2.1 Concept

As illustrated in Figure 3.1.1A, our new micromachine-based DNA isolation concept exploits the "on-the-fly" target hybridization onto self-propelled functionalized microrockets. Compared to earlier catalytic nanowire motors, the bubble-based microtube rockets shown here propel efficiently in different untreated biological fluids, which is in agreement with recent reports.[20-23] These microrockets, fabricated using a custom-modified photolithography process,[14,24,25] were sputtered with gold and modified with a binary self-assembled monolayer (SAM) of a specific thiolated capture probe (SHCP) and a short-chain 6-mercapto-1-hexanol (MCH)

(Figure 3.1.1 A,b). Such mixed SAM coating ensures an efficient hybridization process while minimizing nonspecific binding.[26] The probe-functionalized microrockets readily move around within the biological sample (containing the fuel) and interact with the target nucleic acid (synthetic 30-mer DNA or bacterial 16S rRNA) tagged with fluorescent nanoparticles (Figure 3.1.1 A,a). Such tagging allows for optical visualization of the duplex formation on the moving shuttles following short hybridization periods (Figure 3.1.1 B,a), indicating the presence of the target DNA. As illustrated below, the functionalized microrockets can transport the captured target through a microchannel toward a "clean" downstream zone, thus providing dynamic single-step extraction for subsequent analysis.

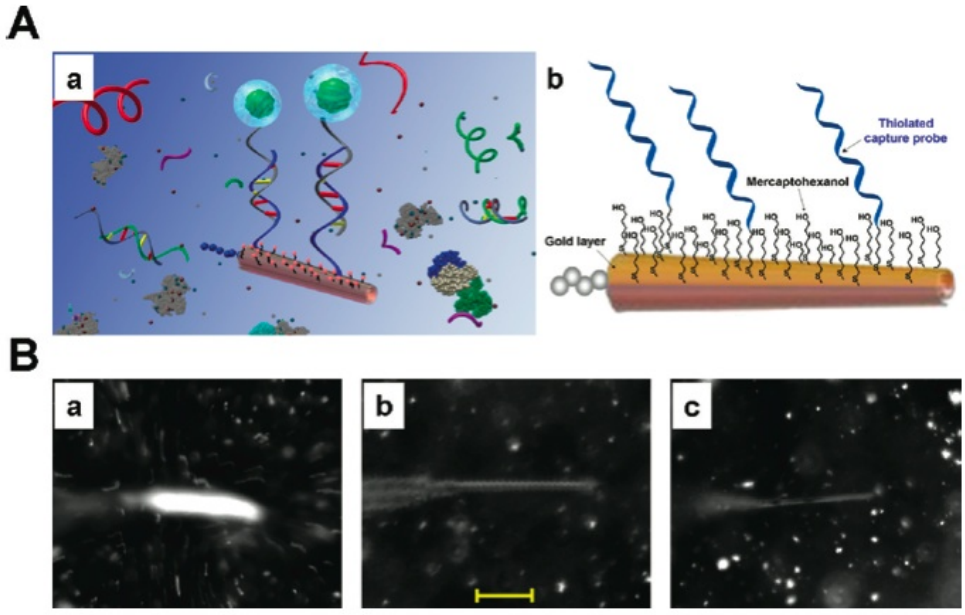

Figure 3.1.1 Motion-based target hybridization and isolation process. (A) Scheme depicting (a) the selective pickup of target nucleic acid from a raw biological sample using a capture-probe-modified microrocket, and (b) surface chemistry involved on the microrockets' functionalization with the binary SAM of SHCP+MCH. (B) Time lapse images illustrating the selectivity and capture efficiency of the SHCP+MCH-modified microrocket toward 25 nM target (a) and 250 nM of 3-MM (b) and NC (c) DNA sequences. Images were obtained after 10 min of incubation in the corresponding solutions, and all experiments were conducted in HB. Scale bar, 30 μm.

The corresponding optical microscope images, shown in Figure 3.1.1 B, illustrate the selective isolation of the fluorescently tagged target DNA sequence (25 nM) by the rapidly moving functionalized microrocket (a), in comparison to control experiments involving a large excess (250 nM) of similarly tagged 3-based mismatched (3-MM) (b) and noncomplementary (NC) (c) DNA sequences. These images were taken 10 min after incubation in their respective samples. The Figure 3.1.1 B(a) clearly demonstrate a highly efficient hybridization of the target DNA to the surface-confined capture probe on the moving microrocket. This is evident from the complete coverage of the microrocket with fluorescent nanoparticles, while the microrocket is moving at 150 μm/s (2.5 body lengths/s). The high specificity of this "on-the-fly" hybridization process can be confirmed from panels b and c of Figure 3.1.1 B where the presence of excess fluorescently labeled 3-MM or NC DNA sequences does not produce any visible binding on the modified-microrocket surface. Even longer incubation times of 25–30 min in the presence of the large excess of these nonfully cDNA sequences did not produce visible capture of the fluorescent tags (not shown). Such effective discrimination against nontarget sequences allows for the highly selective isolation of nucleic acid targets from unprocessed complex biological fluids.

3.1.2.2 Modification

It is also important to note that the composition of the hybridization buffer (high ionic strength and large presence of proteins like BSA) does not compromise the movement of the microrockets. Similarly, the peroxide fuel and sodium cholate (surfactant), which are necessary for microrocket movement[23] do not affect the hybridization efficiency or the integrity of the binary DNA/SAM assembled on the microrockets. This is supported by an independent conventional electrochemical hybridization protocol[19] that yielded similar sensitivities in the presence and absence of hydrogen peroxide and sodium cholate. (See Methods) As will be further illustrated, the movement of the microrockets and the hybridization efficiency are not compromised in unprocessed biological fluids.

3.1.2.3 Convection enhanced isolation

A unique and distinct advantage of this new micromachine DNA isolation, compared to common biomolecular isolation techniques, is the locally induced convection associated with the bubbles generated from the microrocket's end. Using the fluorescent particle tags as tracers, we estimated that each microrocket can move between 4 and 9 nL of fluid per second, depending on the fuel concentration (n = 10). This leads to a favorable hydrodynamic environment for efficient and rapid nucleic acid hybridization compared to common diffusive target transport schemes. Figure 3.1.2 illustrates how modified microrockets incubated with hydrogen peroxide fuel (b, c) dramatically enhance the hybridization efficiency when compared to the same microrockets without the fuel (a). As indicated from Figure 3.1.2c, the fast movement

and generation of bubbles out of the microjet openings lead to small vortexes. Such localized circular fluid movement rapidly mixes and accelerates the mass transfer of the target to the surface probe, resulting in a more efficient hybridization. As a result, the fuel-driven microrockets display about a 13-fold higher number of captured DNA-tagged particles compared to static (Figure 3.1.2a) or artificially shaken ones (based on the corresponding estimated coverages of 7 and 93%, respectively, n = 10; not shown). It is important to note that a micromotor bubbling from both sides was deliberately selected to clearly demonstrate the convection and vortex streams associated with moving microrockets. Such bubble-induced mixing is particularly valuable when microliter sample volumes are involved. Apart from this unique bubbling effect, the fast movement of the micromotor allows for the rapid scanning across samples, therefore increasing the likelihood of contact with the surface-confined probe. This creates a trade-off in the hybridization efficiency when increasing the speed of a unidirectional-bubbling microrocket, i.e., an increase in the distance traveled but a decrease in the convection effect resulting from the microrocket's bubbles. Overall, no major differences in the hybridization efficiency were observed for microrockets moving at different speeds (50–300 μm/s). Additionally, the localized fluid convection directly aids in minimizing nonspecific adsorption of nontarget sequences by shearing off these NC and mismatched nucleic acids (Figure 3.1.1 B).

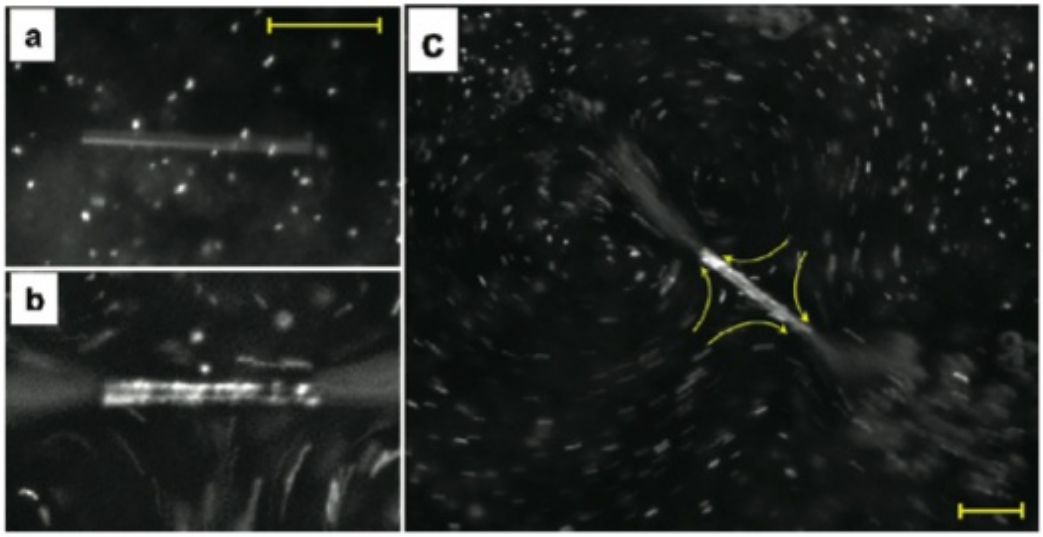

Figure 3.1.2 Micromachine-induced localized convection effects. Time lapse images obtained after a 20 min incubation of the modified microrockets in a HB solution containing the target DNA (25 nM) without (a) and with (b, c) H_2O_2. (c) A larger image illustrating the vortexing effect created around the microrockets by the bubbling propulsion. Scale bar, 30 μm.

3.1.2.4 Time and concentration based isolation

As expected for a hybridization reaction, the quantity of the captured target DNA on the microrocket surface is dependent on its solution concentration and the interaction time. As illustrated in Figure 3.1.3A, the number of captured particles gradually increases upon increasing the hybridization time in the 25 nM target DNA solution. The modified microrocket is almost completely covered by fluorescence nanoparticles after 12 min of incubation time. An estimated relationship between the average coverage of fluorescent particles on the modified microrockets and their navigation time in solution shows that at this target DNA concentration, the coverage increases slowly for the first 5 min and then more rapidly until reaching full coverage after 9 min. This trend reflects the kinetics of the hybridization process. Similarly, and

as shown in Figure 3.1.3B, after 8 min the coverage of fluorescent particles on the modified microrocket increases with the concentration of the DNA target over the 1 and 100 nM range. Although the fluorescent intensity provides a rough quantitative estimation of the target concentration, more accurate nucleic acid quantification would require an appropriate downstream analysis.

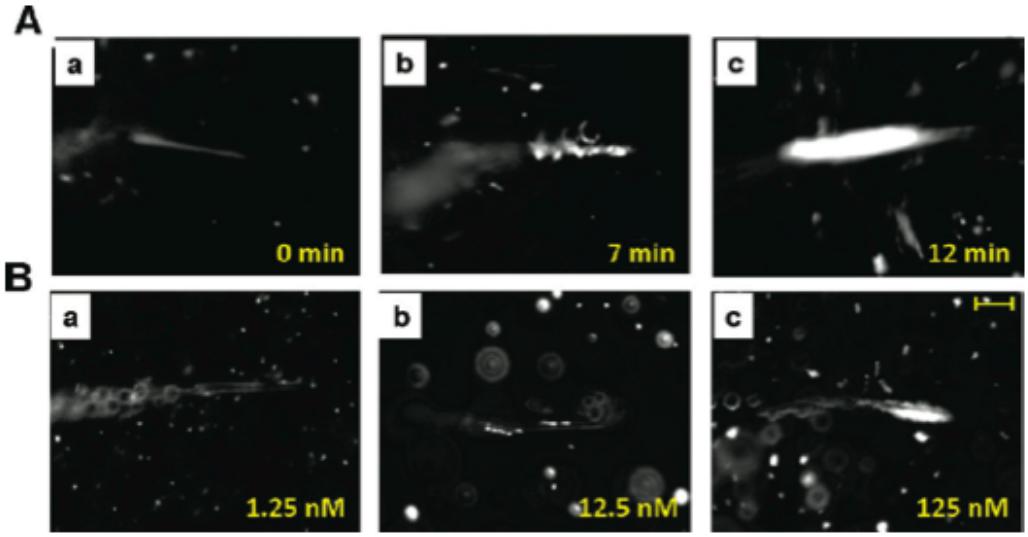

Figure 3.1.3 "On-the-fly" hybridization: Influence of the hybridization time (A) and target concentration (B) upon the hybridization of the fluorescent-tagged target DNA. (A) Time lapse progression of the "on-the-fly" target hybridization (25 nM) onto the moving microrocket following 12 min time in HB. (B) Time lapse images obtained after 8 min exposure of the modified microrockets to different target DNA concentrations in HB. Scale bar, 30 μm.

3.1.2.5 Isolation from Biological Fluids

The propulsion of modified microrockets in complex biological samples such as plasma, urine, or saliva allows for the efficient isolation of target DNA without the need for tedious sample processing steps. In order to demonstrate the ability of the probe-modified microrockets to move and isolate DNA targets in untreated biological fluid samples, nucleic-acid loading was examined in a variety of untreated samples:

100% human serum and 10% human urine and saliva (Figure 3.1.4). As illustrated from the from this figure, the modified microrockets are able to capture target nucleic acids and transport them in these complex biological fluids over long time periods (around 30 min) while maintaining their high speed. It is important to note that the capture efficiency is only slightly dependent on the matrix composition or viscosity. However, in order to consistently obtain prolonged movement of the microrockets (greater than 30 min) different sample dilutions—up to 10-fold for saliva and urine—were used. Note that the efficient propulsion in untreated biological fluids represents a distinct advantage of utilizing bubble-propelled microrockets compared to catalytic nanowire motors which are limited to low ionic-strength environments.[27]

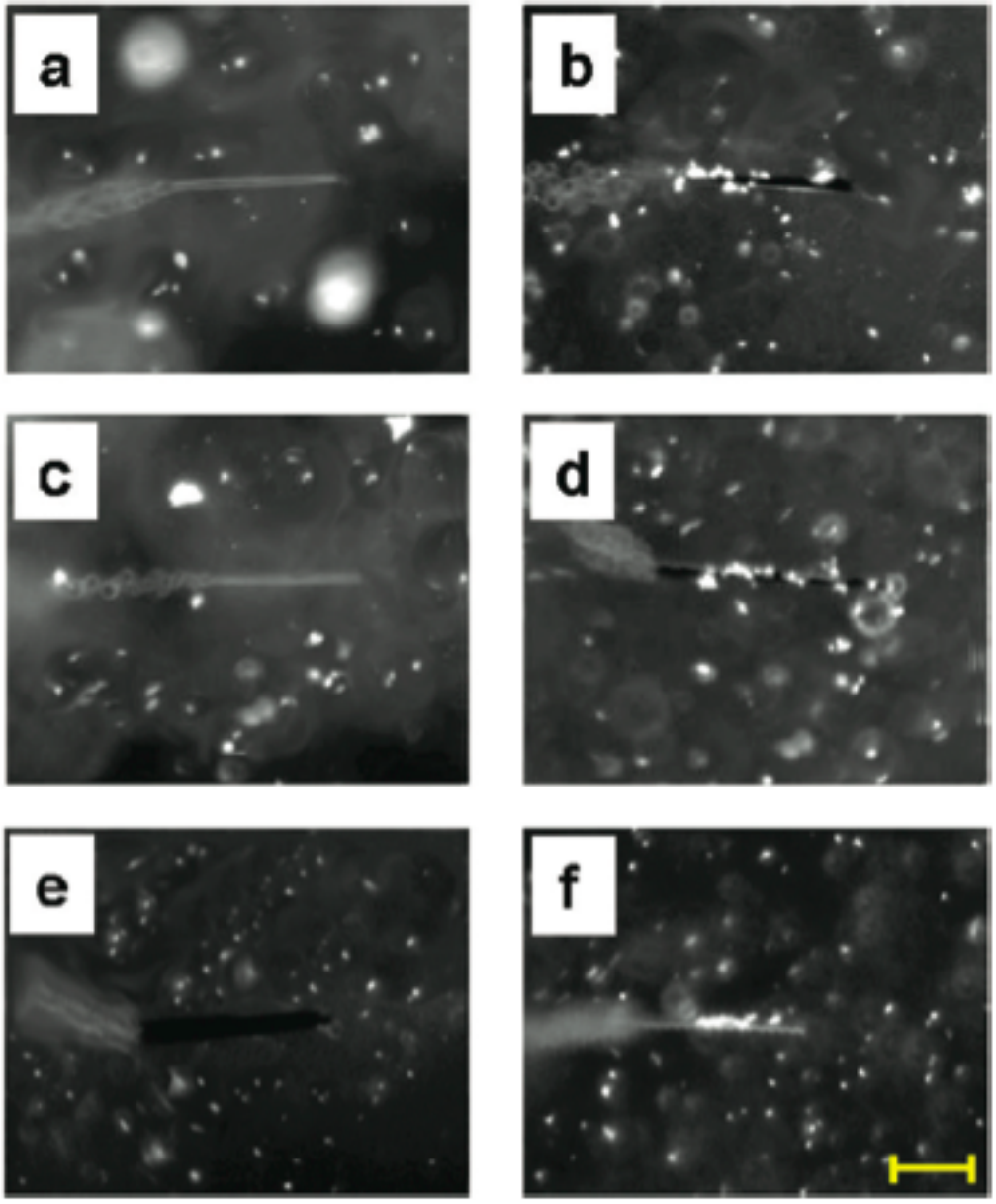

Figure 3.1.4 Micromotor-enabled nucleic acid isolation in biological samples. Time lapse images obtained after incubation of the SHCP+MCH-modified micromotors in solutions of 10% urine (a, b), 100% of serum (c, d), and crude bacterial lysate samples (e, f) containing 20 nM of target DNA (b, d), 200 nM of NC oligonucleotide (a, c) and rRNA corresponding to *K. pneumoniae* 1.8×10^5 CFUs/μL (e) and to *E. coli* 7.5×10^2 CFUs/μL (f). Images (a–d) were captured after 9 min of incubation and (e, f) after 6 min. Scale bar, 30 μm.

3.1.2.6 Isolation of *E. coli* 16S rRNA

The practical utility of this methodology was also illustrated with the isolation of *E. coli* 16S rRNA from raw lysate sample solutions. The specificity of the rRNA capture was tested using *Klebsiella pneumoniae* (*K. pneumoniae*) as a nontarget biological control. As can be seen in Figure 3.1.4f, the incubation in the *E. coli* 16S rRNA solution resulted in the attachment of numerous fluorescence particles to the modified microrockets; in contrast, no fluorescence (i.e., binding) is observed for a large (240-fold) excess of *K. pneumoniae* 16S rRNA (e). The images clearly demonstrates the efficient movement of the modified microrockets in these raw cell lysate samples containing membrane fragments and other cellular debris apart from the released nucleic acids. Overall, the data of Figure 3.1.4 indicates that the micromachine platform offers high specificity for the capture of the target nucleic acids even in the presence of complex biological samples.

3.1.2.7 Micromotor Based DNA Isolation in PDMS Channel

We have also demonstrated the ability of the modified-microrockets to transport the captured DNA across a microfabricated PDMS microchannel, from a "dirty" sample zone to a "clean" postprocessing zone, based on the general scheme shown in Figure 3.1.5 A. The optical images in Figure 3.1.5 B, along with the corresponding video (Supporting Video 3.1.1), depict the process as a modified microrocket captures the target DNA in a sample reservoir (a) and transports it across a 500 μm wide channel (b) to a clean downstream well (c). It should be noted that

such transportation across a 6 mm channel occurs within 80 s, i.e., at a speed of 75 μm/s, despite the opposite hydrostatic pressure gradient created to minimize diffusion of the fluorescence particles from the "dirty" to "clean" well. A similar microrocket speed within a microchannel was reported recently by Sanchez et al.[28] Absorption of the fuel by the PDMS matrix accounts for the reduced speed of the micromotor within the microchannel (relative to that observed in free solution).[29]

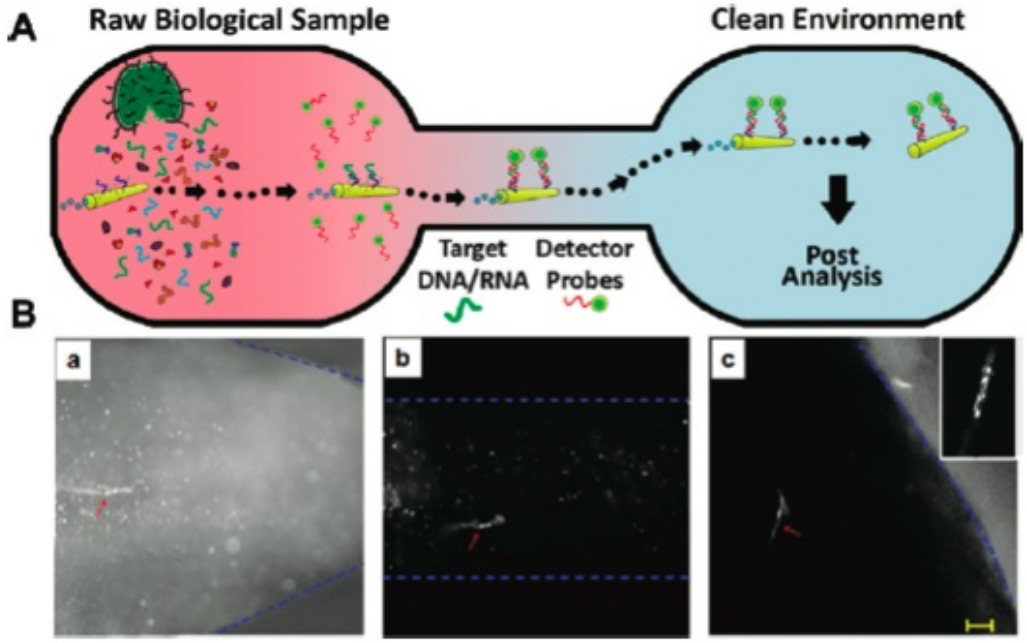

Figure 3.1.5 Isolation of the target nucleic acid in a PDMS channel using the modified microrockets. (A) Cartoon depicting the use of a modified microrocket to isolate and transport the captured target from a raw sample to a clean/separate location for downstream applications. (B) Optical microscopy images depicting the process as a SHCP+MCH-modified microrocket captures the target DNA in a sample reservoir (a) and transports it across a 6 mm long channel (b) to a clean well (c). Target DNA concentration 25 nM, 7 min moving in the "dirty" well before enter in the channel. Insert in panel c shows a 2X zoomed image taken 10 min after arriving to the clean well to facilitate a clear visualization of the fluorescent particles attached to the modified microrockets. Other conditions as described in Methods. Scale bar, 60 μm.

3.1.4 DNA Isolation Conclusions

The borders of the channel were accented using blue dash lines and the position of the microrocket is indicated with a red arrow for a clear visualization.

In conclusion, we have demonstrated that single-strand DNA-functionalized micromotors can act as selective transporters of complementary oligonucleotides (synthetic DNA or bacterial rRNA), allowing for their rapid isolation directly from raw biological samples without preparatory and washing steps. The increased localized convection produced by using these self-propelled modified microrockets resulted in more efficient target binding in microliter samples. This micromachine-based nucleic acid hybridization/isolation protocol could be readily incorporated into microchannel networks for creating microchip devices integrating the capture–transport–detection operation. Such microchips will rely on the active transport of multiple functionalized microshuttles to offer a single-step isolation of the target analytes. These microrockets could also be readily functionalized with other ligands for the isolation and assays of different target analytes. The new micromachine-based target isolation concept thus offers numerous potential applications in biomedical diagnostics, environmental monitoring, and forensic analysis.

3.2 Aptamer Based-Protein Isolation

3.2.1 Aptamer Based-Protein Introduction

Isolation, separation, and purification of different proteins and peptides are widely necessary in bioscience and biotechnology. For example, the selective isolation of proteins from biological samples is an important step in the diagnosis and treatment of various diseases. Yet, such protein isolation represents a challenge because of the complex composition of many biological samples. Affinity ligand techniques currently represent the most powerful selection and recovery tool available for downstream processing.[30,31] However, these techniques are time-consuming and not compatible with most biological samples that require pretreatment steps to eliminate suspended solids and fouling components.[32] Consequently, there are urgent needs to develop new efficient devices for sensitive, selective, and rapid isolation of target proteins from raw body fluids.

We introduce a novel and new nanomachine strategy for isolating target proteins from complex biological samples without preparatory and washing steps. Researchers have recently exploited the motion and power of natural and synthetic nano/microscale vehicles as prospective devices for transporting biomaterials and developing analytical tools that lead to new lab-on-a-chip formats.[11,32-34] There are several examples of using biological nanomotors to load, transport, and release cargos. Particular attention has been given to the pick-up and guided transport of a selected cargo by ATP-fueled kinesin/microtubule-based molecular shuttles.[13,33,35,36] However,

limitations of these biomotors, such as their short lifespan in synthetic environments, small power density, and confinement to microlithographic tracks, have motivated a transition to the engineering of both hybrid and fully synthetic nanomotors for diverse biomedical and bioanalytical applications.[6,9,11]

The section describes a synthetic microtransporter platform, functionalized with an aptamer, for the selective loading, directed transport, and controlled release of target proteins. Functionalized nanomotors present a new and powerful platform to effectively capture and isolate target biomolecules from biological samples.[22,37] Recent advances in self-propelled microtube engines have demonstrated their ability to propel through unprocessed biological fluids and to display large towing forces.[8,22,38] These inherent advantages of synthetic nanomotors make them extremely attractive for diverse biological applications. Functionalizing these microtube engines with oligonucleotide or antibody receptors was shown to be very useful for the selective capture and transport of target nucleic acids[37] and circulating tumor cells (CTCs),[13] respectively (next section). However, there are no reports of using artificial nanomotors for the selective isolation of target proteins or on the controlled release of captured biological targets

To accomplish the nanomotor-enabled selective protein isolation we functionalized the outer gold surface of microtube engines with aptamer receptors. Aptamers are artificially selected, functional oligonucleotides that represent attractive affinity reagents for protein isolation. They bind to molecular targets with high specificity and affinity and exhibit several advantages over antibody receptors.[39-41]

This new aptamer microtransporter concept is illustrated here by the highly selective thrombin isolation from complex biological fluids such as serum or plasma. Functionalization of the microengines was achieved by the self-assembly of a thiolated thrombin aptamer (SH–TBA) and mercaptohexanol (MCH) as "backfiller" onto its outer gold surface (Figure 3.2.1a). The controlled modification of the microtransporter surface offers remarkable discrimination against a large excess of nontarget proteins and, along with the specific aptamer recognition, leads to the selective isolation of the target protein from complex samples. Such use of artificial nanomachines as protein isolation platform represents a major advance toward protein analysis and an extremely novel and new bioanalytical concept.

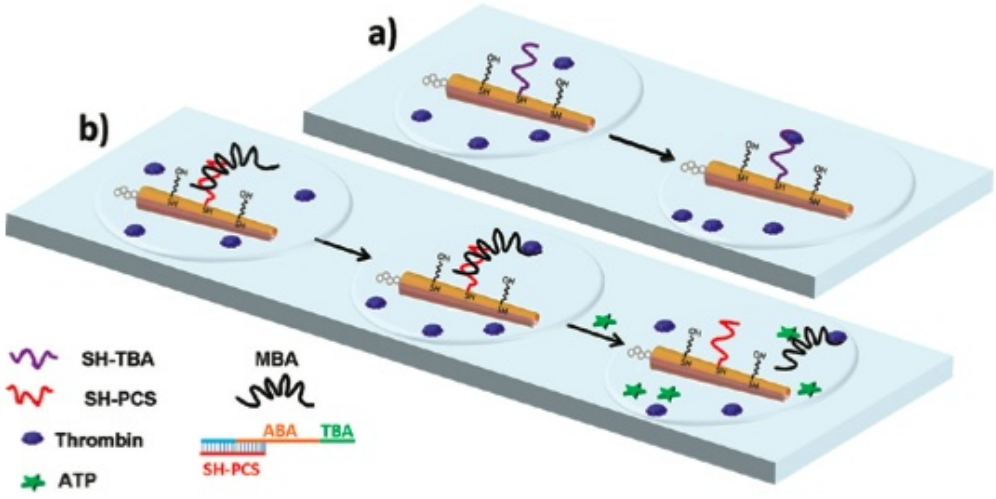

3.2.1 Cartoons depicting the selective pick-up, transport, and triggered release of target proteins based on aptamer-modified microengines. (a) Selective pick-up and transport of a target protein from a raw biological sample by a TBA-modified microtransporter. (b) Selective loading, transport, and release of the capture protein using a MBA-modified microtransporter. A detailed structure of the MBA is depicted at the left bottom of the image.

A second goal of the present work is to demonstrate for the first time the controlled (triggered) release of captured biological targets from a moving synthetic micromotor. Cargo unloading capabilities have been recently described using biological nanomotors but not with artificial microtransporters. In particular, the cargo unloading capability has been demonstrated using a kinesin biomotor by employing various triggers, such as light,[42] chemical,[43] biochemical,[12,13] or temperature[44] stimuli. To accomplish the challenging goal of protein binding and release from a synthetic nanomotor, we functionalized the surface of the microtube engines with a mixed binding aptamer (MBA), containing both ATP (ABA) and α-thrombin (TBA) binding aptamers. The MBA was prehybridized to a short thiolated partially complementary oligonucleotide strand that is bound to the microengine's surface (SH–PCS, see bottom left part of Figure 3.2.1). Such MBA was employed recently by Dong's group[45] for the reversible binding and release of captured proteins from electrochemical biosensors,[45,46] but not in connection to artificial nanomotors. As illustrated in Figure 3.2.1b, release of the captured thrombin from the moving MBA-modified microtransporter can be triggered by navigation in an ATP solution. Interaction with ATP induces a conformational change that releases the thrombin–MBA complex from the microengine surface, leaving on the surface only the SH–PCS.[46] The capture and release capabilities of the new aptamer-functionalized microshuttles make them extremely attractive for developing microchip devices that isolate protein biomarkers from unprocessed samples and perform the pick-up, guided transport, and controlled release of target biomaterials, in general.

3.2.2 Aptamer Based-Protein Experimental Methods

3.2.2.1 Reagents and Solutions

6-Mercaptohexanol (MCH) and sodium cholate (NaCh) were purchased from Sigma-Aldrich. Bovine serum albumin (BSA), lysozyme from chicken egg white, thrombin from human plasma, human IgG, human serum (from human male AB plasma), plasma from human, KCl, Tris–HCl, $MgCl_2$, $CaCl_2$, ammonium sulfate, and NaCl were purchased from Sigma-Aldrich. Hydrogen peroxide (30% w/w) was purchased from Fisher Scientific. Streptavidin-coated fluorescence microspheres (210 nm mean diameter CP01F/8905, 10 mg of microspheres/mL, 1% solids w/v) were purchased by Bangs Laboratories Inc. Reagents were used without any further purification.

The buffer solutions were the following: 50 mM Tris–HCl containing 140 mM NaCl, 1 mM $MgCl_2$, 5 mM KCl, and 1 mM $CaCl_2$, pH 7.4 (buffer 1), for TBA binding experiments; 25 mM Tris–HCl, 300 mM NaCl, pH 8.2 (buffer 2), for prehybridization of the SH–PCS with the MBA; 25 mM Tris–HCl, 100 mM NaCl, pH 8.2 (buffer 3), for the MBA binding experiments.

Solutions of 2% (w/v) NaCh, 0.05 μM biotinylated detection aptamer (B–DA), thrombin, and 0.02% (w/v) fluorescence particles were prepared daily in the corresponding buffer solution (buffer 1 or 3, depending on the aptamer used for the experiment). For isolation experiments from spiked biological samples (human serum

and plasma), the thrombin was prepared in the appropriate sample (previously diluted in the proper buffer if required).

All chemicals were analytical-grade reagents used as received and prepared by dilution in 18.2 MΩ cm Milli-Q deionized (DI) water when not otherwise specified.

3.2.2.2 Oligonucleotides used in this study.

All synthetic oligonucleotides (5' to 3') are used were purchased from Integrated DNA Technologies Inc. (San Diego, CA)

Thiolated capture probe, SH-TBA[a]: thiol–**GGTTGGTGTGGTTGG**

Detector probe, Biotin-DP[a]: biotin–TTTTTTTTTT**AGTCCGTGGTAGGGCAGGTT GGGGTGACT**

Thiolated Partly Complementary DNA Strand (SH–PCS): thiol-TACAGACCTTCC

Mixed thrombin–ATP aptamer (MBA)[b:] **GGTTGGTGTGGTTGG** ACCTGGGGGAGTATTGCGGAGGAAGGTCTGTA

a = The SH–TBA and B–DA (15- and 29-mer in bold, respectively) were reported to recognize different sites of thrombin with different affinities. The 15-mer aptamer binds the fibrinogen recognition exosite of thrombin (K_d = 26 nM), whereas the 29-mer aptamer was known to bind to the heparin binding exosite (K_d = 0.5 nM).[47]

b = The unimolecular MBA contained a small-molecule ATP binding aptamer (ABA) and also a protein α-thrombin binding aptamer (TBA) see left bottom in Figure 3.2.1).

In boldface are the specific sequences for the thrombin recognition sites, and underlined is the sequence recognition for the ATP.[45,46]

3.2.2.3 Microtransporters Fabrication

The Ti/Ni/Au/Pt microtubes engines are commonly prepared by modifying the previously reported top-down photolithographic protocols,[14,15] angled e-beam evaporation, and the stress-assisted rolling of functional nanomembranes on polymers into conical microtubes. Briefly, a positive photoresist (Microposit S1827, Microchem, Newton, MA) which serves as a sacrificial layer, was spin-coated on a silicon wafer at 3000 rpm for 60 s. The coated wafer was baked at 115 °C for 60 s and exposed to UV light with an MA6 mask aligner for 35 s to create predefined patterns. Exposed patterns were developed using a MF-321 developer for 90 s and thoroughly washed with DI water. Metallic layers of Ti, 10 nm, Ni, 15 nm, Au, 5 nm, and Pt, 10 nm, were deposited sequentially using an e-beam evaporator under high-vacuum conditions ($<10^{-4}$ Pa). The e-beam substrate holder was tilted to 48° in order to asymmetrically deposit metals on the patterns. Upon selective removal of the exposed photoresist layer using MF-1165 (Rohm and Haas, Marlborough, MA), the prestressed metallic layers self-assemble into microtubes. The microtransporters were washed and stored in isopropyl alcohol before undergoing critical-point drying to maintain structural integrity. The resulting microtube engines have an inner (catalytic) Pt surface, a diameter opening of 2–10 μm, and are typically 50–100 μm in length.[8,15] The oxygen-bubble recoil propulsion mechanism of these tubular microengines is associated with the decomposition of peroxide fuel on the inner catalytic Pt surface. The conical shape

of the microengine assists unidirectional bubble expansion, and small amounts of surfactant are used to sustain the bubble development and promote their release.[22,38] The incorporation of the intermediate ferromagnetic Ni layer during their fabrication allows for a precise magnetic guidance of their movement. A thin (~60 nm) gold layer was sputtered onto the rolled-up microtubes to facilitate the surface functionalization with the mixed self-assembly monolayer (SAM) described below.

3.2.2.4 Prehybridization of the SH–PCS with the MBA

A mixture of 1.9 μM SH–PCS and 2.2 μM MBA (in buffer 2) was heated and kept at 90 °C for 5 min. The solution was then slowly cooled up to room temperature (around 30 min.[46]

3.2.2.5 Microtransporters Modification

The external gold surface of the microtransporters was modified by an overnight immersion in a 10 μM SH–TBA (in buffer 1) or the SH–PCS/MBA prehybridized solution prepared as specified in the previous section. After washing with the appropriate buffer, the modified microtransporters were post-treated with a 0.1 mM MCH solution (also in the corresponding buffer) for 10 min to obtain the corresponding mixed SAMs. Finally, they were washed for 60 s with buffer, entirely detached from substrates by carefully scratching with a micropipette tip, and placed in the corresponding binding buffer. All incubation steps were carried out at room temperature.

3.2.2.6 Thrombin Isolation and Detection

The thrombin isolation and detection protocol involved a sandwich-type assay format in which the thrombin is captured between the microtransporter surface-chemisorbed capture aptamer (TBA or MBA) and the B–DA. Once the sandwich is formed the labeling of the B–DA with the streptavidin–fluorescence particle tags confirms the presence of thrombin attached to the aptamer-modified microtransporters.

For isolation of thrombin, a mixture of the 3 μL of aptamer-modified microtransporters suspension, 2 μL of 2% (w/v) NaCh, 1.5 μL of 30% (w/w) H_2O_2, and 3 μL of thrombin solutions (in the appropriate binding buffer or in the biological sample under study) was dropped onto a freshly cleaned glass slide. The modified microtransporters were allowed to move 10 min in this solution to capture the protein, after which 3 μL of 0.05 μM B–DA solution was added, and the modified microtransporters were allowed to move in this solution for additional 10 min. In the last step, a 3 μL of 0.02% (w/v) fluorescence particles suspension was added and the microtransporters carrying the affinity complex (SH–TBA–thrombin–B–DA) were allowed to move randomly in the above solution during the desired time. It is important to note that the initial concentrations of the assay reagents (thrombin, ATP, B–DA, fluorescent particles, and samples) provided in the text are diluted by the addition of other reagents. At the moment of video acquisition, the modified microtransporters were magnetically guided to localize them in the observation window. Videos were captured using CoolSNAP HQ^2 camera, 20× objective (unless mentioned otherwise) and acquired at a frame rate of 10 frames/s using the

Metamorph 7.1 software (Molecular Devices, Sunnyvale, CA). A Nikon Eclipse 80i upright microscope with B2-A FITC filter was used to capture fluorescence images and videos. An estimation of the captured affinity complex-tagged particles coverage on the microtransporters was obtained by analyzing the corresponding time-lapse images using the ImageJ software. It is important to point out that the 100% coverage corresponds to the total of the gold layer surface sputtered onto the rolled-up microtubes and not the total of their surface.

For the selectivity data, control experiments were carried using 3 μL of the corresponding binding buffers (or samples under study) without target protein, or with solutions of nontarget proteins (BSA, human IgG, and lysozyme) alone or mixed with the target protein, prepared in the corresponding binding buffer. All procedures were carried out at room temperature.

3.2.2.7 Isolation of Thrombin from Human Serum Samples

Fibrinogen was precipitated from plasma (but not from serum) before the addition of thrombin in the preparation of spiked samples. An amount of 250 μL of plasma was treated with 1250 μL of 2 M ammonium sulfate and 1000 μL of 0.1 M NaCl aqueous solutions. The solution was mixed for 3–4 min and then centrifuged at 12 000 rpm during 4 min.[47] The nondesalted supernatant was spiked with the desired thrombin concentration. To test the performance of the aptamer-based microengines in these complex matrixes 100 nM thrombin standard solutions were added to the untreated serum or pretreated plasma samples, respectively.

3.2.2.8 Unloading Experiments

Aliquots of 3 μL of the MBA-modified microtransporters suspension, 2 μL of 2% (w/v) NaCh, 1.5 μL of 30% (w/w) H_2O_2, and 3 μL of 200 nM thrombin solutions (in the appropriate binding buffer) were dropped on a freshly cleaned glass slide. The modified microtransporters were allowed to move 10 min in this solution to capture the protein, after which two different protocols were tested. On one hand, 3 μL of B–DA and 3 μL of fluorescence particles were allowed to react with the previous mixture during 10 min each, after which 3 μL of 0.01 M ATP solution was added, and surface coverage was checked after 20 min. Alternately, 3 μL of 0.01 M ATP solution was first added to the solution, and the microtransporters were allowed to navigate during 20 min to release the bound protein. After that, the thrombin that remains attached to the microtransporters was labeled using the previously described B–DA and the fluorescence particles sequential incubation steps, and the surface coverage was then estimated.

3.2.3 Aptamer Based-Protein Results and Discussion

3.2.3.1 Concept

Microengine transporters, fabricated using a custom photolithography process,[14,15] were sputtered with gold and functionalized with a binary SAM that comprises a capture aptamer along with the common MCH backfiller. The ordered and compact binary SAM coating ensures favorable accessibility of the aptamer receptor toward the target protein while minimizing nonspecific adsorptions.[26] Depending on the specific protocol used here (loading/transport vs loading/transport/unloading of target protein), either microtransporters functionalized with SH–TBA or the MBA (prehybridized with the SH–PCS) aptamers were used (see Figure 3.2.1 and the Methods for details). Approximately 4.7×10^7 immobilized TBA or SH–PCS molecules can be estimated on the modified microtransporters by considering the maximum surface coverage for a thiolated DNA monolayer on gold surfaces[18] and the microtransporter gold surface area ($\sim 4.71 \times 10^{-6}$ cm^2).

The aptamer-functionalized microtransporters can readily move around within a biological sample (containing fuel) and can recognize and interact with the target thrombin protein (Figure 3.2.1a). We relied on an instant optical visualization of the target binding event involving B–DA that binds to subsequently added streptavidin-coated fluorescent nanoparticle tags, forming a "TBA–thrombin–B–DA" sandwich on the moving microshuttles. Experiments reveal that the incubation of the modified microengines in solutions containing thrombin, the B–DA, and the fluorescent

particles has to occur separately in a stepwise fashion (c vs a and b), to minimize hindrance of the thrombin recognition event.

3.2.3.2 Selectivity of the Microtransporters to the Target Protein

Specific binding is a key requirement for the new aptamer-based nanomotor isolation platform. To evaluate the binding specificity of the aptamer-modified microtransporters toward the target thrombin protein, various nontarget proteins were used (at 50-fold excess) as negative controls. The optical microscope images of Figure 3.2.2 and illustrate the high specificity of the dynamic aptamer–thrombin interaction using different protein solutions: (Figure 3.2.2a) 20 nM thrombin and 1000 nM (Figure 3.2.2b) BSA, (Figure 3.2.2c) IgG, and (Figure 3.2.2d) lysozyme. A substantial coverage of the microengine surface is observed in the target protein solution (Figure 3.2.2a). In contrast, only negligible binding is indicated for the large excess of the nontarget BSA, IgG, and lysozyme (Figure 3.2.2b–d). Microrockets move at an efficient propulsion of the aptamer-modified microengine (at a high speed of 125 μm/s). Capture of the thrombin target also has a negligible effect upon the propulsion efficiency.

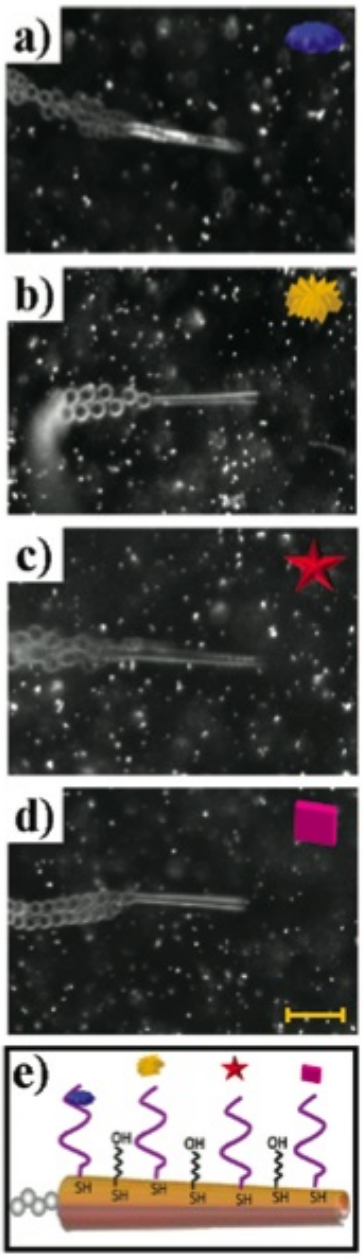

Figure 3.2.2 Selective isolation of the target protein: (a) thrombin (20 nM) vs large (50-fold) excess of nonspecific proteins (1000 nM) (b) BSA, (c) human IgG, and (d) lysozyme. Images a–d were obtained from videos. The representative modified microtransporters were navigated for 10 min in solutions containing either the protein under study or the respective nontargeting proteins. (e) Scheme depicting the observed selectivity results where only the target protein is captured by the TBA-modified microtransporters. Fuel conditions: 3% (w/w) H_2O_2, 0.3% (w/v) NaCh. Scale bar, 30 μm.

To further demonstrate the efficient isolation of the target protein, the modified microtransporters were tested with different concentrations of thrombin (0–500 nM) mixed with a solution containing an excess of all three nontarget proteins (1000 nM each). Figure 3.2.3 (10 min* labeled bars) illustrates that the surface coverages obtained in the presence of these nontargeting proteins were coherent with those observed for the analyte alone (at the same level) over the entire thrombin concentration range examined. These results indicate that the specificity and kinetics of the thrombin binding are not affected by the presence of these coexisting proteins. Another series of experiments, which compared the binding of 100 nM thrombin in the absence or presence of increasing concentrations of the three nontargeting proteins (at 10-, 100-, and 500-fold excess), confirmed the possibility to isolate the target protein. High fluorescent coverage of 78% was observed even in the presence of a huge (500-fold) excess of BSA, human IgG, and lysozyme compared to 88% coverage without these nontargeting proteins. This difference in surface coverage can be likely attributed to the increased solution viscosity and lower probability of target protein interaction when the motor is traveling in the excess nontarget protein solution.

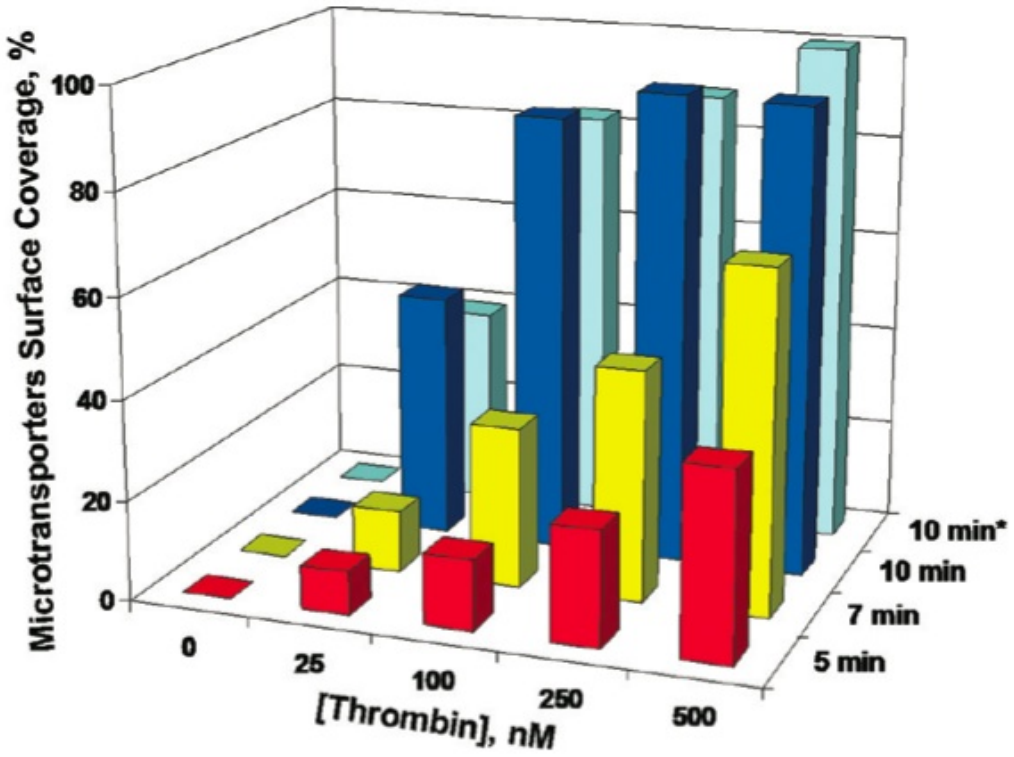

Figure 3.2.3 Kinetics of target protein binding. Dependence of the coverage of fluorescent particles on the TBA-modified microtransporters upon the navigation time (5, 7, and 10 min) in solutions containing different concentrations of thrombin alone or mixed with 1000 nM of three nontargeting proteins: BSA, human IgG, and lysozyme (10 min*). Other conditions are as in Figure 3.2.2. Each condition corresponds to an average of two batches of five microtransporters.

The high selectivity, illustrated in Figure 3.2.2 in these mixture experiments, is attributed not only to the high affinity of the capture aptamer toward the target thrombin but also to the effective minimization of nonspecific binding. The latter reflects the highly dense hydrophilic SAM surface coating and the dynamic microengine movement (along with its induced fluid convection) that facilitates the removal of nonspecifically bound particles. These data indicate that the "on-the-fly" capture and transport of target proteins binding can substitute the washing steps

intrinsic to sandwich protein bioassays and that the presence of the peroxide fuel and NaCh surfactant does not affect the aptamer–thrombin interaction.

3.2.3.3 Reproducibility of the Assay and Kinetic Study

A highly reproducible isolation protocol was created by the systematic optimization of all the experimental conditions involved in the recognition and labeling steps. They were conducted to maximize the binding efficiency while reducing the overall assay time and minimize undesirable nonspecific adsorptions and particle aggregation (not shown). The selected optimized parameters are summarized as follows (10 μM [SH–TBA], 0.1 mM [MCH], 10 min precoating time in MCH, 0.05 μM [B–DA], 10 min incubation time in each step, and 0.02% (w/v) [fluorescence particles]). These are initial concentrations, not considering the dilution effect occurring after mixing with the other reagents required by the bioassay. The experimental reproducibility was investigated using five different modified microtransporters batches following the identical processing steps. A relative standard deviation (RSD) of 6.7% was obtained among the corresponding estimated coverage values after 10 min of incubation in a 100 nM thrombin solution. This indicates small differences in the protein capture efficiency due to the use of different batches of modified transporters. It should be noted also that the speed of the microtransporters remained relatively constant (120 ± 15 μm/s, n = 40) after the prolonged time (>30 min) required for the whole sequential steps of the bioassay (see Methods for details).

Kinetic properties of the thrombin binding on the TBA-modified microtransporters were evaluated. Figure 3.2.3 depicts the influence of the incubation

time and the thrombin concentration upon the isolation efficiency (estimated from the fluorescent coverage). It is clear from these isolation trends that 5 and 7 min incubation times lead to similar concentration-dependent profiles, where the surface coverage increases with the protein concentration over the 25–500 nM range examined. In contrast, when using longer incubation times (≥10 min), the coverage rapidly reaches the maximum value for thrombin concentrations greater than 100 nM (i.e., surface saturation). Such profiles indicate that short incubation times can offer a direct quantitative protein detection down to the low-nanomolar level. The lowest detectable level (after 10 min of incubation) was 5 nM of thrombin, was demonstrated. The dissociation constant, K_d, of the thrombin–TBA complex was estimated by the nonlinear regression analysis method from the saturation profile obtained after 10 min of incubation in the thrombin solution. This was accomplished by plotting the inverse of the surface coverage versus the inverse of the thrombin concentration at saturation conditions. Such plot yields a straight line with K_d being the product of the slope and the intercept.[48,49] The low estimated K_d value of 5.5 nM (vs 5–300 nM range reported),[49,50] indicates high affinity of the microtransporter-immobilized TBA for the target. While aptamer binding often requires long incubation times (due to their slower conformational changes)[51] the microengine-induced localized convection appears to accelerate the binding step. Short incubation periods (<10 min) are thus sufficient for effective isolation from nanomolar thrombin solutions.

3.2.3.4 Isolation from Complex Biological Matrixes

The practical utility of the new microengine approach was illustrated by the ability of the aptamer-modified microtransporters to recognize the target protein in a complex media such as human serum and plasma samples. The different composition of these complex biological fluids is evidenced from the video, with the plasma sample leading to a higher bubble size and lower speed due to the presence of coagulation factors and its high viscosity.[52] The efficient propulsion of the modified microtransporters in these complex biological samples (with speeds of 90 and 70 μm/s, respectively) allows for their prolonged movement and direct isolation of thrombin without tedious sample processing steps. The ability of microengines to efficiently capture the target protein from biological samples has been evaluated using 25% diluted human serum (raw or spiked with thrombin) and 10% plasma samples spiked with thrombin (with or without a standardized pretreatment for quantitative fibrinogen precipitation). The aptamer-modified microtransporters displays a strong fluorescence in both thrombin-spiked biological samples, reflecting the effective binding of the target protein. In contrast, no fluorescence (binding) is observed in the unspiked serum sample and in plasma samples containing excess thrombin before fibrinogen selective precipitation. Such fibrinogen precipitation is essential for avoiding clotting of plasma samples after thrombin addition.[47,53] Unlike serum, which does not contain coagulation factors, plasma contains all proteins involved in the coagulation cascade, including fibrinogen that is being converted by thrombin to insoluble fibrin that forms the fibrin gel.[47] Lower capture efficiencies of 56.2% and 46% have been estimated for

the binding in serum and plasma, respectively, compared to 88% observed in the buffer medium. This reduced efficiency reflects differences in the solution's ionic strength and viscosity, which can hinder the aptamer–protein interactions[54] and lower the microengine's speed. In spite of the matrix effect, the efficient propulsion and binding ability of the functionalized microtransporters allows for a very effective capture from these complex physiological samples containing nanomolar thrombin levels. Such efficient binding is not compromised by the intrinsic presence of a large excess of nontarget proteins in the assayed biological samples (e.g., 33–127 μM human IgG and 524–779 μM BSA), which further supports the high selectivity of the new nanomotor-based protein isolation approach. Overall, these data confirm the feasibility of the new aptamer-based microtransporters to propel effectively and detect selectively trace levels of proteins in human serum and plasma samples.

3.2.3.5 ATP-Assisted Release of the Captured Thrombin

To facilitate the release of the captured thrombin the TBA receptor was replaced with a MBA receptor. According to its structural design (see bottom left part of Figure 3.2.1), when only thrombin is present in the solution, the MBA-modified microtransporters would capture the thrombin and transport it toward the desired site. However, when ATP is present, it can interact with the ATP-binding aptamer portion (ABA), overlapped by the section of the MBA hybridized to SH–PCS, and draws the thrombin–MBA complex away from the modified microtransporter surface. This leaves only the SH–PCS attached to the microtransporters resulting in the full release of the thrombin–aptamer complex (Figure 3.2.1b).

To accomplish the triggered release of the captured thrombin, we thus incubated the microtransporters (containing the MBA–thrombin complex) in an ATP solution for a fixed time (last step in Figure 3.2.1b) before labeling the attached thrombin with the B–DA and the fluorescence particles in the usual way. Figure 3.2.4 illustrates images (from Supporting Video 3.2) of the MBA-modified microtransporters after target binding (indicated by the presence of bound fluorescent particles) and incubation in a buffer solution, in the presence and in the absence of ATP trigger molecule. Incubation in the ATP solution resulted in a very small fluorescence coverage of only 9% on average compared to the 74% coverage observed in a control experiment without ATP. These results demonstrate the efficient release of the thrombin–MBA complex after 20 min of movement in the 0.01 M ATP solution. Such release is significantly (4-fold) shorter than that reported recently by Dong's group[45,46] for the same MBA using conventional electrochemical biosensors. The faster release attributed in part to the microengine-induced fluid convection. Similar to previously reported aptamer and kinesins schemes,[43] a real-time release of the target cannot be observed due to the slow kinetic of the MBA–ATP interaction[45,46] and the need for a post-release labeling step. Our results demonstrated that the labeling of the captured thrombin (with the B–DA and fluorescence spheres) hinders the ATP interaction with the MBA aptamer thereby requiring a postrelease labeling approach. With the use of this approach the drop-off of the protein cargo into the solution is clearly indicated when comparing the fluorescence coverage observed after navigation in a buffer solution, with and without the ATP trigger molecule.

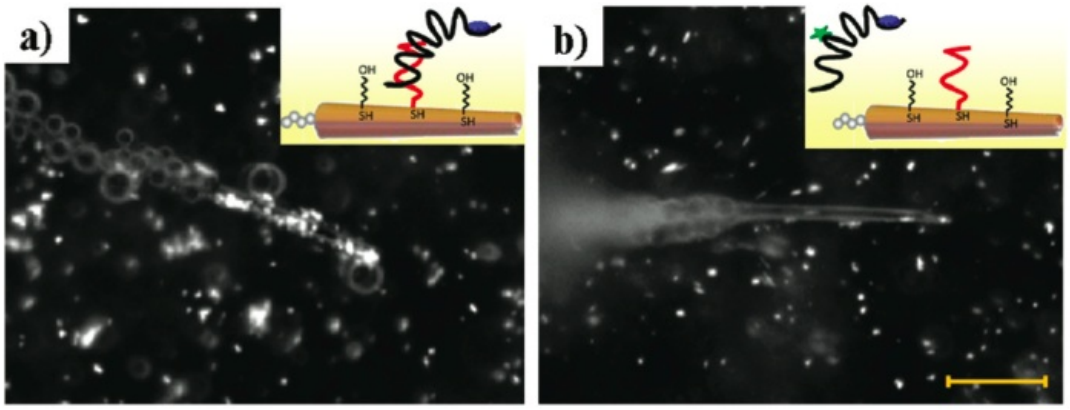

Figure 3.2.4 ATP-induced unloading of the captured thrombin from the modified microtransporters. Images were taken from Video 3.2, demonstrating the release of the target protein after 20 min of incubation of the thrombin–MBA-modified microtransporters in the absence (a) or in the presence (b) of 0.01 M ATP trigger. Other experimental conditions are as Figure 3.2.2. Scale bar, 30 μm.

As expected, no apparent loss in the fluorescence coverage was observed when conducting similar unloading experiments using microtransporters modified with the TBA (lacking the ATP binding site). These results (not shown) confirmed that the unloading of thrombin was caused by the selective ATP interaction with the ABA region of the MBA. It should be pointed out that a high (millimolar) concentration of trigger molecule is required for the efficient thrombin unloading over the time scale of the experiment. This ensures that the low (nanomolar) physiological level of ATP in common body fluids[55] will not lead to an unintentional release of the thrombin, as desired for practical applications of the new approach. Microtransporters utilizing this ATP-triggered aptamer release scheme also have the potential to be reused by rehybridizing the remaining SH–PCS (last step in Figure 3.2.1b) with new MBA strands. This reusable attribute is advantageous over traditional heating–rehybridizing regeneration methods that can destroy Au–S bonds,[12] thus providing the possibility to

reuse the same microtransporter in a new isolation experiment. The ATP-triggered specific target unloading approach has several potential applications including controlled target release, target concentration, and ATP detection. Release of the captured thrombin could be exploited for devising highly miniaturized chip systems integrating the capture, transport, and unloading operations at well-defined positions without an external power or control, thereby providing considerable promise for the separation of proteins and detection of protein biomarkers.

3.2.4 Conclusions

We have demonstrated a new nanomachine-based strategy for isolating target proteins from complex biological fluids. The aptamer-functionalized microengines offer attractive capabilities for autonomous loading, directional transport, and assisted unloading of target proteins. The fluid convection induced by the rapid movement of the modified microtransporters enhanced the aptamer–target binding efficiency, which resulted in a rapid and highly selective thrombin isolation with an effective discrimination against a large excess of nontarget proteins. The microtransporter's ability to isolate targets from raw biological samples, while avoiding preparatory and washing steps, is significant compared to current techniques especially considering the assay's speed and specificity. The simple navigation of these guided multifunctional microtransporters in an ATP solution led to the unloading of the bound thrombin molecules. The multiple inherent capabilities of receptor-functionalized microengines may help to devise miniaturized on-chip systems, by integrating the capture, transport,

and release operations within spatially separated loading and unloading zones, without any external power.

The new motion-driven protein isolation platform represents a fundamentally new approach in bioanalytical chemistry based on active transport and offers an attractive alternative for current protein isolation protocols. Although this new concept has been illustrated for aptamer-based thrombin isolation, it can be further extended for different targets or multiplexed detection using different bioreceptors. Additionally, mixed aptamers-modified microtransporters can be used to transport larger protein-functionalized cargos, such as drug-loaded polymeric particles, and release them using an appropriate trigger (as demonstrated here) for targeted drug delivery systems,[56] or they can be utilized for creating an on-chip molecular-sorter microsystem. These advantages pave the way for a realm of practical applications that utilize the microtransporter's unique, self-controlled movement for protein monitoring and disease diagnosis.

3.3 CTC Isolation

3.3.1 CTC Isolation Introduction

Circulating tumor cells (CTCs) are the primary entities responsible for spawning cancer metastasis. Detection of CTCs provides an indicator for the clinical diagnosis and prognosis of various types of cancers. Several approaches, based primarily on flowing the sample through antibody-coated magnetic beads[57] or microchip[58,59] surfaces, have been described for isolating and counting CTCs. However, these approaches require extensive sample preparation and/or complex surface microstructures to detect the extremely low abundance of CTCs in blood.[59,60] In this study we describe an immuno-micromachine-based approach for in vitro isolation of cancer cells that holds promise for direct CTC detection without sample preprocessing.

Recent progress in the field of man-made nanomachines,[5,6,61] particularly major advances in the power, efficiency, motion control, and versatility of artificial nanomotors,[15,62-64] have opened the door to new and important biomedical applications ranging from drug delivery[9] to biosensing.[11] Autonomously moving synthetic nanomotors have recently been employed for the pickup and transport of diverse payloads, mostly through magnetic or electrostatic interactions.[25,29,65,66] Extending the scope of chemically powered nanomotors to physiological conditions is a key challenge since such nanomotors are commonly incompatible with the high ionic strength environment of biological fluids. Catalytic rolled-up microtube rockets,

propelled by the recoiling force of accumulated gas bubbles,[14,15,21,23,25] are particularly attractive for isolating and transporting cancer cells for downstream analysis as they possess the necessary towing force to carry large mammalian cells. Here it is demonstrated that these microrockets overcome previous constraints to locomotion in biological fluids and are readily functionalized with an antibody specific for antigenic surface proteins expressed on cancer cells, such as anti-carcinoembryonic antigen (anti-CEA) monoclonal antibody (mAb).[67] CEA is used as a targeting antigen because it is one of the most common antigens among cancer cells, being overexpressed in approximately 95 % of colorectal, gastric, and pancreatic cancers.[68] Figure 3.3.1 conceptually illustrates the pickup and transport of cancer cells by microrockets. The conjugation of the anti-CEA mAb to the outer gold surface of the microrockets is accomplished through carboxy-terminated groups from a binary self-assembled monolayer (SAM) using *N*′-(3-dimethylaminopropyl)-*N*-ethylcarbodiimide)/*N*-hydroxysuccinimide (EDC/NHS) for amidation (see the inset in Figure 3.3.1 and the Experimental Section for details).

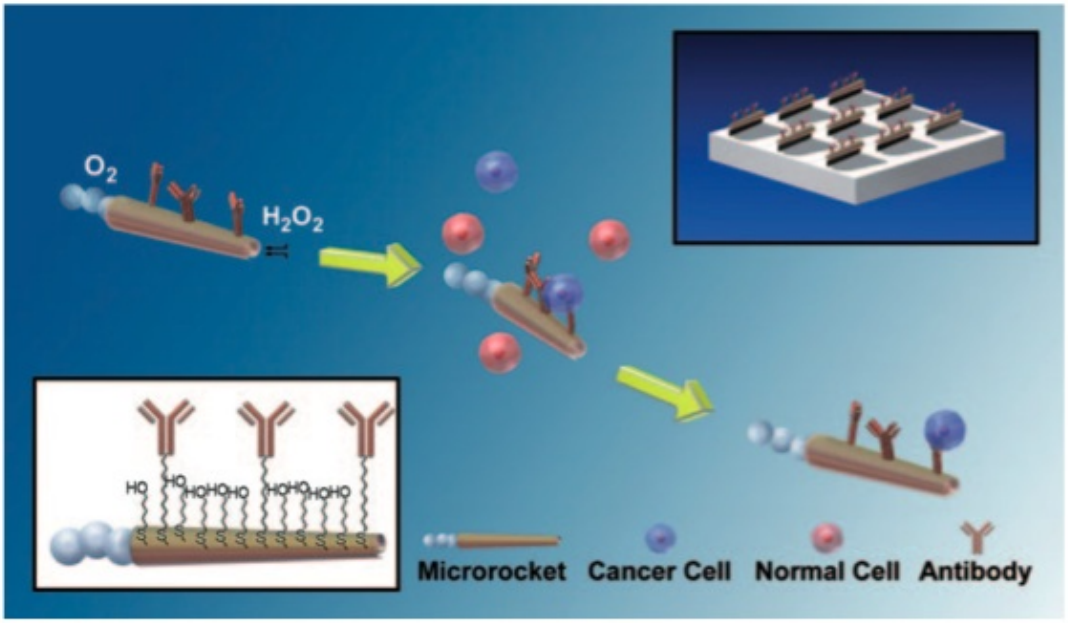

Figure 3.3.1 Microrockets for capture and isolation of cancer cells. Upon encountering the cells, the anti-CEA mAb-modified microrockets recognize the CEA surface antigens on the target cancer cells, allowing their selective pickup and transport. The top-right and bottom-left insets illustrate the preparation of the Ab-modified microrockets and their functionalization, respectively.

3.3.2 CTC Isolation Experimental Methods

3.3.2.1 Reagents and solutions

6-Mercaptohexanol (MCH), 11-mercaptoundecanoic acid (MUA), *N*-hydroxysuccinimide (NHS), 1-(3- dimethylaminopropyl)-*N*'-ethylcarbodiimide hydrochloride (EDC) and sodium cholate were purchased from Aldrich. Mouse anti-carcinoembryonic antigen (CEA), Clone Col-1 (18-0057) (anti-CEA), and Sybr Green II nucleus staining dye, and 4',6-diamidino-2-phenylindole (DAPI, nucleus staining) were purchased from Invitrogen (Carlsbad, CA). Bovine serum albumin (BSA), human serum (from human male AB plasma), KCl, Na2HPO4, K2HPO4.3H2O and NaCl were purchased from Sigma. Reagents were used without any further

purification. Experiments were carried out at room temperature. For tissue culture, 10% fetal bovine serum was acquired from Hyclone (Logan, UT), sodium bicarbonate was obtained from Cellgro (Herndon, VA), RPMI culture medium, penicillin/streptomycin, sodium pyruvate, L-glutamine, and MEM non-essential amino acids were purchased from Invitrogen (Carlsbad, CA), and EDTA powders were bought from Fisher Scientific. Other solutions employed were: Phosphate buffered saline 1␣PBS buffer (containing 137 mM NaCl, 2.7 mM KCl, 8.1 mM Na2HPO4 and 1.4 mM KH2PO4, pH 7.4) and 1% BSA solution in the same PBS buffer, each prepared in deionized water. All chemicals used were of analytical-grade reagents, and deionized water was obtained from a Millipore Milli-Q purification system (18.2 MΩ cm).

3.3.2.2 Microrockets fabrication

The Ti/Fe/Au/Pt microtube rockets were prepared by modifying previously reported lithographic protocols.[14] Briefly, a positive photoresist (Microposit S1827, Microchem, Newton, MA) which serves as a sacrificial layer, was spin-coated on a silicon wafer at 3000 rpm for 60 seconds. The coated-wafer was baked at 115 °C for 60 seconds and exposed to UV light with an MA6 mask aligner for 35 seconds to create pre-defined patterns. Exposed patterns were developed using a MF-321 developer for 90 seconds and thoroughly washed with DI water. Metallic layers of Ti: 10 nm, Fe: 15 nm, Au: 5 nm and Pt: 10 nm were deposited sequentially using an e-beam evaporator under high vacuum conditions (<10-4 Pa). The e- beam substrate holder was tilted to 50° in order to asymmetrically deposit metals on the patterns.

Upon selective removal of the exposed photoresist layer using MF-1165 (Rohm & Haas, Marlborough, MA), the prestressed metallic layers self-assemble into microtubes. The microrockets were washed and stored in isopropanol before undergoing critical-point drying to maintain structural integrity. A thin (~60 nm) gold layer was sputtered onto the rolled-up microtubes to facilitate surface functionalization with the antibody receptor through the assembly of alkanethiols.

3.3.2.3 Microrockets modification

The external gold surface of the microrockets was modified by an overnight immersion in a binary mixture of 2.5 mM of MUA and 7.5 mM of MCH in absolute ethanol. After washing with ultrapure water, the microrockets modified with the resulting mixed monolayer were treated with a solution of NHS (20 mM) and EDC (10 mM) in ultrapure water for 30 min, followed by an 1 h immersion in a solution of 1XPBS buffer (pH 7.4) containing 2 mg/ml of anti-CEA mAb. The remaining reactive groups of the activated monolayer were blocked with 1 M ethanolamine (pH 8.5) for 30 min. The microrockets were subsequently immersed in a 1 % (w/v) solution of BSA in 1XPBS buffer (pH 7.4) for 1 h. Finally, the modified microrockets were washed for 60 s with ultrapure water and resuspended in 1XPBS buffer (pH 7.4). All incubation steps were carried out at room temperature followed by immersion in ultrapure water for 1 min.

‘‘Control’ microrockets (without the mAb) were prepared using the same protocol (with the SAM assembly, activation and blocking steps) but omitting the

addition of the anti-CEA mAb and carrying out the corresponding incubation in buffer (without mAb). It is important to note that the anti-CEA mAb- modified microrockets can be used to capture and transport CEA+ cells if they are stored (up to 2 weeks) in 1XPBS buffer (pH 7.4) at 4^{o}C. Also worth noting is that the Fe layer of the microrocket is very susceptible to the presence of HCl salt in EDC during activation of the —COOH of the monolayer which can render them non-magnetic. In order to maintain the magnetic property of the microrockets, at least 3 times more Fe layer is required. This allows for effective propulsion and proper navigation of modified microrockets even in complex biological media.

3.3.2.4 Preparation of Suspended Cancer Cells

The human pancreatic CEA-positive BxPC-3 (CEA+ cells) and the CEA-negative XPA-3 (CEA- cells) cell lines were maintained in RPMI-1640 medium supplemented with 10% fetal calf albumin, penicillin/streptomycin, L-glutamine, MEM nonessential amino acids, sodium bicarbonate, and sodium pyruvate. Both cell lines were cultured at 37˚C with 5% CO2. To prepare the cells in suspension, each cell line was detached following 20 min incubation in PBS (without Ca/Mg) containing 15 mM of EDTA. The cells were then pelleted and resuspended in PBS with Ca/Mg. The viability of the cells was confirmed using a trypan blue dye exclusion assay. Prior to their fluorescent imaging, the BxPC-3 and XPA-3 cells were nuclear stained in 1X Sybr Green II and DAPI solution, respectively.

3.3.2.5 Identification and Isolation of Cancer Cells

Microrockets functionalized with the anti-CEA mAb were isolated from the substrate surface and suspended in 1␣PBS buffer (pH 7.4). A mixture of microrockets (1 μl) and sodium cholate (1%(w/v), 3 μl) was added to a freshly cleaned glass slide. To this, 5 μl of suspended cancer cells and 3 μl of H2O2 were added (final peroxide concentration, 7.5%(w/v)). Microrockets traveling along the bottom (glass) surface experienced an additional frictional force. Such microrockets were used in control and mixture experiments to increase the interaction time between the microrocket and CEA-cells. The microrockets were magnetically guided towards the CEA+ and CEA- cells to study and identify the cell-microrocket interaction which was monitored using a Nikon Eclipse TE2000S fluorescence microscope. Videos were captured using CoolSNAP HQ2 camera, 20× objective (unless mentioned otherwise) and acquired at the frame rate of 10 using the Metamorph 7.1 software (Molecular Devices, Sunnyvale, CA). Snap shot images in static cell-capture studies on mixture samples were taken with a DeltaVision deconvolution microscope.

3.3.2.6 Microrocket Cellular Transport Calculations

A nanovehicle with a large towing force is an important selection criterion for the cellular transport. Although many catalytic nanomotors have shown the ability to carry objects up to 5 μm in diameter,[25] there is no report of utilizing such nanomotors for cell (diameter 16 μm) manipulation in viscous physiological media. Using Stokes law (Equation 1), we can estimate the force necessary to counter the drag force (**Fd**)

that a cell would experience at a constant velocity of one body length per second in the working solution:

$$\mathbf{Fd} = 6\pi\mu r \quad (1)$$

where μ is the solution viscosity, r is the cell radius and v is the linear velocity of the cell (16 μm/s). Calculations using following values reveal that the following forces are needed to carry such a large cell at a reasonable speed in the different media: Fuel solution containing 7.5% (w/v) H2O2 in 1X PBS, 1% (w/v) sodium cholate (2.5 pN for visocity 1.05 cP), uel solution containing 7.5% (w/v) H2O2 in 25% (v/v) human serum, 1% (w/v) sodium cholate (2.8 pN for visocity 1.14 cP), and Human Blood (12.1 pN for visocity 5 cP).

In order to determine the propulsive force of our microrocket, we used Stokes's drag law for a cylinder as shown in Equation 2, assuming that the microrocket experiences drag as a solid cylinder[27] (as the fluid can not freely flow through the oxygen-bubble containing microrocket and negating the slight 2-4 degree angle along the microrocket, i.e., approaching a cylindrical shape).

$$\mathbf{F}_d = \frac{2\pi\mu L}{\ln\left(\frac{2L}{R}\right) - 0.72} v \quad (2)$$

where R and L are the radius and the length of the microrockets (2.5 and 60 μm, respectively). Although such modified microrockets have a sufficient force to transport these large cells, it is important that they do not apply a large shear force which could prevent binding from occurring or disturb the viability of the captured

cells. The shear stress (Tao) exerted as a result of microrocket interaction with the cell can be calculated based on the following equation 3:

$$\tau_s = \frac{F_d}{A} \tag{3}$$

where A represents the interaction area. Values of the drag force applied by the anti-CEA mAb-modified microrocket to the carried cell are summarized in Table 3.3.1.

Table 3.1 Drag forces and shear stress applied to the carried cell as a function of the speed of the anti-CEA mAb-modified microrocket in different working media.

* anti-CEA mAb-modified microrocket moving in the bottom plane.

Medium	v, μm/s	F_d, pN	τ_s, dyn/cm^2
Fuel solution containing 7.5% (w/v) H_2O_2 in 1× PBS, 1% (w/v) sodium cholate	150	18.1	2.3
Fuel solution containing 7.5% (w/v) H_2O_2 in 25% (v/v) human serum, 1% (w/v) sodium cholate	100	13.3	1.7
Fuel solution containing 7.5% (w/v) H_2O_2 in 1× PBS, 1% (w/v) sodium cholate*	45	5.7	0.7

The interaction area was estimated as 2/3 of the average cell diameter for the width, and 1⁄2 of the microrockets circumference as the height (7.85 μm). Such estimates are based on visual observations which show a slight cell deformation around the microrocket as it passes. Therefore, the average contact area is 78.5 pm2 and the shear stress is directly proportional to the force and ultimately to the

microrocket speed. The values obtained for the shear stresses in PBS and human serum (Table 3.3.1) are similar to that obtained for cell capture using microchip technology.[28] The lower shear stress (0.7 dyn/cm2) induced by the anti-CEA mAb-modified microrocket in the control experiments ensures an increase in binding affinity between the anti-CEA mAb-modified microrocket and the CEA on the cell surface during pick up. Once the cancer cell was captured by the anti-CEA mAb-modified microrocket, the interaction is strong enough for retaining the cell upon experiencing larger shear stresses.

3.3.2.7 Cancer cells viability under experimental conditions

Trypan blue exclusion test was used to determine the number of viable cells present in a cell suspension after exposure to the conditions used in the capture and transport experiments. The cancer cells were incubated in PBS solutions containing 1% of sodium cholate and various concentrations of the peroxide fuel. After different incubation times the cell suspension was mixed with the dye and then it was examined under a microscope to determine whether the cells take up or exclude the dye. The results of the viability are show a >90% viability for an hour for peroxide concentrations under 2%. For higher concentrations up to 8% cells were viable for 10-25 minutes. It should be noted that under all conditions assayed dead cells retain spherical shape (no cell lysis).

3.3.3 CTC Isolation Results and Discussion

3.3.3.1 Microrocket movement in Serum

Practical cancer-cell-sorting applications require that effective motor propulsion is maintained in relevant physiological fluids. A long trail of microbubbles, catalytically generated on the inner platinum surface and released from the rear of the microtube. Such ejection of bubbles propels the microrocket in the diluted serum medium at a relatively high speed of about 85 $\mu m\, s^{-1}$. The sandwiched ferromagnetic (Fe) layer of the microrocket (see the Experimental Section) offers convenient guidance of the microrocket through tuning of the external magnetic-field direction. To facilitate effective propulsion and navigation in such biological media (even after the surface functionalization) the thickness of the Fe layer was increased at least three times compared to that in previously described microrockets.[14,15,25]

3.3.2.2 Pickup of CTC Cells in Biological Fluids

These mAb-functionalized microrockets can selectively bind to target cancer cells and then effectively transport them in phosphate-buffered saline (PBS) and serum. For example, the time-lapse images of Figure 3.3.2 along display the pickup of a pancreatic cancer cell bearing the antigen (CEA+) by the anti-CEA mAb-modified microrocket in PBS (a) and diluted human serum (b). These images demonstrate the movement of the microrocket towards the CEA+ cell (top panel), the dynamic capture of the cell (middle panel), and subsequent directed travel of the cancer-cell-loaded micromotor over a preselected path (bottom panel) without compromising the trajectory of the microrocket movement. The high speed of the microrocket is only

slightly affected by the cell loading (e.g., decreasing from 85 to 80 μm s^{-1} in serum environment), reflecting its high towing force. Such successful pickup is observed at nearly 80 % (n=43) of the time during the first interaction between the modified microrockets and the CEA+ cells while the efficiency decreases to 70 % in serum. The cells were not observed to nonspecifically bind to the microrocket during the various control experiments except in the case when they were sucked up into the opening of the microrocket (representing 2 % of the time, n=120).

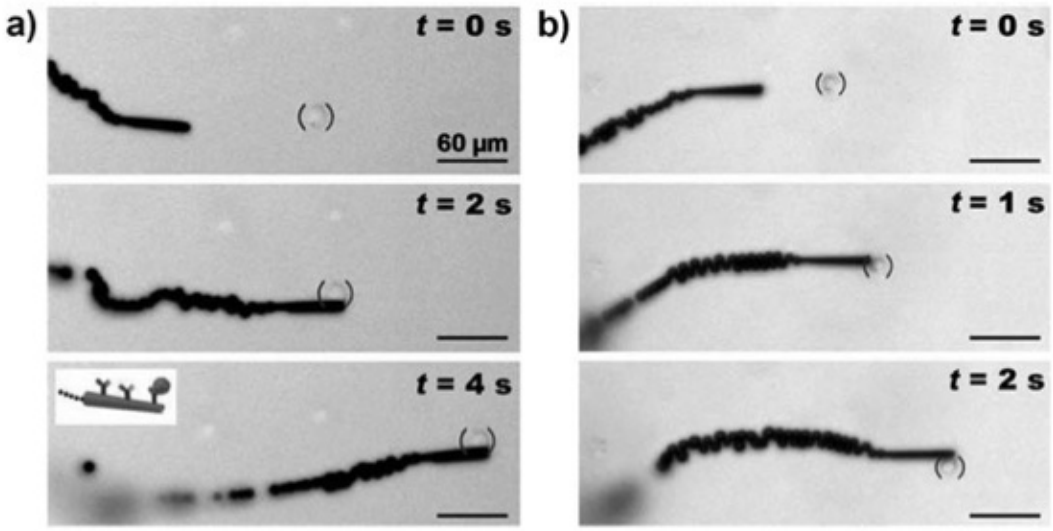

Figure 3.3.2 Pickup and transport in PBS and diluted serum. Time-lapse images demonstrate the pickup and transport of a CEA+ pancreatic cancer cell by an anti-CEA mAb-modified microrocket in PBS (a) and human serum (b) at intervals of 2 and 1 s, respectively. Conditions: a) 1×PBS buffer (pH 7.4) and b) diluted human serum, containing 7.5 % (weight/volume) H_2O_2 and 1 % (w/v) sodium cholate. The CEA+ cells are accented by using solid parentheses.

The substantial force essential for transporting a relatively large (≈16 μm) cancer cell reflects the bubble recoiling propulsion mechanism of the microrockets. The velocity-dependent drag force of the microrockets has been estimated from Stokes′ law (see above methods). The minimum force necessary for transporting such large cells at one body length per second is 2.5 pN (see Experimental Methods), which is an order of magnitude larger than the force generated by previously developed magnetically or chemically powered nano/microscale motors.[9,69]

Unmodified microrockets usually move at a high speed of up to 2 mm s^{-1} in PBS media (not shown), thus exerting a force up to 250 pN. However, after the surface modification with the antibody these microrockets travel in the same bulk media at a speed of up to 150 μm s^{-1}, thus generating an estimated force of about 18 pN. Partial blocking by adsorbed proteins and sulfur poisoning of the catalytic platinum surface[70] may account for this diminished speed. In the presence of diluted serum, the maximum microrocket speed in the bulk solution further drops to about 100 μm s^{-1}, reflecting the increased solution viscosity. Even at the lower speed, the microrockets have sufficient force (>13 pN) to overcome the additional drag force caused by the capture of a cancer cell and we observed that they can transport the cell over long periods (>60 s). The lower microrocket speed is advantageous for the cell capture and transport as it reduces the shear stress and allows for sufficient antigen/antibody interaction. The upper limit of the microrocket speeds in PBS and serum results in estimated shear stresses of 2.3 and 1.7 dyn cm^{-2}, respectively (see Table 3.3.1 in Experimental Methods). Such values have been commonly observed

when flowing cells are selectively captured in microfluidic devices through antibody interactions.[58,71]

3.3.2.3 Receptor Specific Cellular/Micromotor Interactions

The specific binding of the CEA+ cancer cells to anti-CEA mAb-modified microrockets was verified by control experiments. We studied the interactions between anti-CEA mAb-modified microrockets and the pancreatic cancer cells without antigen (CEA−) and between SAM-modified microrockets without the mAb and the CEA+ pancreatic cancer cells (see Experimental Methods for preparation of these "control" microrockets). The results illustrate that none of the control microrockets have the capability of picking up cancer cells; only the anti-CEA mAb-modified microrockets are able to capture the target CEA+ cancer cells. For these control experiments, we deliberately selected microrockets that moved slower along the glass slide interface (average speed of 45 $\mu m\, s^{-1}$) as a way to minimize the exerting shear stress (0.7 dyne cm^{-2}, see Table 3.3.1 in the Experimental Methods) and maximize the microrocket/cell interaction time. We further confirmed that the interaction between the CEA+ cell and the mAb-modified microrocket was strong and specific by oscillating the pair vigorously using a magnet. These results, along with the subsequent studies involving cells mixture (CEA+ and CEA− cells) clearly demonstrate that the capture of the cancer cell occurs through the specific antigen recognition.

3.3.2.4 Cellular Viability in Micromotor Fuel

The viability of the cells under the conditions used in the present study was examined using the trypan blue exclusion assay (see Methods). The cancer cells were subject to PBS solutions containing various levels of the peroxide fuel. While more than half of the cells remained viable for over 10 minutes at a peroxide level of 8 %, the majority of the cells (>90 %) remained viable after 1 hour of immersion in a 2 % peroxide solution. Such time windows would allow for the retrieval of cells for subsequent analysis. We also observed the ability of the mAb-coated microrockets to bind to dead CEA+ cells or their cellular membrane fragments. Therefore, from the perspective of cell detection, these microrockets can identify any CEA-expressing cell regardless of its viability.

3.3.2.5 Mixed Cellular Isolation Experiment

The ability of the anti-CEA mAb-modified microrockets to identify and isolate target cancer cells was further demonstrated using a mixture of green fluorescently stained CEA+ cancer cells and unstained CEA− cancer cells. As shown in the overlay images of Figure 3.3.3 (taken from Supporting Video 3.3), the microrocket first closely interacts with the CEA− cell (steps 1 and 2), hitting and displacing it to a different focal plane (owing to a lack of reaction). After such direct contact without pickup of the CEA− cell, the microrocket captures and transports a CEA+ cell (steps 4 and 5). The CEA+ cell is tightly bound to the modified microrocket during deliberate oscillations. This selective binding was confirmed by exposing the sample to a blue light (460 nm), which excites the CEA+ cells stained with a green fluorescent dye

(step 5). The CEA− cells are indicated by a lack of fluorescence while exposed to blue light at the beginning of the video. A microrocket moving along the bottom plane was chosen; because of its reduced speed we can properly guide the microrocket and distinguish the fluorescent CEA+ cells (from the CEA− cells on the same plane) under the 40× magnification. A similar experiment involving the incubation of modified microrockets (without fuel) with a mixture of CEA+ and CEA− cells further demonstrates the selectivity of the mAb-modified microrocket. These experiments confirm the ability of microrockets to selectively recognize target cancer cells in cell mixtures.

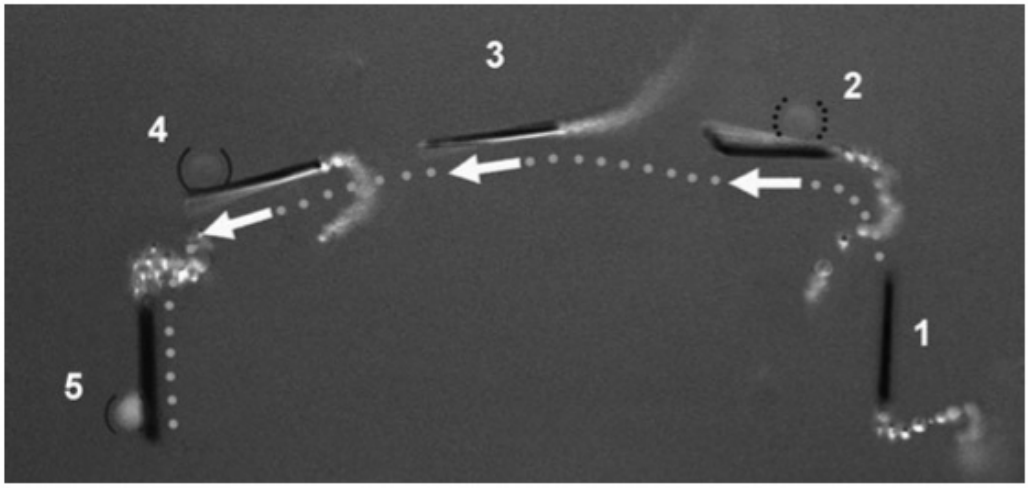

Figure 3.3.3 Isolation of a CEA+ cell in a mixture of cells. The overlay images—taken from video Supporting Video 3.3—show sequential steps (1–5) of movement of the anti-CEA mAb-modified microrocket in a mixture of CEA+ and CEA− cells (solid and dotted parentheses, respectively). For clear visualization, step 5 has been slightly displaced.

3.3.4 CTC Isolation Conclusions

In conclusion, we have demonstrated a new in vitro strategy for isolating cancer cells based on the selective binding and transport ability of mAb-functionalized microengine rockets. These microrockets can be readily functionalized with targeting ligands such as mAb for highly specific cancer cell selection and provide sufficient propulsive force for the efficient transport of the captured target cells in complex media. While the concept has been illustrated for the capture of pancreatic cancer cells, it could be expanded to other cancer cell lines. Such microrocket-based selective capture and transport of tumor cells without preprocessing biological samples holds great promise for extracting CTCs from biological fluids and hence for the early diagnosis of cancer and its recurrence. The autonomous transport properties of the microrockets in viscous fluids such as serum might eliminate the multiple preparatory steps required for the existing magnetic bead-based systems.[58] In addition, we could increase the efficiency of the viable cell separation process by altering the interactions (i.e., by controlling the shear stress). This micromachine-based cell manipulator and sorter could be readily incorporated in microchannel networks for creating integrated microchip devices. Such microchips will rely on the active transport of multiple immuno-micromachines in a blood sample reservoir to induce numerous interactions, high capture efficiency, and single-step isolation of CTCs. Furthermore, this can be extended to accumulating CTCs in a predefined “collection” area by detaching the captured cells.

3.4 Bacteria Isolation and Dissociation

3.4.1 Bacteria Isolation and Dissociation Introduction

Major threats to human health from *E. coli* infection have led to urgent demands to develop highly efficient strategies for isolating and detecting this microorganism in connection to food safety, medical diagnostics, water quality, and counter terrorism.[16,72,73] *E. coli* and other pathogenic bacteria are commonly detected using traditional culture techniques, microscopy, luminescence, enzyme-linked immunosorbent assay (ELISA), biochemical tests and/or the polymerase chain reaction (PCR). These techniques, however, are time-consuming, labor-intensive, and inadequate as they lack the ability to detect bacteria in real time.[74,75] Thus, there is an urgent need for alternative platforms for the rapid, sensitive, reliable, and simple isolation and detection of *E. coli*.

This section presents a new nanomotor strategy for isolating pathogenic bacteria from peroxide-fuel containing clinical, environmental, and food samples, involving the movement of lectin-functionalized microengines. The motion and power of self-propelled synthetic and natural nano/microscale motors have been exploited recently as an attractive route for transporting target biomaterials.[6,33,34,76] The limitations of biological motors for engineered microchip environments[13,33] have motivated the use of synthetic nanomotors for diverse biomedical and bioanalytical applications.[6,9,11] Particularly attractive for such applications are bubble-propelled microtube engines owing to their efficient movement in fuel-enhanced biological

fluids and their large towing forces.[8,22,23,25] Functionalizing photolitographically prepared rolled-up microtube engines with oligonucleotide or antibody receptors has recently been shown to be extremely effective for capturing and isolating target biomolecules and cells from biological samples.[21,22,37,76] Yet, the preparation of these rolled-up microengines is complex and costly, requiring the use of clean-room facilities. Recently, Gao et al.[38] have developed smaller (8 μm) and highly efficient microtube engines, which can be mass-produced through a low-cost membrane template electrodeposition technique and offer ultrafast speeds (>300 body lengths/s) along with low fuel requirements (down to 0.2%) in optimal conditions.[38]

The efficient bacterial isolation platform, described in this paper, relies on the attractive behavior of these easily prepared microengines along with their functionalization with lectin receptors. Lectins are readily available glycoproteins that offer an attractive route for recognizing carbohydrate constituents of bacterial surface, via selective binding to cell-wall mono- and oligosaccharide components.[77] For example, ConA, the lectin extracted from *Canavalia ensiformis* and used in the present work, is a mannose- and glucose-binding protein that is capable of recognizing specific terminal carbohydrates of Gram-negative bacteria such as the *E. coli* surface polysaccharides.[78,79] Furthermore, lectins have been recently used as the biosensor recognition elements for bacterial detection[81-86] but not in connection to nanomachines or nanoscale motion-based isolation.

As illustrated in Figure 3.4.1 (left), the presented nanoscale bacteria isolation strategy utilizes the movement of ConA-functionalized microengines to scour, interact,

and isolate pathogenic bacteria from distinct complex samples. A second goal of the present work is to demonstrate a bacterial target unloading scheme through the controlled release of the captured bacteria from a moving synthetic microengine. Such triggered release has been accomplished by using a low-pH glycine solution that is able to dissociate the lectin-bacteria complex (Figure 3.4.1, right). Finally, we present the ability of the microengines to simultaneously capture and transport both the target bacteria as well as polymeric drug-carrier spheres (using the lectin and magnetic interactions, respectively). Such dual action, coupling the *E. coli* isolation with "on-the-spot" therapeutic action, adds a completely new and unique theranostics ("identify and eradicate") capability to nanomachine platforms. Overall, the template-prepared lectin-modified microengines hold considerable promise for diverse biomedical, food safety, and biodefense applications.

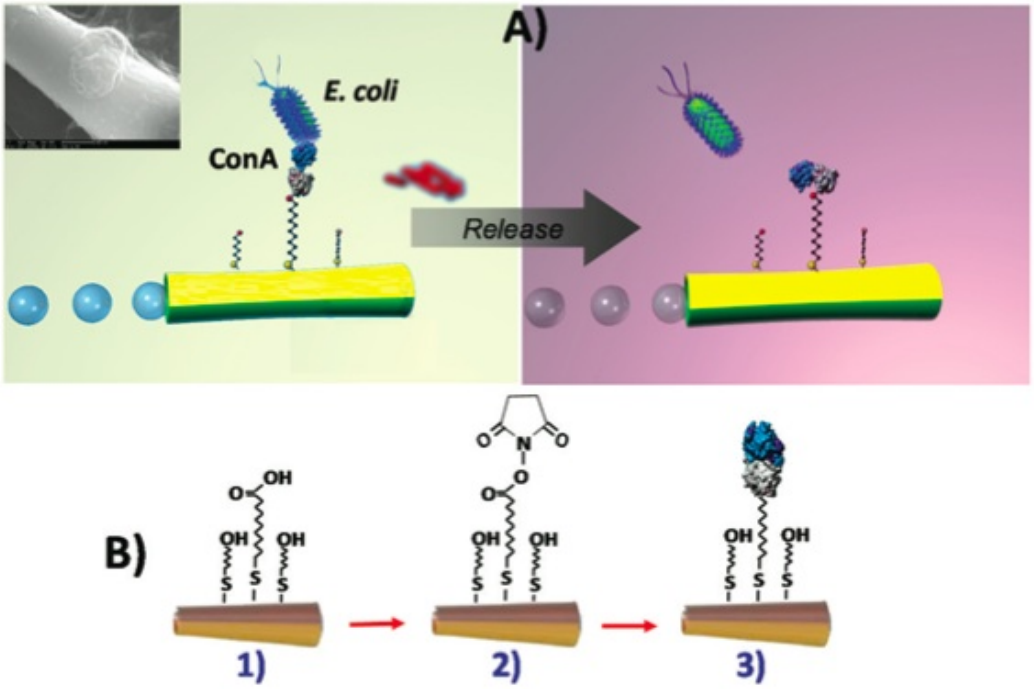

Figure 3.4.1 Lectin-modified microengines for bacteria isolation. Schemes depicting (A) the selective pick-up, transport, and release of the target bacteria by a ConA-modified microengine, and (B) surface chemistry involved on the microengines functionalization with the lectin receptor. Upon encountering the cells, the ConA-functionalized microengines recognize the *E. coli* cell walls by O-antigen structure binding-allowing for selective pick-up and transport. Inset (in Scheme A, top left side): a SEM image of a portion of a ConA-modified microengine loaded with an *E. coli* cell. Scheme A, right side: Release of the capture bacteria by navigation in a 10 mM glycine solution, pH 2.5. Scheme B: Steps involved in the microengines gold surface functionalization. (1) Self-assembling of MUA/MCH binary monolayer; (2) activation of the carboxylic terminal groups of the MUA to amine-reactive esters by the EDC and NHS coupling agents; and (3) reaction of NHS ester groups with the primary amines of the ConA to yield stable amide bonds.

3.4.2 Bacteria Isolation and Dissociation Experimental Methods

3.4.2.1 Methods Reagents and solutions

6-Mercaptohexanol (MCH), 11-mercaptoundecanoic acid (MUA), N-hydroxysuccinimide (NHS), 1-(3- dimethylaminopropyl)-N'-ethylcarbodiimide hydrochloride (EDC), polyaniline (PANI), lectin from *Canavalia ensiformes* (Concanavalin A, ConA), Ulex europaeus (UEA), acetic acid sodium salt,

ethanolamine, 2-(*N*-morpholino) ethanesulfonic acid (MES), CaCl2 and MnCl2 were purchased from Sigma-Aldrich. Hydrogen peroxide (30% w/w) and Triton X-100 were purchased from Fisher Scientific.

The BB solution consisted of a 0.1 M acetate buffer, pH 5.0, containing 1 mM Mn2+ and 1 mM Ca2+. These two divalent metals are necessary in order to get an active ConA conformation for its binding to carbohydrates.[79,84] A 0.1 M MES buffer solution pH 5.0 was used for the modification of the microengines. A 5% (w/v) Triton X-100 solution was prepared daily in this BB solution. 1 M ethanolamine solution pH 8.5 was used as a blocking agent for amine reactive-esters. Glycine, used to promote bacteria unloading was purchased from EM Science. All chemicals were analytical-grade reagents used as received without any further purification and prepared by dilution in 18.2 MΩ cm Milli-Q deionized water when not otherwise specified. Experiments were carried out at room temperature.

For the preparation of the magnetic PLGA microparticles several chemicals were purchased: triethylamine (Sigma-Aldrich), dichloromethane (Sigma-Aldrich), PLGA-ester (50:50 lactic acid: glycolic acid, IV 0.82 dL/g from Lactel, Pelham, AL), oleic-acid coated 10 nm-Fe3O4 nanoparticles (OceanNanoTech; Fayetteville, AR), polyvinyl alcohol (PVA, MW 85 kDa, 80% hydrolyzed, Sigma- Aldrich) and centrifuge filters (Amicon, 100 kDa MW cut-off (MWCO). Standard White Polycarbonate "Track Etch" Membrane Filters from SPI-PoreTM were used to obtain different size of microparticles.

Bacterial strains of *E. coli* NEB 5-a (New England Biolabs) were obtained from the Clinical Microbiology Laboratory, University of California Los Angeles (UCLA), with approval from the UCLA and Veterans Affairs institutional review boards and appropriate Health Insurance Portability and Accountability Act exemptions. The pellets were received in centrifuge tubes and were stored at -80 °C until use. Overnight bacterial cultures were freshly inoculated into Luria broth (LB) and grown to logarithmic phase as measured by the optical density at 600 nm. Concentrations in the logarithmic-phase specimens were determined by serial plating. *S. aureus* cells (10% wet w/v of essentially non-viable *S. aureus* Cowan strain cells in 0.04 M sodium phosphate buffer, pH 7.2, 0.15 M NaCl containing 0.05% NaN3) were supplied by Sigma and *S. cerevisiae* were supplied by Science Stuff. Human urine samples were collected daily, drinking water and apple juice was purchased in a local supermarket and sea water samples (pH 8) collected from the shores of La Jolla, CA. All these real samples were inoculated with the appropriate concentration of bacteria at the moment of the experiment.

3.4.2.2 Microengine fabrication

Microtube engines were prepared by electrodepositing sequential layers into a cyclopore polycarbonate membrane, which contains numerous double-cone-shaped micropores with a maximum diameter of 2 μm (Catalog No 7060-2511; Whatman, Maidstone, U. K.). Standard electrodepostion of an outer PANI layer and inner Pt layer was conducted via a 3-electrode set-up, as was recently described by Gao et al.[38] In brief, A 75 nm gold film was first sputtered on one side of the porous membrane to

serve as working electrode. PANI was electropolymerized for 5 sec at +0.80 V (*vs* Ag/AgCl) from a plating solution containing 0.1 M H2SO4, 0.5 M Na2SO4 and 0.1 M PANI and Pt was galvanostatically deposited for 3600 sec at a constant current of -2 mA using a commercial platinum plating solution (Platinum RTP; Technic Inc, Anaheim, CA). After electrodeposition, the gold film was removed by hand polishing with alumina slurry. In this study a shorter polishing time was used in the preparation process, to increase the area of the modified gold surface and minimize nonspecific capturing of the bacteria (by the mouth suck- in). This polishing procedure led to a larger inner opening on the smaller-diameter side of the microengine, and hence to oxygen bubbles emerging from that side, while maintaining the characteristic efficient propulsion and high towing force.[3] The membrane was then dissolved and repeatedly washed in methylene chloride, ethanol and ultrapure water. The wires solution was then evaporated onto glass slides before the sequential deposition of 10 nm Ti (adhesion layer), 26 nm Ni (magnetic layer), and 12 nm of Au (functionalization layer) over the microtubes using electron beam deposition. This additional steps provide the necessary magnetic directional control and surface modification capabilities for the appropriate guidance and pick-up of target bacterial cells.

3.4.2.3 Microengines modification

The external gold surface of the microengines was modified by an overnight immersion in a binary mixture of 0.25 mM of MUA and 0.75 mM of MCH in absolute ethanol. After washing with Milli-Q water, the resulting mixed monolayer-modified microengines were treated with a 20 mM NHS and 10 mM EDC in 0.1 M MES buffer

solution pH 5.0 for 30 min, washed 1 min with BB solution and immersed 2 h in a BB solution containing 9 mg/ml of ConA (or UEA) receptor. The remaining amine reactive-esters from the activated monolayer were blocked with 1 M ethanolamine solution, pH 8.5, for 30 min and later resuspended in BB solution. Between each incubation and washing steps the microengines were isolated by centrifugation at 6,000 rpm during 4 min; all experiements were carried out at room temperature.

'Control' microengines (without the lectin receptor) were prepared using the same protocol (with the SAM assembly, activation and blocking steps) but omitting the addition of the Con A and carrying out the corresponding incubation in BB.

3.4.2.4 Preparation of bacterial suspension

E. coli stock suspension were prepared by resuspending the appropriate pellet containing 10^7 colony forming units (cfu) bacteria in 100 μL of BB solution or in the undiluted sample matrix under study. This suspension was serially diluted in the same buffer (or sample matrix) to provide different concentrations of bacterial cells. *S. cerevisiae* and *S. aureus* stock solutions were prepared daily by resuspending the appropriate weight of the yeast or by diluting the required volume of the commercially-attenuated *S. aureus* cells suspension in the BB solution or in the sample under study.

3.4.2.5 Identification and isolation of target bacteria

For the detection and isolation of the target bacteria, 2 µl of modified-microengines suspension, 2 µl of 5% (w/v) Triton X-100 (prepared also in BB solution) and 2 µl of 30% (w/v) H2O2 solutions were mixed onto a freshly cleaned glass slide. Once the microrockets were deemed to possess the proper movement and magnetic guidance, 2 µl of the diluted bacterial cell suspension (prepared in the sample matrix or in the BB solution) were added to the mixture. The microengines were then magnetically guided towards the target cells and monitored using a Nikon Eclipse Ti-S/L100 optical microscope. Videos were captured using Hamamatsu digital camera C11440, 40×objective (unless mentioned otherwise) and acquired at the frame rate of 20 fps using the NIS-Elements AR 3.2 software. To test the performance of the lectin-based microengines in complex matrixes the undiluted sample under study was inoculated with the appropriate concentration of bacteria.

It is worth to mention that according to the protocol described all the inoculated matrixes (originally undiluted) were finally diluted 4 times after mixing with equal volumes of the other 3 solutions required by the bioassay (microengines, H2O2 and Triton X-100, to yield a final fuel and surfactant concentrations of 7.5% (w/v) and 1.25% (w/v), respectively. Arana et al.[87] demonstrated that the number of bacteria with intact cytoplasmic membranes (viable) is still high even working with more than 1 % of H2O2, despite a sharp loss in culturability.

3.4.2.6 Unloading experiments:

After capturing target bacteria following exactly the same protocol described in the previous section, 12 μL of the dissociation solution (10 mM glycine pH 2.5) were added to the glass slide. We monitored the navigation of the Con A-modified microengines in this solution during the required time to release the captured bacteria.

3.4.2.7 Preparation of the magnetic PLGA microparticles

The magnetic PLGA microparticles were freshly prepared by oil-in-water emulsion method.[88] The PLGA-ester (50:50 lactic acid: glycolic acid, IV 0.82 dl/g from Lactel, Pelham, AL) was dissolved in chloroform and mixed with oleic-acid coated 10 nm-Fe3O4 nanoparticles (400μ L, OceanNanoTech; Fayetteville, AR). This oil phase solution was added to water phase PVA (1.5 mL, 2% (w/v)) to stabilize the formed magnetic PLGA particles. The mixture was vortexed for 3 minutes and sonicated for 6 min. Chloroform was evaporated overnight by gentle stirring. Particles with 1-2 μm were separated from the bulk solution by using 1 and 2 μm pore diameter polycarbonate filter membranes (Whatman Inc.). This PLGA fraction was diluted and 2 μl of the solution were added to the above microengine/bacteria mixture when performing experiments.

3.4.3 Bacteria Isolation and Dissociation Results and Discussion

3.4.3.1 Concept

The fabrication of the microengines involves a template-based electrodeposition of a polyaniline (PANI)/Pt bilayer microtube and e-beam vapor deposition of outer Ni/Au layers that are essential for magnetic navigation and surface functionalization. As illustrated in Figure 3.4.1B, such functionalization involves the self-assembly of alkanethiols and subsequent conjugation of the lectin receptor. The template fabrication process results in 8 μm long microtube engines that are substantially smaller than the common rolled-up tubular microengines. The relative similar dimensions of the microengine and the target bacteria (~2 μm long × 0.5 μm in diameter) permit convenient real-time optical visualization of the isolation process without the need for additional labeling. By varying the membrane pore size and deposition time, the microengine's aspect ratio can be tailored for meeting the needs of specific target bacteria detection paradigms. Similar to rolled-up microengines,[8,14,15,20,37] the template-prepared microengines are propelled efficiently in different media via the expulsion of oxygen bubbles generated from the catalytic oxidation of hydrogen peroxide fuel at the inner Pt layer.[38] The high speed of the template-prepared PANI/Pt bilayer microtube engines in the present working medium (300 μm/s) is reduced by ca. 50% after the vapor deposition of the outer Ni/Au layers to around 150 μm/s.

Next, the microengine functionalization protocol was optimized for efficient lectin-bacteria interaction and locomotion. As illustrated in Figure 3.4.1B, functionalization was accomplished by conjugating the lectin to the outer gold surface of the microengines via a self-assembled monolayer (SAM). A mixture of 11-mercatoundecanoic acid (MUA) and 6-mercaptohexanol (MCH) was used to create the binary SAM while 1-ethyl-3-(3-dimethylaminopropyl) carbodiimide (EDC)/*N*-hydroxysuccinimide (NHS) chemistry was used to activate the MUA carboxyl-terminated groups for conjugation with ConA (see Methods for additional details). To promote favorable target accessibility while minimizing nonspecific adsorption, the binary SAM was prepared using optimal alkanethiol concentrations of 0.25 mM MUA and 0.75 mM MCH.[89] The relatively low thiol concentrations ensure minimal poisoning of the inner catalytic platinum surface and hence a high catalytic activity.[60] Such surface modification of the Au/Ni/PANI/Pt microtubular engines resulted in an additional speed reduction, down to 80 μm/s. This speed is sufficient to perform cellular towing tasks and is relatively faster than previously reported rolled-up microengines.[14,15] After the SAM activation, the lectin receptor was immobilized via NHS/EDC coupling using a binding buffer (BB) solution containing 9 mg/mL of ConA. This step did not affect the microengine speed. Overall, despite the ~75% total reduction in speed from the entire modification process, the microengine's speed and related force were sufficient to carry multiple bacteria or different cargoes.

3.4.3.2 Specificity in Biological Samples

The specific binding of the ConA-modified microengines to *E. coli* was examined first in inoculated human urine samples. These urine samples were inoculated with *E. coli* target bacteria along with a 5-fold excess *Saccharomyces cerevisiae* (*S. cerevisiae*), a species of yeast frequently responsible for yeast infections and UTIs. Figure 3.4.2 demonstrates the selective binding and transport of the rod-shaped ($\sim$2 μm length) gram-negative *E. coli* bacteria (delineated by green dotted circles). In contrast, the modified microengine does not capture the round-shaped *S. cerevisiae* cells ($\sim$5 μm in diameter) even when multiple contacts occur (delineated by red dotted circles) (Figure 3.4.2a). The distinct size ($\sim$2 μm versus 5 μm) and shape (rod versus round) of the target *E. coli* and control *S. cerevisiae*, respectively, allow clear optical visualization and discrimination between the target and nontarget cells during the motor navigation. Note that the similar size scale of the microengine and bacteria facilitates real-time visualization of the binding process (see Figure 3.4.2). This selective and rapid capture mechanism is attributed to the nearly instantaneous recognition of the sugar moieties on the bacterial cell wall by the lectin-modified microengine (Figure 3.4.2). Indeed, the multivalent binding of ConA to the O-antigen *E. coli* surface favors strong adhesion of *E. coli* to the ConA-modified microengine surface[79,80] as illustrated clearly in the SEM image depicted in Figure 3.4.1A (top left side). To further corroborate the specificity of the ConA-modified microengines, we tested human urine samples inoculated with both *E. coli* and a 5-fold excess of another urinary pathogen *Staphylococcus aureus* (*S. aureus*), (i.e., a small, round, gram-

positive UTI-related bacteria).[91] Both capture experiments results with *S. cerevisiae* and *S. aureus* controls in urine specimens demonstrate the high specificity of the ConA-modified microengines toward *E. coli* and their ability to selectively capture and transport microorganisms from complex clinical samples.[92]

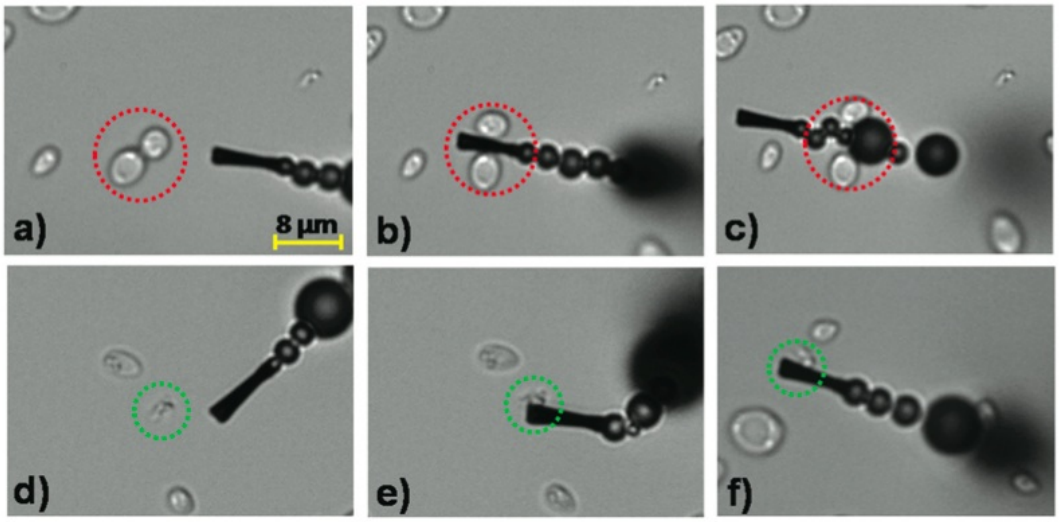

Figure 3.4.2 Selective interaction between the ConA-functionalized microengines and the *E. coli* target bacteria in a fuel-enhanced and *E. coli* inoculated human urine sample. Time-lapse images taken before, during, and after interaction of the ConA-modified microengines with *S. cerevisiae* negative control (a–c, respectively) and *E. coli* target (d–f, respectively) cells. Urine samples are inoculated with *E. coli* (2.25×10^7 colony forming units (cfu/ml) or 4.5×10^4 cfu on the glass slide) and a 5-fold excess of *S. cerevisiae* and finally diluted 4 times in the glass slide to include the functionalized microengines and the fuel solutions (see Methods for additional details). Final fuel conditions: 7.5% (w/v) H_2O_2, 1.25% (w/v) Triton X-100. The *E. coli* and *S. cerevisiae* cells are accented by dashed green and red circles, respectively.

Additional experiments were performed with "control" microengines (i.e., without the immobilized ConA; prepared as described in the Methods) to demonstrate that the surface-confined lectin is solely responsible for the bacterial isolation. For example, these "control" microengines do not capture *E. coli* even after multiple

contacts with the bacteria while navigating in the BB solution containing a 10-fold excess of *E. coli* (compared to solutions used here with the ConA-modified microengines). These results, along with mixture experiments involving large excess of a gram-positive bacteria or yeast, clearly demonstrate that the capture of the *E. coli* occurs through the specific lectin-carbohydrate recognition and confirm the high specificity of surface-confined ConA toward lipopolysaccharide O-antigens characteristics of gram-negative bacteria.[80,81,83,86,93] The high selectivity, illustrated in Figure 3.4. is attributed not only to the high affinity of the lectin to the target bacteria but also to the effective minimization of nonspecific binding associated with the highly dense hydrophilic SAM surface coating. These data also confirm that the hydrogen peroxide fuel and Triton X-100 surfactant, essential for the microengine movement, do not compromise the specific lectin-bacterial cell wall interaction or the integrity of the assembled binary SAM.

3.4.3.3 Reproducibility

The reproducibility of the new motion-based isolation was investigated by using five different batches of ConA-modified microengines following identical processing steps. The results (not shown) demonstrated very small (~5%) differences in the bacteria capture efficiency among different batches of modified microengines, demonstrating the reliability of their fabrication, modification, and movement processes. While lectin-bacteria binding often requires long (30–60 min) incubation times,[14,93] the microengine-induced localized convection appears to dramatically accelerate the binding process. Short contact times with the target bacteria (on the

order of seconds) are thus sufficient for its effective capture. The new microengine platform thus presents a unique approach for meeting the need for rapid, direct, and real time isolation of biological agents.

3.4.3.4 Bacteria Isolation for Diverse Testing Applications

The practical utility of the new microengine approach toward diverse applications was illustrated by the ability of the lectin-modified microengines to recognize the target bacteria in different fuel-enhanced and *E-coli*-inoculated real samples. These samples included common beverages (ranging from drinking water to apple juice) and environmental matrices (such as seawater). Results (not shown) illustrate that the functionalized microengines display an immediate "on the fly" *E. coli* capture upon contacting the target bacteria in each of these real samples. A successful pick-up rate (during the first engine-cell contact) of nearly 90% (n = 50) has been observed in all the tested matrices. In rare occasions (less than 1% of the times), the cells were inhaled into the front opening of the modified microrocket (i.e., captured nonspecifically). Overall, the results demonstrate the ability of the modified microengines to pick-up bacteria in the presence of diverse conditions, different environments, and matrix effects, including low and high sugar concentrations (as in drinking water and apple juice, respectively) as well as high salt (seawater and urine) environments. Note also that the average speed of the functionalized microengines varies with the specific sample matrix. Despite small decrease in the microengine speed (~10%) after the *E. coli* capturing, efficient propulsion and transport of the captured bacteria are maintained using the different sample matrices with highest

average speeds of 50 μm/s in BB and lowest (27.3 μm/s) in drinking water. These estimated speeds were of the ConA-Functionalized Microengines in Different Media Inoculated with 1.8×10^7 cfu/ml of *E. coli.* Media finally diluted 4 times after mixing with the ConA-microengines and the fuel solutions required by the bioassay. Fuel composition: 7.5% (w/v) H_2O_2 + 1.25% (w/v) Triton X-100.

3.4.3.5 Bacterial cell/ConA-modified microengines Interaction

The interaction between the bacterial cell and the ConA-modified microengines is not only highly selective but also very robust. For example, the ability of the microengines to pick up and carry an *E. coli* cell that had adhered to the glass slide, as well as their ability to simultaneous transport of multiple bacteria by a single ConA-modified microengine has been often observed. The drag force needed to perform such tasks can be calculated via Stokes' law.[22] For example, a drag force of 1 pN can be estimated for a microengine moving at 33.9 μm/s in seawater, assuming a cylindrical microengine of 8 μm in length and 2 μm in diameter.[78] This force is thereby sufficient to remove a bacterial cell firmly fixated to the glass slide, as has been demonstrated. Note that in the multiple-bacteria transport process, are confined only to half of the microengine, reflecting that only ~50% of its outer surface is covered by the gold layer due to the one-sided e-beam deposition process and the corresponding one-sided functionalization with the lectin receptor.

3.4.3.6 pH Sensitive Unloading of Lectin Bound Bacteria

The ability to isolate and unload target bacteria is critical for identifying pathogenic bacteria serotypes. To facilitate the release of the captured bacteria, the loaded ConA-modified microengines were moved through a low-pH glycine-based dissociation solution that disrupts the sugar-lectin complex[94-96] (Figure 3.4.1, right). Figure 3.4.3 illustrates images, obtained from Supporting Video 3.4 of the lectin-modified microengines before (a) and after (b) 20 min navigation in this dissociation solution. Note that such prolonged continuous movement is observed without replenishing the fuel. The multiple bacteria confined to the moving microengine are clearly released from its surface after movement in the low-pH glycine-based dissociation solution. The efficient removal of the captured bacteria is attributed to the unfolding of ConA in this low pH-solution, thereby dissociating the sugar-lectin complex and releasing the captured bacteria for subsequent reuse.[94-96] The unfolding of the immobilized bioreceptor in this low-pH solution is supported also by the inability of the ConA-modified microengines to capture target bacteria in this medium while contacting it multiple times, as illustrated in Supporting Video 3.4B. These mild dissociation conditions were shown not to affect the sugar binding capacity of the immobilized lectin[81,97,98] or the integrity of the assembled binary monolayer. Thus, a reversible refolding to the original active ConA conformation is expected after navigating in the BB solution, indicating great promise for reusing the same modified microengines in new isolation experiments.

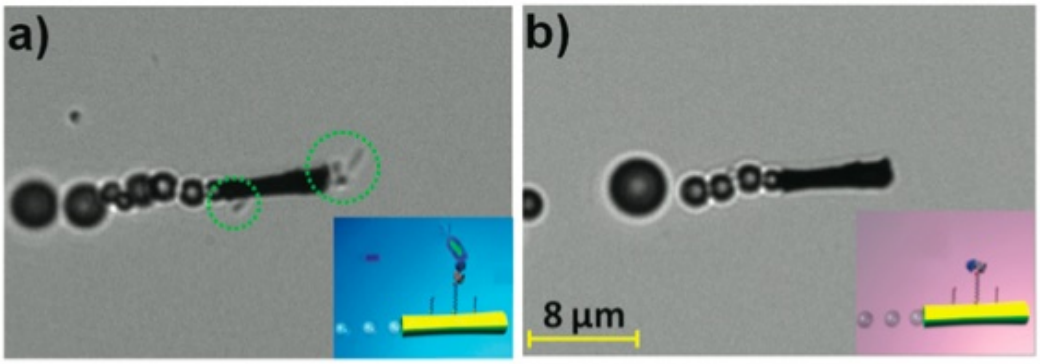

Figure 3.4.3 Release of the captured bacteria from the ConA-modified microengines. Images taken from Supporting Video 3.4 showing an *E. coli*-ConA-modified microengine before (a) and after (b) incubation (20 min) in a 10 mM glycine solution (pH 2.5). Other experimental conditions, as in Figure 3.4.2. *E. coli* cells are accented by dashed green circles.

3.4.3.7 Theranostic Microengines for Multiple Applications

The feasibility of lectin-modified microengines to perform multiple tasks was finally explored. Here, we combine the ability to capture the target bacteria cell with simultaneous transport of common therapeutic polymeric particles toward the creation of the first self-propelling multifunctional (theranostics) device. Common drug carrier microspheres, poly d,l-lactic-*co*-glycolic acid (PLGA) microparticles, containing magnetic iron-oxide nanoparticles, were employed due to their potential to deliver antimicrobial drugs.[99] We have also demonstrated this dual capture and transport functionality, by displaying a ConA-modified microengine picking-up and transporting both an *E. coli* cell and a PLGA magnetic particle. The ConA-modified microengine is capable of first identifying and capturing a noxious bacteria (i.e., *E. coli*) (b), next capturing the magnetic polymeric drug carrier (c), and finally transporting both cargos at the same time (d). Eventually both captured cargoes can be released simultaneously or independently in a specified location for eradication or

identification. Alternatively, future therasonics nanomotor schemes could be developed to navigate a PLGA-loaded microengine in the bacteria-containing sample. Overall, the preliminary data of reveals the unique multifunctionality potential of the modified-microengines for future applications including UTI diagnosis and treatment or water and food quality control.

3.4.4 Bacteria Isolation and Dissociation Conclusions

While a large fraction of the bacteria are expected to remain viable but not culturable (VBNC) after exposure to the peroxide fuel level,[87,100] the new nanomotor 'swim and catch' strategy allows for isolation of different bacteria populations (independent of their viability or culturability). Such VBNC *E. coli* cells, the predominant bacterial population under our working conditions, are not detectable by common culture methods but may retain their capacity to grow and cause infection.[100-104] Hence, this nanomotor method can avoid time-consuming PCR protocols and false negatives associated with culture-based methods when detecting VBNC and nonviable bacteria. The ability to detect potentially infectious VBNC *E. coli* and dead cells is also attractive for tracing the source of an outbreak to identify enterotoxigenic or enterohemorrhagic *E. coli* serotypes such as Shiga toxin (Stx)-producing *E. coli* O157/H7.[102] Whenever needed, new fuel-free magnetically driven nanomotors,[105] functionalized with the lectin receptor, could also be used to ensure full viability of the isolated bacteria.

In conclusion, we have demonstrated the use of new synthetic microengines, functionalized with lectin receptors, for the efficient isolation of target bacteria from diverse real samples. These modified template-prepared microengines offer very attractive capabilities for autonomous loading, directional transport and bacterial unloading (catch and release) toward their subsequent reuse, along with efficient and simultaneous transport of drug nanocarriers. Such ability to perform simultaneously bacteria isolation and directed drug-delivery may help in designing miniaturized theranostics microsystems, integrating dual capture of target species, and transporting and releasing target species in a controlled fashion within spatially separated zones. The incorporation of the new microengine-based bacterial isolation protocol into microchannel networks could lead to microchip operations involving real-time isolation of specific bacteria, and subsequent bacteria lysis and unequivocally identification (by 16S rRNA gene analysis), potentially down to the single-cell level. The diverse capabilities of these lectin-modified hybrid microengines make them extremely attractive for a wide-range of fields, including food and water safety, infectious disease diagnostics, biodefense, and clinical therapy treatments.

Chapter 3.1 is based on the material as it appears in Nanoletters, 2011, by Daniel Kagan, Susana Campuzano, Shankar Balasubramanian, Filiz Kuralay, Gerd Flechsig, and Joseph Wang; Chapter 3.2 is based on the material as it appears in Nanoletters, 2012, by Susana Campuzano, Jahir Orozco, Daniel Kagan, Maria Guix, Wei Gao, Sirilak Sattayasamitsathit, Jonathon Claussen, Arben Merkoçi, and Joseph Wang, J.; Chapter 3.3 is based on the material as it appears in Angewandte Chemie,

2011, by Shankar Balasubramanian, Daniel Kagan, Jack Hu, Susana Campuzano, Maria Jesus Lobo-Castañon, Nicole Lim, Dae Kang, Maria Zimmerman, Liangfang Zhang, and Joseph Wang,; Chapter 3.4 is based on the material as it appears in Analyst, 2011, by Jahir Orozco, Susana Campuzano, Daniel Kagan, Ming Zhou, Wei Gao, and Joseph Wang, The dissertation author was the primary investigator and co-author of these papers.

3.5 References

1. Boom, R.; Sol, C. J. A.; Salimans, M. M. M.; Jansen, C. L.; Wertheim-van Dillen, P. M. E.; van der Noordaa, J. J. Clin. Microbiol. 1990, 28, 495– 503.

2. Duarte, G. R. M.; Price, C. W.; Littlewood, J. L.; Haverstick, D. M.; Ferrance, J. P.; Carrilho, E.; Landers., J. P. Analyst 2010, 135, 531– 537.

3. Kline, T. R.; Paxton, W. F.; Mallouk, T. E.; Sen, A. Angew. Chem., Int. Ed. 2005, 44, 744– 746.

4. Ozin, G. A.; Manners, I.; Fournier-Bidoz, S.; Arsenault, A. Adv. Mater. 2005, 17, 3011– 3018.

5. Mallouk, T. E.; Sen, A. Sci. Am. 2009, 300, 72– 77.

6. Wang, J. ACS Nano 2009, 3, 4– 9.

7. Howse, J. R.; Jones, R. A. L.; Ryan, A. J.; Gough, T.; Vafabakhsh, R.; Golestanian, R. Phys. Rev. Lett. 2007, 99, 048102

8. Mei, Y.; Solovev, A. A.; Sanchez, S.; Schmidt, O. G. Chem. Soc. Rev. 2011, 40, 2109– 2119.

9. Kagan, D.; Laocharoensuk, R.; Zimmerman, M.; Clawson, C.; Balasubramanian, S.; Kang, D.; Bishop, D.; Sattayasamitsathit, S.; Zhang, L.; Wang, J. Small 2010, 6, 2741– 2747.

10. Kagan, D.; Calvo-Marzal, P.; Balasubramanian, S.; Sattayasamitsathit, S.; Manesh, K. M.; Flechsig, G.-U.; Wang, J. J. Am. Chem. Soc. 2009, 131, 12082– 12083.

11. Wu, J.; Balasubramanian, S.; Kagan, D.; Manesh, K. M.; Campuzano, S.; Wang, J. Nat. Commun. 2010, 1, DOI: 10.1038/ ncomms1035.

12. Taira, S.; Du, Y. Z.; Hiratsuka, Y.; Konishi, K.; Kubo, T.; Uyeda, T. Q. P.; Yumoto, N.; Kodaka, M. Biotechnol. Bioeng. 2006, 3, 533– 538.

13. Hiyama, S.; Inoue, T.; Shima, T.; Moritani, Y.; Suda, T.; Sutoh, K. Small 2008, 4, 410– 415.

14. Mei, Y.; Huang, G.; Solovev, A. A.; Bermúdez Ureña, E.; Mönch, I.; Ding, F.; Reindl, T.; Fu, R. K. Y.; Chu, P. K.; Schmidt, O. G. Adv. *Mater.* **2008**, *20*, 4085–4090.

15 Solovev, A. A.; Mei, Y. ; Bermúdez Ureña, E.; Huang, G.; Schmidt, O. G. *Small* **2009**, *5*, 1688–1692.

16. Liao, J. C.; Mastali, M.; Gau, V.; Suchard, M. A.; Moller, A. K.; Bruckner, D. A.; Babbitt, J.; Li, Y.; Gornbein, J.; Landaw, E. M.; McCabe, E. R. B.; Churchill, B. M.; Haake, D. A. *J. Clin. Microbiol.* **2006**, *44*, 561–570.

17. Wu, J.; Chumbimuni-Torres, K. Y.; Galik, M.; Thammakhet, C.; Haake, D. A.; Wang, J. *Anal. Chem.* **2009**, *81*, 10007–10012.

18. Steel, A. B.; Herne, T. M.; Tarlov, M. J. *Anal. Chem.* **1998,** *70*, 4670–4677.

19. Wu, J.; Campuzano, S.; Halford, C.; Haake, D. A.; Wang, J. *Anal. Chem.* **2010**, *82,* 8830–8837.

20. Li, J.; Huang, G.; Ye, M.; Li, M.; Liu, R.; Mei, Y. *Nanoscale,* **2011***, 3,* 5083.

21. Sanchez, S.; Solovev, A. A.; Schulze, S.; Schmidt, O. G. Chem. Commun. 2011, 47, 698– 700.

22. Balasubramanian, S.; Kagan, D.; Hu, C. J.; Campuzano, S.; Lobo-Castañon, M. J.; Lim, N.; Kang, D. Y.; Zimmerman, M.; Zhang, L.; Wang, J. Angew. Chem., Int. Ed. 2011, 50, 4161– 4164.

23. Manesh, K. M.; Cardona, M.; Yuan, R.; Clark, M.; Kagan, D.; Balasubramanian, S.; Wang, J. ACS Nano 2010, 4, 1799– 1804.

24. Sanchez, S.; Solovev, A. A.; Mei, Y.; Schmidt, O. G. J. Am. Chem. Soc. 2010, 132, 13144– 13145.

25. Solovev, A. A.; Sanchez, S.; Pumera, M.; Mei, Y.; Schmidt, O. G. Adv. Funct. Mater. 2010, 20, 2430– 2435.

26. Levicky, R.; Herne, T. M.; Tarlov, M. J.; Satija, S. K. J. Am. Chem. Soc. 1998, 120, 9787– 9792.

27. Paxton, W. F.; Baker, P. T.; Kline, T. R.; Wang, Y.; Mallouk, T. E.; Sen, A. J. Am. Chem. Soc. 2006, 128, 14881– 14888.

28. Sanchez, S.; Solovev, A. A.; Harazim, S. M.; Schmidt, O. G. J. Am. Chem. Soc. 2011, 133, 701– 703.

29. Burdick, J.; Laocharoensuk, R.; Wheat, P. M.; Posner, J. D.; Wang, J. J. Am. Chem. Soc. 2008, 130, 8164– 8165.

30. Başar, N.; Uzun, L.; Guner, A.; Denizli, A. Int. J. Biol. Macromol. 2007, 41, 234– 242.

31. Boto, R. E. F.; Anyanwu, U.; Sousa, F.; Almeida, P.; Queiroz, J. A. Biomed. Chromatogr. 2009, 23, 987– 993.

32. Safarik, I.; Safarikova, M. BioMagn. Res. Technol. 2004, 2, 7

33. Fischer, T.; Agarwal, A.; Hess, H. Nat. Nanotechnol. 2009, 4, 162– 166

34. Schmidt, C.; Vogel, V. Lab Chip 2010, 10, 2195– 2198

35. Guo, P. X.; Erickson, S.; Anderson, D. A. Science 1987, 236, 690– 694

36. Chang, C.-L.; Zhang, H.; Shu, D.; Guo, P.; Savran, C. A. Appl. Phys. Lett. 2008, 93, 153902

37. Kagan, D.; Campuzano, S.; Balasubramanian, S.; Kuralay, F.; Flechsig, G.-U.; Wang, J. Nano Lett. 2011, 11, 2083– 2087

38. Gao, W.; Sattayasamitsathit, S.; Orozco, J.; Wang, J. J. Am. Chem. Soc. 2011, 133 (31) 11862– 11864

39. Tombelli, S.; Mascini, M. Curr. Opin. Mol. Ther. 2009, 11, 179– 188

40. Liu, J.; Cao, Z.; Lu, Y. Chem. Rev. 2009, 109, 1948– 1998.

41. Hansen, J. A.; Wang, J.; Kawde, A.-N.; Xiang, Y.; Gothelf, K. V.; Collins, G. J. Am. Chem. Soc. 2006, 128, 2228– 2229

42. Kato, K.; Goto, R.; Katoh, K.; Shibakami, M. Biosci. Biotechnol. Biochem. 2005, 69, 646– 648

43. Hirabayashi, M.; Taira, S.; Kobayashi, S.; Konishi, K.; Katoh, K.; Hiratsuka, Y.; Kodaka, M.; Uyeda, T. Q. P.; Yumoto, N.; Kubo, T. Biotechnol. Bioeng. 2006, 94, 473– 480

44. Hiyama, S.; Moritani, Y.; Gojo, R.; Takeuchi, S.; Sutoh, K. Lab Chip 2010, 10, 2741– 2748.

45. Zhou, M.; Chen, C.; Du, Y.; Li, B.; Wen, D.; Dong, S.; Wang, E. Lab Chip 2010, 10, 2932– 2936

46. Du, Y.; Bingling, L.; Wei, H.; Wang, Y.; Wang, E. Anal. Chem. 2008, 80, 5110– 5117

47. Centi, S.; Tombelli, S.; Minunni, M.; Mascini, M. Anal. Chem. 2007, 79, 1466– 1473

48. Hu, J.; Easley, C. J. Analyst 2011, 136, 3461– 3468; DOI: 10.1039/c0an00842g

49. Jianwei, J. L.; Xiaohong, F.; Tan, W. Biochem. Biophys. Res. Commun. 2002, 292, 31– 40

50. Strehlitz, B.; Nikolaus, N.; Stoltenburg, R. Sensors 2008, 8, 4296– 4307.

51. Baldrich, E.; Restrepo, A.; O'Sullivan, C. K. Anal. Chem. 2004, 76, 7053.

52. Harreby, M.; Danneskiold-Samsøe, B.; Kjer, J.; Lauritzen, M. Ann. Rheum. Dis. 1987, 46, 601– 604

53. Ding, C.; Ge, Y.; Lin, J.-M. Biosens. Bioelectron. 2010, 25, 1290– 1294

54. Hianik, T.; Ostatna, V.; Sonlajtnerova, M.; Grman, I. Bioelectrochem. 2007, 70, 127– 133.

55. Lin, Z.; Luo, F.; Liu, Q.; Chen, L.; Qiu, B.; Cai, Z.; Chen, G. Chem. Commun. 2011, 47, 8064– 8066.

56. Cao, Z.; Tong, R.; Mishra, A.; Xu, W.; Wong, G. C. L.; Cheng, J.; Lu., Y. Angew. Chem., Int. Ed. 2009, 48, 6494– 6498.

57. Galanzha, E. I.; Shashkov, E. V.; T. Kelly, J.; Kim, W.; Yang, L.; Zharov, V. P.; *Nat. Nanotechnol.* **2009***, 4,* 855–860.

58. Nagrath, S.; Sequist, L. V.; Maheswaran, S.; Bell, D. W.; Irimia, D.; Ulkus, L.; Smith, M. R.; Kwak, E. L.; Digumarthy, S.; Muzikansky, A.; Ryan, P.; Balis, U. J.; Tompkins, R. G.; Haber, D. A.; Toner, M. *Nature* **2007,** *450,* 1235–1239.

59. Adams, A. A.; Okagbare, P. I.; Feng, J.; Hupert, M. L.; Patterson, D.; Göttert, J.; McCarley, R. L.; Nikitopoulos, D.; Murphy, M. C.; Soper, S. A. *J. Am. Chem. Soc.* **2008***, 130,* 8633–8641.

60. A. L. Allan, M. Keeney, J. Oncol. **2010**, 426218.

61 Mirkovic, T.; Zacharia, N. S.; Scholes, G. D.; Ozin, G. A. *ACS Nano* **2010***, 4,* 1782–1789.

62. Wang, J.; Manesh, K. M. *Small* **2010***, 6,* 338–345

63. Paxton, W. F.; Sundararajan, S.; Mallouk, T. E.; Sen, A. *Angew. Chem.* **2006***, 118,* 5546–5556.

64. Ebbens, S. J.; Howse, J. R. *Soft Matter* **2010***, 6,* 726–738.

65. Sundararajan, S.; Lammert, P. E.; Zudans, A. W.; Crespi, V. H.; Sen, A. *Nano Lett.* **2008***, 8,* 1271–1276.

66. Sundararajan, S.; Sengupta, S.; Ibele, M. E.; Sen, A. *Small* **2010***, 6,* 1479–1482.

67. Shi, Z.-R.; Tacha, D.; Itzkowitz, S. H.; Histochem. J. *Cytochem.* **1994***, 42,* 1215–1219.

68. Zieglschmid, V.; Hollmann, C.; Böcher, O. *Crit. Rev. Clin. Lab. Sci.* **2005***, 42,* 155–196.

69 Zhang, L.; Abbott, J. J.; Dong, L.; Peyer, K. E.; Kratochvil, B. E.; Zhang, H.; Bergeles, C.; Nelson, B. J. *Nano Lett.* **2009,** *9,* 3663–3667.

70. Bartholomew, C. H.; Agrawal, P. K.; Katzer, J. R. *In Advances in Catalysis*; Academic Press: New York, 1982; 31, 135– 242.

71. Plouffe, B. D.; Kniazeva, T.; Mayer, J. E.; Murthy, Jr., S. K.; Sales, V. L. *FASEB J.* **2009***, 23,* 3309–3314.

72. Laurino, P.; Kikkeri, R. *Nano Lett.* **2011***, 11,* 73– 78.

73. Guven, B.; Basaran-Akgul, N.; Temur, E.; Tamer, U.; Boyacı, I. H. *Analyst* **2011***, 136,* 740– 748.

74. Wang, R.; Ruan, C.; Kanayeva, D.; Lassiter, K.; Li, Y. *Nano Lett.* **2008***, 8*, 2625– 2635.

75. Arya, S. K.; Singh, A.; Naidoo, R.; Wu, P.; McDermott, M. T.; Evoy, S. *Analyst* **2011***, 136*, 486– 492.

76. Orozco, J.; Campuzano, S.; Kagan, D.; Zhou, M.; Gao, W.; Wang, *J. Anal. Chem.* **2011***, 83*, 7962– 7969.

77. Haseley, S. R. *Anal. Chim. Acta* **2002***, 457*, 39– 45.

78. Loaiza, O. A.; Lamas-Ardisana, P. J.; Jubete, E.; Ochoteco, E.; Loinaz, I.; Cabañero, G.; García, I.; Penadés, S. *Anal. Chem.* **2011***, 83,* 2987– 2995.

79. He, X.; Zhou, L.; He, D.; Wang, K.; Cao, J. *Analyst* **2011***, 136*, 4183– 4191.

80. Shen, Z.; Huang, M.; Xiao, C.; Zhang, Y.; Zeng, X.; Wang, P. G. *Anal. Chem.* ***2007***, *79*, 2312– 2319.

81. Safina, G.; van Lier, M.; Danielsson, B. *Talanta* **2008***, 77,* 468– 472.

82. Lu, Q.; Lin, H.; Ge, S.; Luo, S.; Cai, Q.; Grimes, C. A. *Anal. Chem.* **2009***, 81,* 5846– 5850.

83. Gamella, M.; Campuzano, S.; Parrado, C.; Reviejo, A. J.; Pingarrón, J. M.. *Talanta* **2009***, 78*, 1303– 1309.

84. Wan, Y.; Zhang, D.; Hou, B. *Talanta* **2009***, 80*, 218– 223.

85. Gao, J.; Liu, D.; Wang, Z. *Anal. Chem.* **2010***, 82*, 9240– 9247.

86. Grünstein, D.; Maglinao, M.; Kikkeri, R.; Collot, M.; Barylyuk, K.; Lepenies, B.; Kamena, F.; Zenobi, R.; Seeberger, P. H. *J. Am. Chem. Soc.* **2011***, 133*, 13957– 13966.

87. Arana, I.; Orruño, M.; Pérez-Pascual, D.; Seco, C.; Muela A.; Barcina, I. *FEMS Microbiol. Ecol.* **2007**, *62*, 1–11.

88. Chaisri, W.; Hennink, W. E.; Okonogi, S. *Curr. Drug. Deliv.* **2009**, 6, 69-75.

89. Briand, E.; Salmain, M.; Herry, J. M.; Perrot, H.; Compère, C.; Pradier, C.-M. *Biosens. Bioelectron.* **2006***, 22*, 440– 448.

90. Muder, R. R.; Brennen, C.; Rihs, J. D.; Wagener, M. M.; Obman, A.; Stout, J. E.; Yu, V. L. *Clin. Infect. Dis.* **2006***, 42,* 46– 50.

91. Pistole, T. G. *Annu. Rev. Microbiol.* **1981***, 35,* 85– 111.

92. Gao, J.; Liu, C.; Liu, D.; Wang, Z.; Dong, S. *Talanta* **2010***, 81*, 1816– 1820.

93. Serra, B.; Gamella, M.; Reviejo, A. J.; Pingarrón, J. M.. *Anal. Bioanal. Chem.* **2008***, 391*, 1853– 1860.

94. Švitel, J.; Dzgoev, A.; Ramanathan, K.; Danielsson, B. *Biosens. Bioelectron.* **2000***, 15*, 411– 415.

95. Duverger, E.; Frison, N.; Roche, A. C.; Monsigny, M. *Biochimie* **2003***, 85,* 167– 179.

96. Witten, K. G.; Rech, C.; Eckert, T.; Charrak, S.; Richtering, W.; Elling, L.; Simon, U. *Small* **2011***, 7*, 1954– 1960.

97. Murthy, B. N.; Sinha, S.; Surolia, A.; Indi, S. S.; Jayaraman, N. *Glycoconjugate J.* **2008***, 25*, 313– 321.

98. Yakovleva, M. E.; Safina, G. R.; Danielsson, B. *Anal. Chim. Acta* **2010***, 668*, 80– 85.

99. Lecaroz, M. C.; Blanco-Prieto, M. J.; Campanero, M. A.; Salman, H.; Gamazo, C. *Antimicrob. Agents Chemother.* **2007***, 51*, 1185– 1190.

100. Oliver, J. D. *FEMS Microbiol. Rev.* **2010***, 34*, 415– 425.

101. McDougald, D.; Rice, S. A.; Weichart, D.; Kjelleberg, S. *FEMS Microbiol. Ecol.* **1998***, 25*, 1– 10.

102. Fode-Vaughan, K. A.; Maki, J. S.; Benson, J. A.; Collins, M. L. P. *Lett. Appl. Microbiol.* **2003***, 37,* 239– 243.

103. Garcia-Armisen, T.; Servais, P. J. *Microbiol. Meth.* **2004***, 58,* 269– 279.

104. Rowan, N. J. Trends Food Sci. Technol. 2004, 15, 462– 467.

105. Gao, W.; Sattayasamitsathit, S.; Manesh, K. M.; Weihs, D.; Wang, J. *J. Am. Chem. Soc.* **2010***, 132,* 14403– 14405.

Chapter 4: Synthetic Nanomotors for Potential Drug Delivery Applications

4.1 Delivery of Drug Carriers by Catalytic Nanoshuttles

4.1.1 Delivery of Drug Carriers by Catalytic Nanoshuttles

Introduction

The development of new technologies is required to help deliver therapeutic and diagnostic agents to areas of the body that are now inaccessible to current systemic drug delivery techniques. To achieve not only active targeting but also precise guidance and control, future generation drug delivery vehicles may need to incorporate propulsion and navigation capabilities in order to deliver payloads to predetermined locations in the body. Nanoshuttles, precisely guided and controlled by a doctor, have the potential to transport therapeutic agents directly to diseased tissues, thereby improving the therapeutic efficacy and reducing systemic side effects of highly toxic drugs. Here chemically-powered catalytic nanoshuttles[1-3] are used to

demonstrate an initial proof-of-concept of using nanomotors to deliver biocompatible drug carriers in a propelled and targeted manner.

Many nanostructures have been constructed for drug delivery applications including polymeric nanoparticles, liposomes, polymersomes, dendrimers, nanoemulsions and their derivatives.[4,5] It has been demonstrated that these nanoscale drug carriers can improve the solubility of poorly water-soluble drugs, extend the drug systemic circulation lifetime, release drugs in a sustained and controllable way, and potentially deliver drugs in a targeted manner to minimize the likelihood of systemic toxicity. Such therapeutic particles are typically administered intravenously. By functionalizing the particle surface with tumor-specific targeting ligands, they can passively or selectively accumulate near tumors due to "enhanced permeability and retention" (EPR) effects or active targeting effects. However, off-targeting remains a key challenge of nanoparticle drug delivery. This is underlined by the fact that the majority of the intravenously administered therapeutic particles are distributed to normal tissues, which induces considerable adverse side effects. Another challenge of nanoparticle drug delivery includes the limited penetration depth of particles into the tumors.[6] Various strategies have been proposed to address these challenges by optimizing the physicochemical properties and biological functionalities of the drug carriers.[7] While significant progress has been made towards improving the therapeutic efficacy of drug-loaded nanoparticles, we envision self-powered nanomotors providing a new and unique approach to rapidly delivering drug carriers to predetermined destinations in a target-specific manner.

This initial study explores the ability of synthetic nanomotors to transport common drug carriers. The use of nanomotors to power nanomachines and nanofactories is one of the most exciting challenges facing nanotechnology today.[1-3] Recent experimental advances in the motion control and cargo-towing force of catalytic nanomotors,[1-3] combined with extensive theoretical analysis of nanomotor movements,[8-11] have made them attractive transport devices. Our group[12] and Sen's group[13,14] have previously demonstrated the ability of a nanowire motors to pick-up, transport and deliver polystyrene spherical cargo. The ability of using such catalytic nanoshuttles to transport nanostructured biomaterials and drug nanocarriers has recently been recognized as one of the next prospects for nanomotor development.[3] In the following sections, we will demonstrate that the catalytic nanoshuttles can readily pick-up drug-loaded poly-d,l-lactic-*co*-glycolic acid (PLGA) particles and liposomes and transport them over predefined routes towards predetermined target destinations. We will also examine the rate of transporting PLGA particles of different sizes and discuss factors influencing the high transport rates of drug carriers by the nanoshuttles, along with key challenges to their in vivo targeted drug delivery applications. While the concept of nanoshuttle drug-delivery transport is illustrated here using catalytic nanomotors, practical in vivo applications would require the use of fuel-free motors.

4.1.2 Delivery of Drug Carriers by Catalytic Nanoshuttles Experimental Methods

4.1.2.1 Purification of Multiwalled Carbon Nanotubes (CNT)

CNT purification was adapted from the previously reported procedure.[19] In brief, CNT (100 mg) obtained from NanoLab (Catalog No. PD30L5-20, Newton, MA), were dispersed in concentrated nitric acid (100 mL) and sonicated at 60 °C for 90 min. The solution was continued to incubate at 60 °C overnight. Following the acid treatment, nanopure water (4 L) was added to the CNT suspension. The diluted CNT suspension was allowed to settle overnight at room temperature. The supernatant was slowly decanted and the CNT suspension was centrifuged at 3000 rpm for 30 min to separate the CNT from the acid solution. The acid treated CNT were washed repeatedly with nanopure water (18.2 MΩ cm) until the solution pH was neutral. Finally, the purified CNT were dried at 60 °C and stored at room temperature. A Pt-CNT plating solution was sonicated for at least 2 h prior to use.

4.1.2.2 Synthesis and Characterization of Nanomotors

The nickel-containing catalytic nanomotors were prepared by electrodepositing the corresponding metals into a porous alumina membrane template (Catalog no. 6809-6022; Whatman, Maidstone, UK). Either carbon nanotube (Au/Ni/Au/PtCNT) or alloy ((Ni/(Ag_{50}/Au_{50})/Ni/Pt) nanomotors were used in these experiments. In both cases the length of each nanomotor segment was obtained by controlling the electrodeposition charge, while its diameter (~220 nm) was predetermined by the diameter of the membrane pores. A thin gold film was first sputtered on the branched

side of the membrane to serve as a working electrode. The membrane was assembled in a plating cell with aluminum foil serving as an electrical contact for the subsequent electrodeposition.

Magnetic carbon nanotube (Au/Ni/Au/PtCNT) nanomotors were developed by the following process.[19] In order to synthesize well-shaped cylindrical nanomotors, a sacrificial silver layer was electrodeposited into the branched area (~1–2 μm thickness) of the membrane using a silver plating solution (1025 RTU@4.5 Troy/Gallon; Technic Inc., Anaheim, CA) and a total charge of 2 C at −0.9 V (vs. Ag/AgCl, in connection to a Pt wire counter electrode). This was followed by an electrodeposition of gold (0.75 C) from a gold plating solution (Orotemp 24 RTU RACK; Technic Inc.) at −0.9 V (vs. Ag/AgCl). Subsequently, nickel was electrodeposited at −1.0 V (vs. Ag/AgCl) from a nickel plating solution [20 g L^{-1} $NiCl_2 \cdot 6H_2O$, 515 g L^{-1} $Ni(H_2NSO_3)_2 \cdot 4H_2O$, and 20 g L^{-1} H_3BO_3 (buffered to pH 3.4)] using a total charge of 2.0 C. The second gold segment (0.75 C) was then deposited, followed by the growth of a Pt-CNT segment. The Pt-CNT was galvanostatically deposited at −2 mA for 50 min from a platinum plating solution (Platinum RTP; Technic Inc.) containing CNT (0.50 mg mL^{-1}), mixed with Nafion (0.1 wt%) and 4-nitrobenzenediazonium tetrafluoroborate (2 mM). The sputtered gold layer and the silver layer were simultaneously removed by mechanical polishing using cotton tip applicators soaked with HNO_3 (35%) for ca. 5 min to ensure complete silver dissolution.

Magnetic alloy ((Ni/(Ag_{50}/Au_{50})/Ni/Pt) nanomotors were prepared by sequential electrodeposition of a pure platinum segment, followed by a nickel segment, the silver/gold (Ag/Au) alloy segment and a second nickel segment into the porous alumina membrane template. A sacrificial copper layer was first electrodeposited into the branched area of the membrane using a 1 M cupric sulfate pentahydrate solution ($CuSO_4 \cdot 5H_2O$; Sigma–Aldrich, St. Louis, MO), a total charge of 10 C at a potential of −1.0 V. Platinum was then deposited potentiostatically at −0.3 V for 2.8 C from a platinum plating solution (hexachloroplatinic acid, boric acid mixture) followed by electrodeposition of ferromagnetic Ni segment using the commercial nickel plating solution at −1.0 V for 1.8 C. Subsequently, a Ag/Au alloy segment was deposited at −1.1 V for 0.4 C using an equal mixture of the above plating solutions. One final nickel segment of 1 C was then plated at −1.0 V. The sputtered gold layer was removed by mechanical polishing using alumina powder (3 μm particle size) and the sacrificial copper layer was dissolved using $CuCl_2$ (0.5 M)–HCl (20%) mixture. In both cases, nanowires were released by immersing the membrane in NaOH (3 M) for 30 min. These nanowires were collected by centrifugation at 10,000 rpm for 5 min and washed repeatedly with nanopure water (18.2 MΩ cm) until a neutral pH was achieved.

4.1.2.3 Synthesis of Iron-Oxide Nanoparticles

The superparamagnetic iron oxide nanoparticles—used for the liposome transport—were synthesized by alkaline coprecipitation method described by Massart et al.[20] Briefly, $FeCl_2$ (1.0 mL, 2.0 M, in 2.0 M HCl) was mixed with $FeCl_3$ (4.0 mL, 1.0 M in 2.0 M HCl), followed by drop-wise addition of concentrated ammonium

hydroxide. The above mixture was vigorously stirred for 1 h under nitrogen atmosphere to yield black precipitate. The precipitate was washed by repeated magnetic decantation followed by vigorous stirring in distilled water. Boiling ferric nitrate (1.3 mol in 0.8 M HNO_3) was added to the above precipitate to oxidize magnetite to maghemite nanoparticles. After oxidation, the iron-oxide nanoparticles were magnetically decanted and additionally stirred in nitric acid (0.8 M) for 10 min. These nanoparticles were finally stabilized by adding sodium citrate (0.25 M) and held at 80 °C for 30 min, followed by precipitation in acetone at room temperature. Subsequently, a final magnetic decantation was performed to redisperse the particles in water. The size of the particles was analyzed using dynamic light scattering and found to have mean value of 15 nm.

4.1.2.4 Preparation of Drug-Loaded PLGA Microparticles

Doxorubicin-loaded magnetic PLGA microparticles were prepared using an oil-in-water emulsion method.[21] Briefly, an excess of triethylamine was added to an aqueous solution of doxorubicin hydrochloride (Sigma-Aldrich) in order to neutralize the hydrochloride ion. The resulting free-base doxorubicin was extracted from the aqueous solution with dichloromethane. The extraction was performed three times to improve yield. The collected free-base doxorubicin was dried under argon and dissolved in chloroform at 1 mg mL^{-1}. Meanwhile, PLGA-ester (10 mg, 30 mg mL^{-1}, 50:50 lactic acid: glycolic acid, IV 0.82 dL g^{-1} from Lactel, Pelham, AL) were dissolved in chloroform. Oleic-acid coated 10 nm Fe_3O_4 nanoparticles in chloroform (150 μL, 16.7 mg mL^{-1}), received from OceanNanoTech; Fayetteville, AR) was added

to the PLGA solution. To complete the oil phase of the oil-in-water emulsion, doxorubicin solution (100 μL in chloroform) was added to the PLGA–Fe_3O_4 solution and the mixture was vortexed for complete mixing. The chloroform oil phase was then added dropwise to a water phase consisting of an aqueous solution of polyvinyl alcohol (1.5 mL, 6%, molecular weight: MW 85 000, 80% hydrolyzed, Sigma-Aldrich). The polyvinyl alcohol serves as an emulsifying agent to stabilize the oil phase in the water. The mixture was then vortexed at high speed for 3 min to create an emulsion. The emulsion was sonicated in a bath sonicator for 1 min to produce a more uniform emulsion, followed by gently stirring overnight with the lid off to allow the chloroform to evaporate. Finally, the solution was washed 3 times with a centrifuge filter (Amicon, 100 kDa MW cut-off (MWCO)) and resuspended with water (4 mL) after the first two washes and 1 mL of water after the final wash. PLGA particles were separated using a variety of filter membranes to obtain desired particle size fractionation.

4.1.2.5 Preparation of Magnetic Liposomes

Magnetic liposomes were prepared using the reverse phase evaporation method.[22] In brief, a diethyl ether solution (3 mL) containing egg phosphatidylcholine (1 mg; ePC) and cholesterol (1 mg; CHOL) (both from Avanti Polar Lipids, Alabaster AL), was prepared and then added to NaCl solution (1 mL, 0.9%) containing Fe_3O_4 nanoparticles (10 mg) which were prepared in accordance to procedure described above. This mixing resulted in a two-phase mixture which was then emulsified in a bath sonicator until the organic solvent was evaporated and the mixture became one-

phase dispersion. The magnetic liposomes and non-incorporated magnetite particles were separated using a desalting column (Thermo Scientific, Rockford, IL) and were magnetically collected/washed using a Neodymium (NdFeB) magnet (1.32 Tesla from K&J Magnetics Inc., Jamison, PA).

4.1.2.6 Visualization of Particle Transport of PLGA

Initially, the concentrated nanomotor (1 mL) suspension in nanopure water diluted (with nanopure water) using a 1:100 volume ratio. The diluted nanomotor suspension (10 μL) were then mixed with the magnetic particle carrier (10 μL) and hydrogen peroxide fuel solution (10 μL, 15 wt%). The solution was then transferred to a pre-cleaned glass microslide (25 × 75 mm, 1.0 mm thickness; VWR International) and placed on the microscope stage. A 10 mm cube-shaped Neodymium (NdFeB) magnet (1.32 Tesla from K&J Magnetics Inc., Jamison, PA, USA) was placed at 2 cm away from the glass microslide. The nanomotor was magnetically directed toward an unbound magnetic liposome or PLGA particle, captured and transported it for 5 s via magnetic steering. The translocation of a magnetic liposome or PLGA particle by a catalytic nanomotor was observed and recorded using light transmission microscopy at 400X total magnification (Nikon Instrument Inc., Eclipse80i, Melville, NY), equipped with a Nikon HQ^2 CoolSNAP camera (Roper Scientific, Duluth, GA) and MetaMorph 7 software (Molecular Devices, Sunnyvale, CA). Movies were acquired over 30 s at a frame rate of 10 frames s^{-1}. The speed of the nanomotors was measured using MetaMorph 7's tracking software, which determined the position of the nanomotor in each frame, calculated the displacement distances between the frames, resulting in the

average velocity of each nanomotor. The average nanomotor speed (n = 50) before the particle pick-up was found to be 16 μm s^{-1} (range of 14–18 μm s^{-1}). For experiments involving a size-dependent pick-up, data were normalized to the average nanomotor speed to clearly depict the impact of the particle pick-up as a decreased nanomotor speed rather than a simple percent decrease. For SEM images, alloy nanomotors were incubated with a diluted suspension of fractionated PLGA particles for 30 min and imaged using a Phillips XL30 ESEM instrument.

4.1.2.7 Preparation of the PDMS Microchannel Channels

Microchannel structures were prepared using the soft lithography of PDMS in a previously described procedure.[12] In brief, masks were produced on transparent sheets using a high resolution printing system (CadArt Services Bandon, Or). SU-8 25(negative photoresist) patterned on a 4" silicon wafer served as the master for soft lithography. PDMS (Dow Corning Corporation, Midland, MI) was mixed by hand in a 10:1 polymer: fixing agent ratio. PDMS was poured over the silicon master, degassed in a vacuum dessicator, and baked at 110 °C for 15 min. The resultant structures were exposed to UVO ozone (Jetline Co., Irvine, CA) at a gas flow rate of 3 sccm for 5 min. The PDMS network had channels of 35 μm wide and 25 μm tall with channel lengths of approximately 600 μm, leading into wells with 200 μm openings and a 1 mm overall diameter at a slope of 5% to minimize hydrostatic pressure. Holes of 600 μm were punched in each well using a steal rod (Technical innovations, Brazoria, TX). The microchannels were filled using a 20-gauge needle before use with 0.3 M NaOH

for 30 min. The PDMS microchannels were then flushed with 3 mL of ultra pure water to insure the removal of any residual NaOH.

4.1.2.8 Nanomotor Experiments in PDMS Microchannels

The nanomotor suspension in nanopure water was first diluted to obtain a concentration (2.6×10^6 nanomotors mL^{-1}) suitable for filling the PDMS channel ~2.6×10^6 nanomotors mL^{-1}. The diluted nanomotor suspension (100 μL) were then mixed with the hydrogen peroxide (100 μL, 15 wt%) and diluted with solution of the magnetic liposome or drug-loaded PLGA, thus resulting in a 5 wt% H_2O_2 fuel solution. The final solution was then transferred to the PDMS microstructure using a 1 mL syringe and 20 μm gauge needle. Nanomotors, liposomes and PLGA particles in the PDMS chamber were visualized by using an inverted microscope and using a Nikon HQ^2 Coolsnap camera. Fluorescence images were acquired using an X-Cite-120 light source and Nikon G-2E/C Rhodamine filter cube. Ambient light and digital adjustments to brightness and contrast were used to visualize the fluorescent PLGA, nanomotor and PDMS channel at the same time. Tracking, magnetic guidance and visualization techniques are the same as described above.

4.1.2.9 Theoretical Calculations

The hydrodynamic drag balancing the propulsive force on the moving nanorod is approximated by Stoke's drag law for a cylinder as shown in Equation 1,

$$\mathbf{F}_{drag} = \frac{2\pi\mu L}{\ln\left(\frac{2L}{R}\right) - 0.72}\mathbf{v}$$

(1)

where μ is viscosity, v is velocity, L & R are the length and radius of the moving nanorod.

The force of the alloy nanomotor was calculated to be 0.09 pN using the fluid viscosity of 1.0144×10^{-3} kg s-1 m-1 and an average nanomotor velocity of 16 μm s-1 into the above equation. Using the calculated nanomotor drag force and assuming the radius of the nanomotor is negligible compared to the particle, we estimated the theoretical velocity of the nanomotor-particle doublet by the Stokes law for particle drag force, Equation (2).

$$\mathbf{v} = \frac{\mathbf{F}}{6\pi\mu r}$$

(2)

The velocities were calculated for particles of different size and used to predict the transport time to cover the distance of 100 μm. This distance symbolizes how far the drug- loaded particle has to travel from the blood vessel to the nearest tumor cell. In comparison a similar transport time was calculated for an unassisted particle diffusing under Brownian motion using the diffusion constant derived from the Einstein-Stokes equation, Equation (3).

$$D = \frac{kT}{6\pi\mu r}$$

(3)

After obtaining the diffusion constant we solved for time from the below random walk theory equation (Equation 4) assuming 1 dimension diffusion over a 100 μm distance.

$$x^2 = 2Dt \quad (4)$$

The resulting time tb was compared to the transport time using the nanomotor assisted particle transport time tnm. The resulting predicted ratio tb/tnm revealed a particle size independent 1000 fold increase for the random walk time to travel the same 100 μm.

These predicted results were compared to our actual nanomotor assisted average particle transport times. The calculated results shown in the below Table 4.1 reveal that the nanomotors transport of the particles is very consistent with their theoretical Stokes values. Such results may suggest that these nanomotors are a very efficient method for particle transport.

Table 4.1 Table portrays the predicted and experimental time increase between nanomotor driven and faster diffusion driven particle transportation assuming that particles diffuse in one direction.

Particle radius, μm	[a]Predicted velocity, μm s^{-1}	[b]Predicted t_B/t_{NM}	Experimental velocity, μm s^{-1}	[b]Calculated t_B/t_{NM}
0.325	14.4	1009	13.69	1033
0.650	7.21	1005	9.7	1408
1.1	4.34	1008	5.8	1448

a – nanomotor assisted predicted velocity using Stoke's equation
b – ratio of transport time was calculated assuming a 100 μm separation distance between a hypothetical blood vessel and tumor cell
t_B is calculated using random-walk theory of 1-D diffusion, $x^2 = 2Dt$
t_{NM} is calculated from predicted and experimental nanomotor velocity

4.1.3 Delivery of Drug Carriers by Catalytic Nanoshuttles

Results and Discussion

4.1.3.1 Transport and Release of PLGA Particles

Drug-loaded PLGA particles, containing small magnetic iron oxide nanoparticles, were synthesized and applied as cargo to the nanowire motors. Figure 4.1.1 illustrates the scheme of the pick-up, transport and release of drug-loaded PLGA microparticles by synthetic nanomotors. Figure 4.1.1B shows actual optical images highlighting the directed motion of our catalytic alloy nanomotor towards a PLGA particle followed by an instantaneous loading of the polymeric particle onto the nanomotor via the weak magnetic attraction between the nanomotor's nickel segment and the iron oxide-encapsulated 1.6 μm diameter PLGA particle. Similar to the scheme of Figure 4.1.1A, these images demonstrate the dynamic processes of pick-up (a), transport (b), and release (c) of the "heavy" polymeric particle using magnetically-guided nanomotor. The nanomotor travels at a slower speed of 9 μm s^{-1} when bearing the PLGA particle, and it regains its initial faster speed (16 μm s^{-1}) after releasing the particle. The instantaneous release of the particle cargo is attributed to the fast reversal in the direction of the nanomotor, during which the drag force imposed on the particle overcomes the magnetic attraction between the particle and the nanomotor. These data (and results obtained through this study) suggest that the iron oxide-loaded polymeric particles and the size of the nickel segment within the nanomotors are sufficient for enabling the pick-up of particles but not overwhelming to prevent their release.

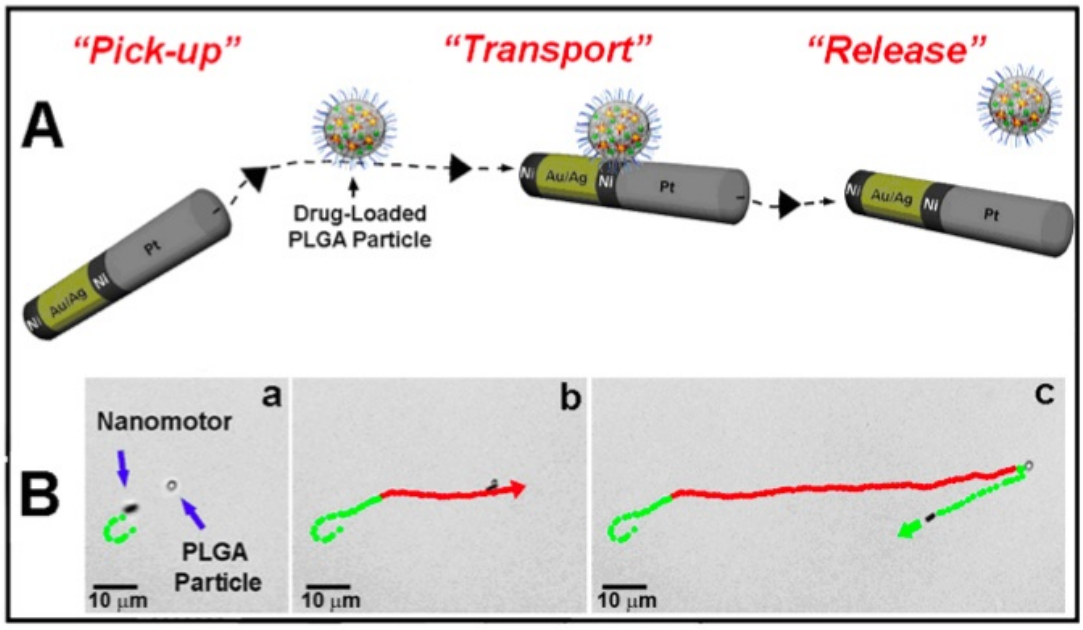

Figure 4.1.1 Translocation of model drug carriers by catalytic nanowire motors. A) Scheme depicting the dynamic pick-up, transport, and release of drug-loaded PLGA particles using a nanoshuttle. B) Sequential optical microscopy images of an en-route PLGA particle pick-up and transport by an alloy (Ni/(Au_{50}/Ag_{50})/Ni/Pt) nanomotor. Dark (broken) and grey (solid) tracked lines represent the path traveled by the nanomotor and the cargo-loaded nanomotor, respectively. Image B (a) shows the magnetically guided movement of the nanomotor towards the magnetic cargo, while (b) and (c) respectively, display the dynamic pick-up, transport, and subsequent release of the PLGA particle by the nanomotor in a 5 wt% hydrogen peroxide medium.

4.1.3.2 Size Dependent Transport of PLGA Particles

The slower speed during the particle transport is expected from Stoke's law, which states that the drag force opposing the velocity of an object in a fluid is directly influenced by the diameter of that object. Accordingly, we next examined the influence of the particle size upon the transport rate of the drug-loaded PLGA particles by the catalytic nanomotors. The scanning electron microscopy (SEM) images (not shown) illustrate the ability of the nanomotors to attract different sized PLGA particles [a) 2.5, b) 1.5, and c) 0.75 μm] to their Ni segment. Experiments were carried out by allowing the nanomotors to freely move around and interact with polymeric particles

for 30 min before drying the samples for SEM imaging. Various sized particles were synthesized by altering the sonication time during the emulsion process. Particles were further separated into a more confined size range through a series of size filtration steps. SEM imaging revealed that most nanomotors can capture at least one particle. As expected with ferromagnetic materials, in few cases, grouping of several nanomotors and particles was also observed. PLGA particles themselves were typically not found to attract each other, except when concentrated and condensed in the dried sample. For particle sizes smaller than 500 nm, the nanomotor has the ability to pick-up multiple particles; however these nanoscale particles are invisible due to optical limitations (not shown).

The pick-up and delivery of polymeric particles of different sizes and the corresponding nanomotor motion trajectories can be used to calculate the transport rates of such drug-loaded polymeric particles Figure 4.1.2. The straight-line images of Figure 4.1.2A visually depict the effect of the PLGA particle size on the transport rate using catalytic nanomotors. The ferromagnetic Ni segment allows for such straight-line magnetic alignment. As predicted by the Stoke's law, these images show a steady decrease of the nanomotor speed upon increasing the particle size (a-c). For example, a nanomotor carrying particles of 2.0, 1.3, and 0.8 μm size traveled distances of 31.5, 48.5, and 67.5 μm, respectively, over a 5 s period. Supporting Video 4.1 clearly illustrates such rapid transport of the varying sized PLGA particles. This video demonstrates that a single nanomotor—originally moving at 16 μm s^{-1}—travels at slower speeds of 6.3, 9.7, and 13.5 μm s^{-1} upon carrying the 2.0, 1.3 and 0.8 μm

particles, respectively. These nanomotor transport speeds are representative of other nanomotors traveling with similar sized particles. The histogram representation of Figure 4.1.2B shows the average transport rate (and the corresponding standard deviation) of varying sized PLGA particles calculated from 10 or more nanomotors. An average decrease of the speed (after the pick-up) of 61%, 39%, and 14% is thus observed for the big, medium, and small particles, respectively.

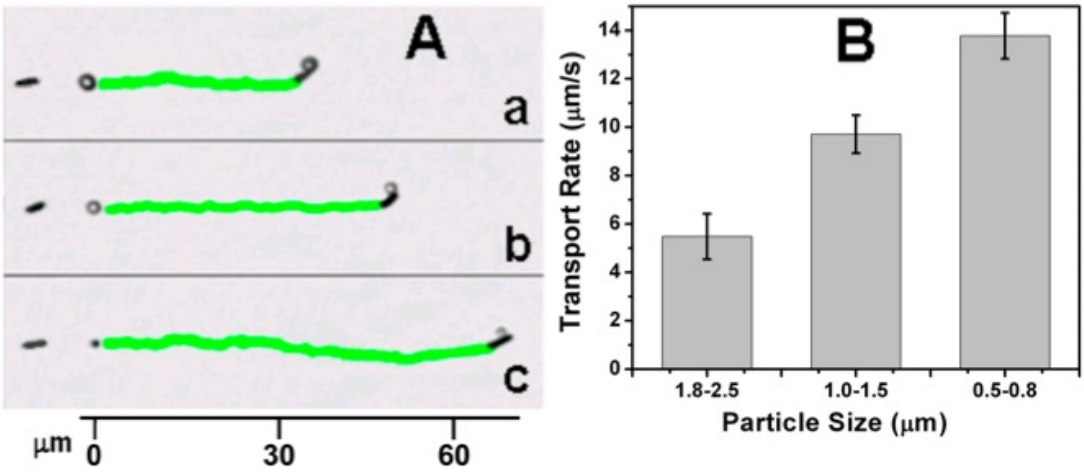

Figure 4.1.2 PLGA particle transport rate. Ability of synthetic (Ni/(Au_{50}/Ag_{50} alloy)/Ni/Pt) nanomotors to pick-up and transport drug-carrying PLGA particles of varying sizes. A) Optical images, superimposed with tracked lines, comparing the displacement of a catalytic nanomotor during the 5 s transport of different sized particles: a) 2.0 μm, b) 1.3 μm, c) 0.8 μm. Sizes below about 400 nm cannot be visually seen and subsequently transported. B) Corresponding column graph statistically depicts changes in the motor speed as a function of the transported particle size. Transport rates were calculated using at least 10 nanomotors after pick-up whose initial speed was normalized to 16 μm s^{-1} (the average nanomotor speed which have a range of 14–18 μm s^{-1}).

The overall rapid transport of polymeric particles delivered by nanoshuttles can be advantageous for the drug carriers to reach deep tumor tissues, compared with common nanoparticle drug delivery whose penetration depth mainly depends on Brownian motion once the particles are in the tumor interstitium. The strong

propelling force provided by the nanoshuttles can potentially facilitate the tissue penetration of drug carriers.[6,15] From the Stoke's equation for a rod, a force of 0.09 pN can be estimated for our nanomotor traveling at 16 μm s^{-1} in 5% H_2O_2 (see Methods). Assuming the distance between a tumor cell to its nearest blood vessel is 100 μm, the theoretical average transport time of the large, medium and small PLGA particles over such distance would be 17.3, 10.3, 7.3 s according to Figure 4.1.2B. Such times are (on average) 1300 times faster than those expected by random Brownian diffusion, calculated from the Einstein-Stokes equation for particles of 2.15, 1.25, 0.65 μm diameter (i.e., the average size for large, medium, small particles found in Figure 4.1.2B). Such results are in-line with the predicted size-independent, 1000 fold increase in transport rate (See Methods detailed calculations). We observed that the smaller particle transport rates were in good agreement with Stoke's law while small deviations were observed for larger particles. These discrepancies may be attributed to the complex interplay of fluid dynamics of the nanomotor-particle pair or due to a possible over-estimation of the particle size by the distortion under an optical microscope. It is important to note that the calculated Brownian transport times refer only to the time it takes for particles to travel a distance of 100 μm. Due to the randomness of Brownian diffusion either a high multitude of these particles or the use of a director device such as a nanomotor would be necessary to ensure that drug-loaded particles arrive at their desired destination.

4.1.3.3 Directed Transport of Drug-Loaded PLGA Particles

Next we demonstrated the ability of the nanomotors to transport drug-loaded polymeric particles through a microchannel network. Microfluidic dexterity is illustrated by the PLGA particle pick-up, transport, and release by a nanomotor in a polydimethylsiloxane (PDMS) microchannel network. The PDMS channel acts as a tool for creating experimental uniformity and reproducibility. With the PDMS channel, movement and dexterity of the nanomotors carrying PLGA particles through predetermined paths can be illustrated. While the paths provide a challenge of navigation for the nanoshuttles, they also provide an illustration of the applicability of the nanoshuttles in different environments. Doxorubicin was selected as a model anticancer drug in this study because of its self-fluorescence property, which allows for the visualization of the PLGA particles using fluorescence microscopy. Specifications that need to be addressed in a microfluidic channel are different from those involved in the nanomotor/drug-carrier interaction outside the channel. For instance, the surface chemistry of the microfluidic channels can affect the performance of the nanomotors. Also, hydrostatic pressure gradients need to be avoided by maintaining equal volumes in each well. Such difference between bulk-flow transport and that of a nanomotor-based microchannel transport is evident when conducting experiments.

4.1.3.4 Directed Transport of Liposomes

In addition to the rapid delivery of polymeric (PLGA) particles, we examined the ability of our catalytic nanomotors to pick-up and transport liposomes. Liposomes

are attractive drug carriers that can carry both hydrophilic and lipophilic therapeutic agents.[18] Liposome transport offers some advantages including on-demand drug release after the mechanical or chemical breaking of the liposome. Here we show the ability of alloy and CNT-based nanomotors to pick up iron oxide-encapsulated liposomes. Figure 4.1.3 demonstrates the dynamic processes of pick-up (a, b) and transport (c,d) of a 4.3 μm liposome by the CNT-based motor. The transport rate of the nanomotor carrying a liposome is about 4 μm/s. Yet, the nanomotor regains its initial speed upon releasing the liposome. In comparison to the PLGA particles, the liposome transport is relatively slower due to its large size. As illustrated in Figure 4.1.3B, the nanomotor is able to pick up a drug-loaded liposome on one side of a microfluidic channel, transport it across the channel, and release it into the opposite microwell. The images of Figure 4.1.3B(b–d) were captured at low magnification to illustrate both the liposome transport process by the alloy nanomotor and the configuration of the PDMS channel. The liposome is carried by a nanomotor and transported through a 2-mm-long channel within 2 min. It is unlikely that such a large particle could reach its destination through such a long channel via random diffusion without external directed motion. Supporting our theoretical results, we only observed Brownian motion and did not see any particles displaced over significant distances even after several hours of observation. This enabled us to selectively target and pick-up drug-loaded particles with relative ease.

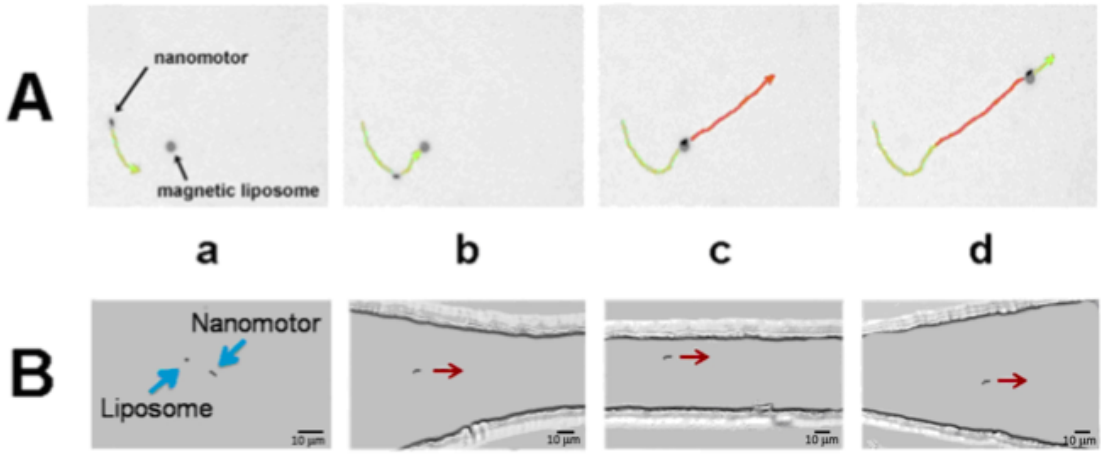

Figure 4.1.3 Transport of magnetic liposome vesicle. Image (A) shows an en-route of liposome pick-up and transport by a Au/Ni/Au/Pt-CNT nanomotor. Black and grey tracked lines represent the path traveled by the nanomotor and the cargo-loaded nanomotor, respectively. Images (a) and (b) show the magnetically guided movement of the nanomotor towards the magnetic cargo, while (c) and (d) display the dynamic pick-up and subsequent transport of the liposome by the nanomotor. B) Use of the catalytic nanoshuttle for transporting the magnetic liposome through a PDMS microchannel. Optical microscopy images depicting the pick-up (a) and subsequent transport of a liposome across a PDMS microfluidic channel (entering (b), inside (c), exiting (d)) by an alloy (Ni/(Au_{50}/Ag_{50})/Ni/Pt nanomotor. Experiments performed in 5wt% hydrogen peroxide fuel.

4.1.4 Delivery of Drug Carriers by Catalytic Nanoshuttles

Conclusions

In conclusion, we have demonstrated an initial proof-of-concept of directed delivery of common polymeric and liposomal drug carriers using catalytic nanomotors. The nanomotors can pick-up, transport, and release varying sized drug carriers from a loading zone to a predetermined destination through a predefined route. The transport of the drug carriers delivered by a nanomotor is directionally guided, with a rate more than three orders of magnitude faster than that expected from Brownian motion. We envision that such self-powered nanomotors may provide a new and unique approach for rapidly delivering drug carriers to their destination in a target-specific manner.

While key challenges remain prior to applying these nanomotors for in vivo targeted drug delivery, this work advances one step closer to a futuristic nanomachine suitable for systemic medical applications. We are currently exploring several aspects to improve the nanomotor drug delivery in the future. Our groups are currently developing a new generation of magnetically driven (fuel-free) nanomotors for future in vivo applications. Other recently developed fuel-free nanomotors based on an artificial flagella design[16,17] could also be used for such targeted-drug delivery. In order to improve the efficiency of nanomotor drug delivery, we are also exploring the attachment of drug carriers to nanomotors through chemical or biological linkers that are sensitive to the tumor microenvironment (e.g., enzyme and acidity) to enable on-demand release of the carrier. Such a mechanism will allow for a more accurate delivery to the target site, and help overcome the inherit limitation of using a magnetic field for delivering drug-loaded particles. Lastly, the removal of nanomotors from the body after completing the mission needs further consideration.

4.2 Delivery of Drug Carriers by Magnetic Nanoshuttles

4.2.1 Potential Drug Delivery by Magnetic Nanomotors

Introduction

The proper understanding and execution of nanomotor biological functionality, i.e., pick-up, transport, and delivery of biologically relevant nanostructured loads,[2,3,12-14, 23-26] is crucial for myriad future biomedical applications including drug delivery and gene therapy. Past work from both Sen's group and our team has previously demonstrated the ability of catalytic nanowire motors to pick up, tow, and release spherical polystyrene particles.[12,13] Our group has also recently demonstrated the guided transport of drug-loaded liposomes,[23] pancreatic cancer cells,[27] and nucleic acids[28] by fuel- driven nanomotors. Despite these advances in cargo-towing by catalytic nanomotors, future ex-vivo and in-vivo biomedical transport applications require the use of biocompatible, fuel-free nanomotors.

In this work, we describe the efficient cargo-towing capabilities of magnetically driven (fuel-free) nanomotors, elucidate the fundamental mechanism of cargo-towing by these flexible nanoswimmers, and assess to what extent they can be used to transport relevant cargo in biological media. Magnetically driven nanomotors, which swim under externally applied magnetic fields, are particularly promising for use in a variety of biomedical applications,[26,29,30] as they can perform complex manoeuvres while obviating fuel requirements. To examine the directed transport of

payloads by these fuel-free magnetic swimmers, we rely here on our recently developed flexible nanowire motors that are prepared by a templated electrodeposition approach.[30-32] These two- or three-segment, flexible nanowire motors consist of a rotating magnetic nickel head (≈1.5 μm long), along with a flexible silver segment (≈4 μm long). These swimmers appear to be among the fastest fuel-free synthetic nanomotors reported to date in terms of dimensionless swimming speed (obtained by dividing the dimensional speed, by the body length, and the actuation frequency, to scale off the effects of motor size and frequency), allowing them to propel efficiently in biological fluids.[32] Despite the great potential for these magnetically propelled nanoswimmers in diverse biomedical applications, their ability to carry a cargo has not yet been demonstrated.

In order to elucidate the fundamental mechanisms of cargo-towing by flexible magnetic nanomotors, we examine the transport of various-sized, drug-loaded magnetic polymeric microspheres made of pol(D,L-lactic-*co*–glycolic acid) (PLGA). We investigate their towing performance and discuss the hydrodynamic features of these cargo-loaded motors. The effect of the iron oxide-loaded cargo size upon the swimming performance is evaluated experimentally and compared to a theoretical model, emphasizing the interplay between hydrodynamic drag forces and boundary actuation. The performance of these new fuel-free nanowire motors makes them attractive for future biomedical applications, as illustrated below for the directed delivery of drug-loaded microparticles to HeLa cells in cell-culture media. Our investigations will ultimately enable us to address the performance and physical

limitations of nanomotor towing for the efficient transport of biological and therapeutic payloads.

4.2.2 Potential Targeted Drug Delivery by Magnetic Nanomotors

Experimental Methods

4.2.2.1 Reagents and Solutions

Cupric sulfate pentahydrate, nickel(II) chloride hexahydrate, nickel(II) sulfamate tetrahydrate, gold (Orotemp 24 RTU RACK) and silver (1025 RTU @ 4.5 Troy/gallon) plating solutions were purchased from Technic Inc., Anaheim, CA. All chemicals used were of analytical-grade reagents, and deionized water was obtained from a Millipore Milli-Q purification system (18.2 MΩ cm). For the preparation of the drug-loaded magnetic PLGA microparticles, doxorubicin hydrochloride (Sigma-Aldrich), triethylamine (Sigma-Aldrich), dichloromethane (Sigma-Aldrich), PLGA-ester (50:50 lactic acid: glycolic acid, IV 0.82 dL g^{-1} from Lactel, Pelham, AL), oleic acid-coated 10 nm Fe_3O_4 nanoparticles (OceanNanoTech; Fayetteville, AR), polyvinyl alcohol (PVA, MW 85000, 80% hydrolyzed, Sigma-Aldrich) and centrifuge filters (Amicon, 100 kDa MW cut-off (MWCO)) were used. Standard White Polycarbonate 'Track Etch' Membrane Filters from SPI-Pore were used to obtain different size of microparticles. A commercial Sylgard 184 Silicone elastomer kit (Dow Corning Corporation, Midland, MI) was used for the preparation of the PDMS channel (see below).

For the HeLa cell-culture RPMI (Roswell Park Memorial Institute) medium, fetal calf serum, penicillin, streptomycin, and trypsin, all purchased from Life Technologies (Carlsbad, CA), were used.

4.2.2.2 Apparatus

Template electrochemical deposition of nanowires was carried out with a CHI 660D potentiostat (CH Instruments, Austin, TX). An inverted optical microscope (Nikon Instrument Inc. Ti-S/L100), coupled with a 40× objective, a Photometrics QuantEM 512/SC camera (Roper Scientific, Duluth, GA) and a MetaMorph 7.6 software (Molecular Devices, Sunnyvale, CA) were used for capturing movies. The images for Figure 4.2.1 was captured using a Hamamatsu digital camera C11440, 40× objective and was acquired at the frame rate of 100 fps using the NIS-Elements AR 3.2 software.

4.2.2.3 Synthesis of Flexible Ni–Ag_{flex} Magnetic Nanowires

The nanowire motors were prepared using a common template-directed electrodeposition protocol.[30-32] A silver film was first sputtered on one side of the porous alumina membrane template containing 200 nm-diameter cylindrical pores (Catalog No 6809-6022; Whatman, Maidstone, UK) to serve as a working electrode. The membrane was then assembled in a plating cell with an aluminum foil serving as a contact for the sputtered silver. Copper was electrodeposited in the 'branch' area of the membrane from a $CuSO_4 \cdot 5H_2O$ (1 M) solution, using a charge of 8 C and a potential of -0.9 V (versus an Ag/AgCl reference electrode, along with a Pt wire counter electrode); subsequently, gold was plated next from the commercial gold

plating solution at -0.9 V (versus Ag/AgCl), using a charge of 0.5 C, which was used for protecting the nickel while dissolving the membrane later; nickel was deposited from a nickel-plating solution containing $NiCl_2 \cdot 6H_2O$ (20 g L^{-1}), $Ni(H_2NSO_3)_2 \cdot 4H_2O$ (515 g L^{-1}), and H_3BO_3 (20 g L^{-1}) at -1.0 V (versus Ag/AgCl) for 6 C; finally, silver was plated at -0.9 V (versus Ag/AgCl) for a total charge of 4.5 C using a commercial silver-plating solution. The sputtered silver layer was mechanically removed from the membrane by polishing with alumina particles (3–4 μm); the sacrificial copper layer was dissolved using a 20% HCl solution containing 0.5 M $CuCl_2$. The membrane was then dissolved in a NaOH (3 M) solution for 30 min to completely release the nanowires. The nanowires were collected by centrifugation at 6000 rpm for 5 min and were washed repeatedly with nanopure water (18.2 MΩ cm) until a neutral pH was achieved. All nanowire solutions were stored in nanopure water at room temperature. Flexibility of the silver segment was achieved by its partial dissolution accomplished by mixing the diluted Ni–Ag nanowire solution (10 μL) with the hydrogen peroxide solution (10% (w/v), 10 μL) for 1 min. The nanowires were then washed on the glass slides using nanopure water (18.2 MΩ cm) until a neutral pH was achieved. The resulting nanomotors had a single rigid 1.5 μm-long Ni segment, a 4 μm-long flexible silver segment and a 0.3 μm-long gold segment (for protecting the Ni), giving a total nanowire length of 5.8 μm.

4.2.2.4 Preparation of the Drug-Loaded PLGA Microparticles

Doxorubicin-loaded magnetic PLGA microparticles were prepared using an oil-in-water emulsion method.[21] Briefly, an excess of triethylamine was added to an

aqueous solution of doxorubicin hydrochloride in order to neutralize the hydrochloride ion. The resulting free-base doxorubicin was extracted from the aqueous solution with dichloromethane. The extraction was performed three times to improve yield. The collected free-base doxorubicin was dried under argon and dissolved in chloroform at 1 mg mL^{-1}. Meanwhile, PLGA–ester (10 mg, 30 mg mL^{-1}, 50:50 lactic acid: glycolic acid, IV 0.82 dL g^{-1} from Lactel, Pelham, AL) were dissolved in chloroform. 400 μL of the oleic acid-coated 10 nm Fe_3O_4 nanoparticles suspension in chloroform (16.7 mg mL^{-1}) were added to the PLGA solution. To complete the oil phase of the oil-in-water emulsion, a doxorubicin solution (100 μL) was added to the PLGA–Fe_3O_4 suspension and the mixture was vortexed for complete mixing. The chloroform oil phase was then added dropwise to a water phase consisting of an aqueous solution of PVA (1.5 mL, 2% (w/v)). The PVA serves as an emulsifying agent to stabilize the oil phase in the water. The mixture was then vortexed at high speed for 3 min to create an emulsion. The emulsion was sonicated in a bath sonicator (Fisher Scientific FS30D) for 6 min to produce a more uniform emulsion, followed by gently stirring overnight with the lid off to allow the chloroform to evaporate. Finally, the solution was washed 3 times with a 100 kDa MW cut-off centrifuge filter and resuspended with water (4 mL) after the first two washes and 1 mL of water after the final wash. PLGA particles were separated using the appropriate variety of filter membranes to obtain the desired particle size fractionation.

4.2.2.5 PDMS Channels Preparation

Polydimethylsiloxane (PDMS) was hand-mixed in a 10:1 polymer:fixing agent ratio using the commercial Sylgard 184 Silicone elastomer kit. PDMS was poured over a glass Petri dish, degassed in a vacuum desiccator, and baked at 110 °C for 15 min. Holes of ≈2 mm were punched in each well using a puncher (Ted Pella, Redding, CA). An open channel of ≈200 μm wide and ≈10 mm in length was used to properly visualize the magnetic nanowire motors. The resultant structures and cleaned glass slides were exposed to UVO ozone (Jetline Co., Irvine, CA) at a gas flow rate of 3 sccm for 5 min, pressed together and baked for another 10 min at 110 °C to complete the bonding process. The PDMS channel was washed with ultra pure water to ensure the removal of any residual dust and dried properly under nitrogen before starting the experiments. Ambient light and digital adjustments to brightness and contrast were used to visualize the magnetic nanowires with the cargo and the PDMS channel at the same time.

4.2.2.6 Magnetically Driven Movement

The magnetic field was achieved by a triaxial Helmholtz coil, consisting of a homogeneous rotating magnetic field and a constant magnetic field which is perpendicular to the axis of the rotating one. The magnetic induction was measured using a Gaussmeter (Model 475 DSP Gaussmeter, Lake Shore Cryotronics, Inc, Westerville, OH). The magnetic nanomotors were driven by a magnetic field with an unsteady component of amplitude H_1, rotating sinusoidally in a plane perpendicular to

a constant component, H_0. The magnetic field precessed about the direction of the constant magnetic field at an angular frequency $\Omega = 2\pi f$.

4.2.2.7 Cell Line and Culture

HeLa cells were cultured in a flask in RPMI medium supplemented with 10% fetal calf serum, penicillin (100 μg mL^{-1}), and streptomycin (100 μg mL^{-1}). The HeLa cells were incubated with 5% CO_2 at 37 °C until 80% confluent. The cells were treated with trypsin and centrifuged at 1000 rpm for 10 min to form a pellet. The cells were resuspended in fresh RPMI medium and counted with a hemacytometer in order to determine the cell concentration per mL. The cells were seeded in the PDMS wells attached to slide coverslips at approximately 10^4 cells cm^{-2}. The PDMS coverslips were placed inside a 100 mm cell-culture dish and an additional coverslip was placed over the PDMS well to prevent evaporation. The cells were allowed to incubate overnight and were used in subsequent experiments.

4.2.2.8 Experiments in PDMS Channels

Ni–Ag_{flex} magnetic nanowires were repeatedly washed (10 times) with culture media to remove the remaining peroxide residue. Then the PDMS channel was filled with culture media (500 μL) and an appropriate volume of the washed flexible Ni–Ag_{flex} magnetic nanowire suspension and the drug-loaded magnetic PLGA microparticles (≈10 μL of each) was added to the magnetic microparticles capture well. After capturing the magnetic microparticles, the flexible nanowires were magnetically guided across the channel to the target cells reservoir. HeLa cells were plated 24 h earlier in the corresponding reservoir selected for a stationary delivery.

4.2.3 Potential Targeted Drug Delivery by Magnetic Nanomotors

Results and Discussion

4.2.3.1 Cargo-Towing Magnetic Nanowire Motors

Figure 4.2.1 shows a sequence of pictures, taken at 20 ms intervals, of the motion of a magnetic nanowire motor carrying a ≈1.0 μm drug-loaded magnetic PLGA microsphere under a rotating magnetic field (the magnetic moment of the microsphere arises due to the encapsulation of iron oxide nanoparticles. These display the entire movement of the sphere-loaded flexible nanoswimmer. The motor rotates around the cargo (the particle is loaded inside the cone swept by the nickel), which is further shown by the disappearance of the particle during each rotation cycle. The location of the magnetic cargo towards the free end of the nickel segment also confirms that the particle is magnetically bound, as the nickel segment's poles are the strongest attraction points. The motor is actuated by the magnetic nickel segment, which follows closely the external rotating magnetic field. Through boundary actuation, the flexible silver filament deforms in a chiral fashion to produce propulsion in the direction towards the nickel segment. The necessity of chirality in the deformation for propulsion was established in our previous work, together with a simple elastohydrodynamic model for its propulsion.[32] Using high-definition images, we noticed that the deformation of the flexible filament does not seem to change significantly after picking-up the cargo sphere. The deformation of the silver segment is very apparent in the slow-motion video frames, which show the segment whipping and driving the propulsion of the cargo-carrying wire through the fluid. The exact

shape of the silver filament is a result of the competition from magnetic actuation, elastic forces from the flexible filament, and viscous forces from the fluid medium.[32] Overall, these results demonstrate that our flexible magnetic nanoswimmers are able to transport micrometer particles at high speeds, both dimensional (up to 10 μm s^{-1}) and dimensionless (up to 0.2 body lengths per revolution).

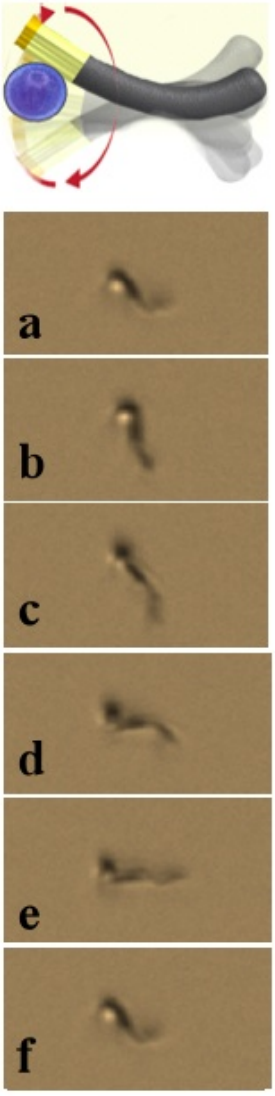

Figure 4.2.1 Time-lapse images depicting the slow motion of a magnetic nanowire motor with a 1.0 μm drug-loaded magnetic PLGA microsphere. The time interval between each image is 20 ms. Scale bar 5 μm. Magnetic field: f = 10 Hz, H_1 = 10 G, and H_0 = 9.5 G.

4.2.3.2 Size Dependent Transport

The picking up of polymeric magnetic particles of distinct, different sizes (radii ranging from 500 nm to 2.5 μm) was used to assess the influence of cargo size on the nanomotors' speed and trajectory. Figure 4.2.2 shows actual optical images highlighting the directed motion of the magnetic nanomotor towards a drug-loaded PLGA particle, followed by the instantaneous capture of a magnetic polymeric sphere by the nanomotor and its transport. This cargo loading is accomplished via the magnetic attraction between the nickel segment on the nanomotor and the iron oxide nanoparticles encapsulated in the PLGA particle. Figure 4.2.2 depicts the movement for three PLGA cargo spheres, representative of different particle-size groups (of average diameters 0.65, 1.25, and 2.25 μm). As was illustrated in our previous work,[32] the magnetic frequency and strength have a profound influence on the speed of nanoswimmer, and should thus influence its cargo-towing ability.

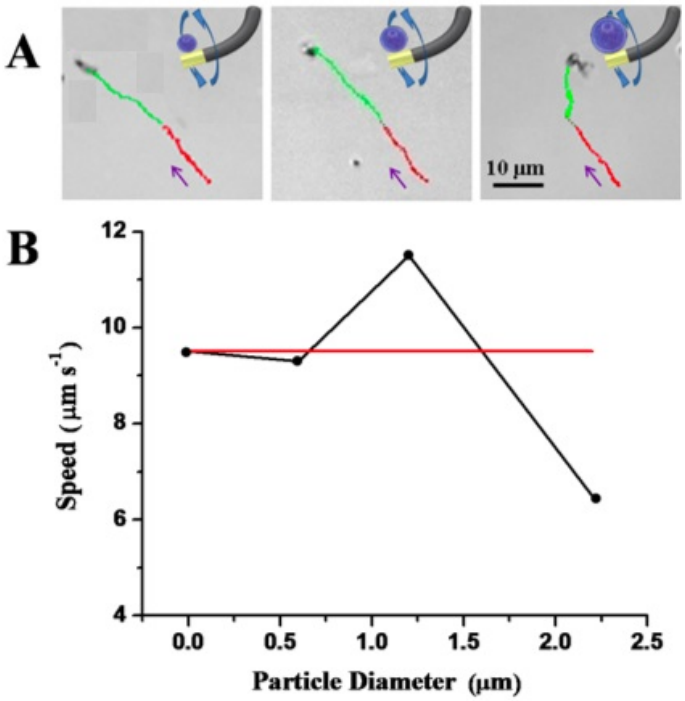

Figure 4.2.2 Capture and transport of different sizes of drug-loaded magnetic PLGA micro/nanoparticles. Time-lapse images show the motion trajectory within 2 s before and after picking up the different-sized, drug-loaded PLGA particles, respectively. B) Variation of the speed of the magnetic nanowire motors after picking up different sizes of drug-loaded PLGA particles. Error bars estimated as a triple of the standard deviation (n = 20). Magnetic fields as in Figure 4.2.1.

In previous studies on cargo transportation using catalytic fuel-driven nanomotors,[12,13,23] loaded particles were found to increase the hydrodynamic resistance, and led to a monotonic decrease in propulsion speed with particle size. Upon loading, the hydrodynamic center changes only along the axis of the nanowire; since the motion of the catalytic motor is only along the axial direction, the loading process simply contributes additional hydrodynamic drag to the motor. The additional loading obeys Stokes' law for the viscous resistance of spheres (the force (F) to speed (U) ratio is given by $F/U = 6\pi\mu a_r = R_s a_r$ where a_r is the dimensional radius of the

sphere, R_s is $6\pi\mu$, and μ is the fluid viscosity) and results in a monotonic decrease in propulsion speed upon increasing the size of the loaded particle. In contrast, here, we observe an unusual nonmonotonic impact of the cargo loading on the speed and trajectory of the magnetic nanowire motors. As shown in Figure 4.2.2B, for the small drug-loaded particles (average diameters of 0.2 and 0.65 μm), the cargo-loaded nanomotors travel at approximately the same speed (9.5 μm s^{-1}) as before the loading; for the medium size of cargo (average diameter of 1.25 μm), we observed an unexpected (≈20%) increase in the propulsion speed after pick-up; however, a significant reduction in the average speed (≈33%) was observed for the very large particle (average diameter of 2.25 μm). We attributed this increase to a subtle change, brought about by the loading process, in the boundary condition for the filament actuation. Unlike catalytic motors, the attachment of a spherical particle to the magnetic nickel segment of the current motor not only increases the viscous drag, but also perturbs the total force and torque balances, which in general lead to a deformation of the entire silver filament. Since the propulsion speed is a fuction of the shape of the silver filament,[15] a nontrivial modification to the propulsion speed is expected. This is also likely to be the cause because particle's magnetic moment is several orders of magnitude smaller than that of the nickel segment so its presence would have little impact on the speed.

For large particles (≈2 μm in diameter), in addition to the 30% reduction in speed, we also observed a significant change in the motor trajectory after loading. For unloaded motors, or when the loading particle is small, the motor propels in the

direction of the axial magnetic field both before and after the loading (Figure 4.2.2A, left and middle panel). However, when the cargo is large, the new trajectory is seen to occur at an angle with respect to the axial magnetic field (Figure 4.2.2A, right panel). Such a change in the cruising angle could be attributed to hydrodynamic interactions with surfaces, which is expected to play a more significant role when the loading particle is large. The presence of a surface breaks spatial symmetry and the viscous drag experienced by a moving body is higher when located close to the bottom surface. Tierno et al. first exploited this type of drag anisotropy in order to convert the rotational motion of an anisotropic colloidal doublet (i.e., a small sphere attached to a larger sphere) near a surface into translational motion.[36,37] As pointed out in their work, the higher viscous drag near the surface plays a role similar to the solid friction between a rolling wheel and a solid surface. When loaded with a particle, our current nanowire motor is geometrically similar to an anisotropic doublet, and hence we suspect that the off-axis propulsion velocity after loading is due to a similar mechanism. The current nanowire motor performs thus both as a flexible propeller (propelling in the direction of the constant magnetic field) and as a surface walker (propelling in a direction perpendicular to the constant magnetic field) when it is loaded with a large particle in the presence of a surface. For future applications close to a surface/boundary and requiring a preservation of the cruising direction, the cargo particle has therefore to be limited in size to avoid any interference with the swimming direction of the motor.

4.2.3.3 Targeted Drug Delivery

The results obtained through the former study illustrate that the iron oxide-loaded polymeric particles and the size of the nickel segment within the nanomotors are sufficient for enabling the particle's pick-up and transport. These results also demonstrate that the size of the drug-loaded spheres plays a significant role in the speed and trajectory of the cargo- loaded Ni–Ag nanowire motors. After having studied the physicochemical properties and cargo-carrying capability of the magnetic nanoswimmers, we next examine the potential practical utility of these fuel-free nanomotors by experimentally delivering drug (e.g., doxorubicin)-loaded PLGA microparticles to cancer cells in an in-vitro setting. This active transport, which usually occurs at a rate orders of magnitude faster than diffusion,[23] takes place through a microchannel that connects the pick-up zone to the release microwell, as illustrated schematically in Figure 4.2.3A. The corresponding experimental results are shown in Figure 4.2.3B (corresponding Video 4.2). For systemic drug-delivery purposes, most drug carriers (e.g., PLGA particles and liposomes) are used at a size smaller than 1 μm, where the flexible nanomotors do not have any obvious speed changes. In this study, in order to directly visualize the concept of delivering drug-loaded particles to target cancer cells, we used PLGA particles of around 1.25 μm in size. Experiments were conducted using HeLa cancer cells because they can readily adhere to the plasma-treated glass wells when incubated overnight in a culture medium. Repeatedly washed, flexible nanowire motors and drug-loaded PLGA particles were added to a culture medium solution in the left well and the cancer cells were seeded and cultured in the

right well. Figure 4.2.3 shows both a cartoon (panel A) and captured experimental images of a five-step in-vitro process, which is used to emulate the fuel-free motors drug delivery capabilities (panel Ba–e). First, the flexible nanomotor approaches the target iron oxide/doxorubicin-encapsulated PLGA particle in a cell-free well via precise magnetic guidance (point marked ‘a’). As the motor passes close by the particle, the particle is magnetically attracted and picked up (point ‘b’). The long-range transport capability of the flexible nanomotor is then tested while it tows and guides the PLGA particle across the channel (‘c’) and to the open secondary well containing the HeLa cancer cells. The nanomotor is then guided to a target HeLa cancer cell (‘d’), which is attached and spread across the bottom surface. Finally, the flexible silver segment of the nanowire nonspecifically bound to the HeLa cell to enable localized drug release from the PLGA particle (‘e’). We observed this nonspecific binding several times when the motor was directed to the cancer cell and given enough time to interact. In most cases the cargo-loaded nanomotor tended to travel around or over the cell as it perpetually interacted with the cellular membrane. Future endeavors could involve nanomotors functionalized with antibodies specific to cancer cells, to increase their binding efficiency once they have been directed to the target cells. This nanomotor-based, targeted, drug-delivery system involving fuel-free nanovehicles may potentially address current challenges of nanoparticle drug delivery, such as inevitable off-targeting of particles and the likelihood of systemic toxicity.

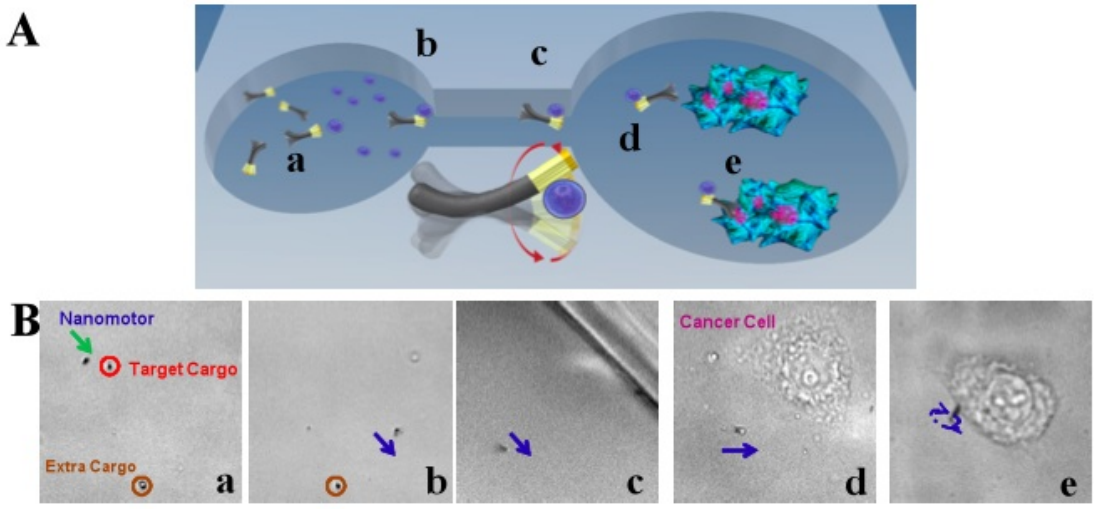

Figure 4.2.3. Drug delivery to HeLa cells using flexible magnetic nanoswimmers in cell-culture media. A) Scheme depicting the process as a flexible magnetic Ni–Ag nanowire motor (a); captures the drug-loaded magnetic polymeric particle in the loading reservoir (b); transports it through the channel (c); approaches the target cell (d); sticks onto the target cell, and releases the drug (e). B) Time-lapsed images illustrating each of the previous described steps, taken from Supporting Video 4.2 The arrows show the moving direction of the nanoswimmer. Conditions as in Figure 4.2.1.

4.2.4 Potential Targeted Drug Delivery by Magnetic Nanomotors

Conclusions

In conclusion, we demonstrated the first example of directed transport of magnetic polymeric drug carriers by fuel-free flexible magnetic nanomotors, investigated both experimentally and theoretically the influence of such cargo upon the propulsion speed and trajectory of the loaded motor, and elucidated the fundamental mechanism of such cargo towing. These fuel-free nanomotors have been shown useful for the pick-up and transport of various drug carriers from a loading zone to a predetermined destination through a predefined route, and they represent a novel approach towards transporting cargos in a target specific manner. Note that the transport occurs at a rate order of magnitude faster than that expected from Brownian

motion. The new understanding will ultimately enable us to address the performance and physical limitations of nanomotor-towing for the efficient transport of biological and therapeutic payloads.

Despite these significant advancements of nanomotor design and our new understanding of the ability of the flexible nanoswimmer to transport cargo, several challenges still exist for their practical in-vivo use. Enhancements on the propulsive thrust and cargo attachment are necessary to overcome any additional hydrodynamic drag and shear present in the in-vivo environment. To further improve the efficiency of nanomotor-based drug delivery, we envision the possibility of attaching drug carriers to these magnetically driven nanoswimmers through cleavable linkers that are responsive to tumor microenvironments (e.g., enzymes and acidic pH) to enable an autonomous release of the carriers and a more accurate delivery of cargos to the target site. While eliminating the fuel requirements, attention must be given also to the preparation of more biocompatible magnetic nanowimmers. Eventually, such magnetically driven fuel-free nanoswimmers are expected to provide a new and unique approach for rapidly delivering drug carriers to predetermined destinations in a target-specific manner.

4.3 Ultrasound-Triggered Microbullets for Targeted Drug Delivery

4.3.1 Ultrasound-Triggered Microbullets for Targeted Drug Delivery Introduction

Recent advances in nanomachines have shown great promise in diverse fields.[1,2,16,24,27,28,38-45]A wide variety of chemically-powered and magnetically-propelled micro/nanoscale motors have been developed for specific biomedical applications ranging from lab-on-chip bioanalytical devices to site-specific drug delivery targeting. However, these nanomachines lack the power and biocompatibility necessary for penetrating tissue and cellular barriers, for *in vivo* cargo delivery and precision nanosurgery. Herein we present a highly efficient microscale propulsion technique that utilizes ultrasound (US) to externally trigger on-board fuel (*i.e.*, perfluorocarbon (PFC) emulsions) bound within the motor's interior for high velocity, bullet-like propulsion. These new US-driven microbullets (MBs) can travel at remarkably high average velocities (~6.3 m/s: over 100 times faster than currently published micromachines[2,39,46]) and deeply penetrate and deform kidney tissue. The concomitance of powerful MB propulsion and deeply penetrative yet medically safe US could lead to highly targeted *in vivo* drug delivery, artery cleaning, gene regulation schemes, and cancer therapeutics that require higher specificity and accuracy than the current state-of-the-art.

Current micro/nanoscale motor designs typically require conversion of external chemical energy, located in the vicinity of the rockets, to promote autonomous propulsion. Several mechanisms have been developed to realize such rocket thrust in connection to hydrogen-peroxide fuel, including self-electrophoresis,[1,2] self-diffusiophoresis,[45] and bubble propulsion.[2,38,46] To enhance biocompatibility several groups have also explored fuel-free microrocket propulsion mechanisms, including the utilization of electrical power (*i.e.*, diode nanowires[47]) and magnetic oscillation.[15,17,31] Despite the inherent advantages of such externally-propelled microscale locomotion schemes, these propulsion mechanisms do not possess the thrust needed for penetrating tissue barriers and cellular membranes.[44]

This section describes a new US-triggered, microscale propulsion technique that is capable of inducing sufficient nanomotor thrust for deep tissue penetration and deformation. Similar to the externally triggered explosion experienced within a gun barrel to propel a bullet,[48] these microbullets (MB) utilize the rapid expansion and vaporization of perfluorocarbon droplets,[49] electrostatically bound within the motor interior and triggered by an US pulse (*i.e.*, acoustic droplet vaporization (ADV)),[50,51] for propulsion. The resulting US-driven MB possesses remarkable energy and penetrative force for tissue and cellular penetration. The ability of US to externally access deep tissue and its history of safe and effective US clinical usage,[52,53] combined with the biocompatible nature of the PFC emulsions creates a propulsion mechanism well-suited for *in vivo* applications. The tapered conical structure of the MBs directs thrust from ADV while an embedded magnetic layer permits externally-guided,

magnetic alignment for precision steering. Thus, both the MB structure and composition lead to unprecedented nanomotor power and control that facilitate, for the first time, an attractive pathway for targeted tissue penetration and deformation.

4.3.2 Ultrasound-Triggered Microbullets for Targeted Delivery

Experimental Methods

4.3.2.1 Large microbullet (MB) (length >= 40 μm) fabrication

The Ti/Ni/Au MBs that were 40 μm or greater in length were prepared by modifying a previous top-down photolithographic protocol, which involves angled e-beam evaporation to provide stress-assisted rolling of functional nanomembranes on polymers into conical microtubes.[7,9] First, a positive microposit S1827 photoresist (Microchem, Newton, MA) was spin-coated onto a silicon wafer at 3000 rpm for 60 seconds. The coated-wafer was baked for 60 seconds at 115 °C before UV light (35 seconds) exposure using a MA6 mask aligner and various-sized MB patterns. Exposed patterns were etched using a MF-321 developer for 90 seconds before washing thoroughly with DI water. Metallic layers of Ti (10 nm), Ni (15 nm), and Au (15 nm) were evaporated sequentially onto the waferfor microrockets 40 and 60 μm in length via an e-beam evaporator (Temescal BJD 1800) under high vacuum conditions ($<10^{-8}$ Pa). For larger MBs (> 100 μm), 20nm of Ni and Au were deposited to provide needed support. The e-beam substrate holder was tilted to 48° in all cases to asymmetrically deposit the metals on the patterns. Resist remover, MF-1165 (Rohm & Haas, Marlborough, MA), was applied to the pre-stressed metallic layers, allowing for the

immediate self-assembly of microtubes. The MBs underwent critical-point drying to prevent unwarranted tubular collapse.

4.3.2.2 Small microbullet (MB) (length ~8 μm) fabrication

Alternatively, small 8 μm MBs were prepared by electrodepositing sequential layers into a cyclopore polycarbonate membrane, containing numerous 2 μm conical-shaped pores (Catalog No 7060-2511; Whatman, Maidstone, U.K.).[17] The electrodepostion of an outer polyaniline (PANI) layer and inner Au layer was carried out using a three-electrode set-up.[8] PANI microtubes were electropolymerized at +0.80 V for 0.02 C from a solution containing 0.1 M H_2SO_4, 0.5 M Na_2SO_4 and 0.1 M aniline; subsequently, the inner gold layer was plated at -0.9 V for 1 C from a commercial gold plating solution (Orotemp 24 RTU RACK; Technic Inc.). The membrane was dissolved in methylene chloride and repeatedly washed in methylene chloride, ethanol and ultrapure water. Electron beam evaporation of 10 nm Ti (adhesion layer) and 26 nm Ni (magnetic layer) onto the dried MBs was used to magnetically orient the small MBs.

4.3.2.3 Perfluorocarbon emulsion preparation protocol

Perfluorohexane and perfluoropentane nanoemulsions were prepared in phosphate buffer saline (PBS). Briefly, 10 μL of 1 mM DiI-C18 (Biotium, Hayward, CA) dissolved in chloroform was evaporated in a 1.5 microcentrifuge tube. 850 μL PBS was added to the solution and a XL-2000 (Misonix, Farmingdale, NY) probe-type sonicator was operated at the bottom of the tube at level 20 until the DiI film was

completely suspended in the buffer and the solution become hot to the touch. The tube was immediately placed in a heating block at 90ºC for 5 minutes and 50 µL of Zonyl FSE (Wilmington, DE) anionic fluorosurfactant was added. The solution was vortexed until homogenized and subsequently cooled in an ice bath. An 100 µl aliquot of perfluoropentane (Strem Chemicals, Newburyport, MA) or perfluorohexane (Alfa Aesar, Ward Hill, MA) was added and an XL-2000 (Misonix, Farmingdale, NY) probe was lowered in the tube about 8 mm from the bottom. While still in the ice bath, the sonicator was operated with a LabVIEW program interfaced with the sonicator via a foot pedal input and a reed relay board. The program delivered three 0.5 second bursts and was repeated 60 times. The short bursts prevented the solution from stirring violently and producing foam; a 15 sec delay between each set of 3 bursts served to prevent overheating. This process resulted in a 10 vol% PFC emulsion which was stable and turbid in appearance. Emulsion sizes and zeta potentials were measured by dynamic light scattering with a Zetasizer Nano-ZS (Malvern Instruments, Worcestershire, UK). The 10 vol% PFC emulsion was diluted to 1% vol% by a PBS pH 7.4 solution before incubating with the MBs.

4.3.2.4 Conjugation of perfluorocarbon emulsion to microbullet

The inner Au layer allowed electrostatic binding and selective localization of the perfluorocarbon emulsions to the inner cavity of the bullet; thus bubbles were formed within and emitted from the MBs during US pulses. This Au interior layer provided an optimum surface for direct cysteamine binding (10mg/mL in water), thereby forming a densely packed monolayer within 5 minutes.[56] The exposed amine

group (pKa 8.6) of the cysteamine[31] is positively charged for the prescribed experimental settings (*i.e.*, pH range 7.4 - 8.0) and thus electrostatically binds to emulsions stabilized with an anionic phosphate fluorosurfactant (pKa 7.2). Emulsions were strongly negative with a measured zeta potential of -46 mV in phosphate buffered saline.

Before the electrostatic emulsion binding, copious amounts of DI water were used in numerous washing steps (~15) to remove all excess cysteamine. To ensure optimal emulsion binding for sufficient MB propulsion, the MBs were incubated overnight within the perfluorohexane emulsion under continuous flat shaker agitation (400 rpm). The MBs were repeatedly washed (10 times) with PBS/ultrapure H_2O (1:1000; final pH 8.0) before experimental testing. This composition of the washing solution prevents MBs from electrostatically binding to the glass surface while still promoting the emulsion/MB interaction. Furthermore, saturation with liquid perfluorohexane (non-active) was used to prevent dissolution of the bound emulsion while stored for several days before experimental testing.

4.3.2.5 Ultrasound (US) triggered (MB) propulsion

Subsequent MB propulsion was initiated by an US signal generated by a Panametrics V305-SU (Olympus NDT Inc., Waltham, MA), 2.25 MHz transducer connected via a Panametrics BCU − 58–6 W waterproof connector cable. The transducer was positioned within a water tank while the MBs were positioned at the water surface level between a glass slide and cover slip. Distinct US waveforms were

generated from aPCI-5412arbitrary waveform (National Instruments, Austin, TX) and amplified by a 300 W amplifier (Vox Technologies, Richardson, TX) to create acoustic intensities of up to 3 MPa peak negative pressure at the focus. A custom-designed LabVIEW 8.2 program was utilized to initiate the US pulses while a Photron FASTCAM 1024 PCI acquired the image sequences. A 40x magnification lens was used to acquire most initial experiments to visualize the gaseous bubbles; a 10x magnification lens was used to observe MBs locomotion and tissue penetrating characteristics. The glass slide acted as a coupling medium between the water tank and the MBs for the US pulses. In order to reduce the MB velocity for improved imaging, 20%v/v glycerol was added to the MB solution to increase the viscosity.

4.3.2.6 Microrocket imaging

In order to capture the MB propulsion videos, individual image frames were acquired at 10,000 or 18,000 frames per second (fps) using a (10X, 20X or 40X Objective) FASTCAM 1024 PCIhigh speed camera (Photron, San Diego, CA).

4.3.2.7 Force and speed Calculations

The velocity of the MB locomotion was calculated via Stoke's law. With the observations of the MB motion, and the Stokes' drag law for cylinders,[58] it is possible to calculate many key physical parameters. $F_d = \frac{2\pi\mu L}{ln\left(\frac{2L}{R}\right) - 0.72} v$, or $F_d = kv$, where $k = \frac{2\pi\mu L}{ln\left(\frac{2L}{R}\right) - 0.72}$,

and μ is the viscosity of the medium, L is the length, R is the radius, and v is the velocity. Using values from the below table, the average speed is 6.3 m/s determined from the distance traveled of 350 μm in 1/18,000 seconds (time elapsed in one frame). Using this calculated velocity in the Stokes' drag law for cylinders, the average drag force is determined to be 50.6 μN. To calculate the initial impulse of the US triggered propulsion initial MB's speed and metal mass (negating the inner air/liquid containing volume) were evaluated to determine the instantaneous change in momentum.

The equation for the change in velocity over time (acceleration) was utilized to calculate the initial MB velocity

$\frac{dv}{dt} = -\frac{F_d}{m} = -\frac{kv}{m}$, where m is the mass of the MB. By solving this differential equation, one can obtain the velocity function,

$$v(t) = v_0 e^{-\frac{kt}{m}}$$

, where v_0 is the initial velocity—subsequently determined by integrating the velocity over the length of one image frame

$$\int_0^{\Delta t} v(t)dt = \Delta d$$

Since the frame length, Δt is known from the camera settings, and the distance travelled, Δd is also known from image calibration, one can express the initial velocity in terms of known quantities,

$$v_0 = \frac{\Delta d}{\frac{m}{k} - \frac{m}{k} e^{-\frac{k\Delta t}{m}}}$$

Using these derived equation along with the quantity values displayed in methods, the initial velocity is calculated to be 56.9 m/s. Thus an initial momentum (p = mv) of 2.69E-11 Ns and kinetic energy (KE = ½mv^2) of 0.764 nJ was calculated for a MB with mass of 4.74E-13 kg. A special note should be considered when reviewing these calculations. Although it was possible to capture image sequences at frame rates greater than 18,000 fps, the MB velocity was so great that it was not possible to capture more than 2 or 3 frames during motion within the limited field of view. Since this was a memory speed limitation and not a limitation due to amount of light, we were, however, able to use shutter speeds of at least 1/303,000 seconds which could freeze the objects in motion. Thus, the velocity calculations presented herein are an approximation due to the limitations in MB image capturing.

Table 4.2. Table containing all the necessary values to help calculate the speed and force calculations for ultrasound triggered propulsion.

Velocity Components	**Values**
Average Density	11.7g/cm^3
Pre-rolled Volume (L x W x T)	(40 x 25 x .04 μm) = 4.00E-11cm^3
Mass	4.74E-13 kg
Solution Viscosity	1.05 cP
Radius Rolled MB	2.5 μm
Time Between Frames	1/18000 s
Distance Traveled	350 μm
Drag Coefficient	8.89E-8

4.3.3 Ultrasound-Triggered Microbullets for Targeted Delivery

Results and Discussion

4.3.3.1 Concept

A three-step fabrication strategy, was utilized for preparing the US-triggered MBs, including nanofabrication (A), cysteamine functionalization (B), and PFC emulsion binding (C). Large MBs (length ~40μm) were created via rolled-up thin-film nanofabrication techniques,[16,27,28,38] while small MBs (length ~8μm) utilized polycarbonate membrane template electrodeposition for fabrication (see Methods).[46] An embedded Ni layer facilitates MB magnetic washing and experimental alignment while an inner Au layer permits cysteamine monolayer conjugation for electrostatic attachment of perfluorohexane (PFH) droplets. To initiate this study, perfluorohexane (PFH) droplets which possess a low boiling point temperature (56 ºC)[54] were utilized because they maintain stability under physiological conditions but enable ADV upon arrival of incident US pressure waves. To illustrate the selective PFH droplet immobilization strategy developed herein, fluorescently-tagged PFH emulsions, stabilized by a negatively-charged surfactant, were electrostatically immobilized onto the cysteamine-modified inner gold surfaces.

Initial US-triggered propulsion experiments reveal PFH emulsion vaporization originating from within the MBs (Figure 4.3.1). A vaporized emulsion (*i.e.*, bubble) extending out of the tail of the MB is clearly visible after the US pulsation (Figure 4.3.1a), corroborating the assumption that microscale gaseous bubble formation is

resultant upon sudden US-promoted PFH vaporization. The rapid emulsion expansion during the vaporization process (~5 fold radial[49]) provides a sudden impulse that projects the MB out of the microscope field of view within an extremely short single image frame (~55.6 μs). Control experiments over a longer period demonstrate that nonspecific adsorption of PFH was negligible as MBs functionalized without cysteamine or without the PFH emulsion failed to produce bubbles nor MB movement (Figure 4.3.12b and 2c, respectively). US pulsations thus have minimal effect on the locomotion of non-functionalized MBs.

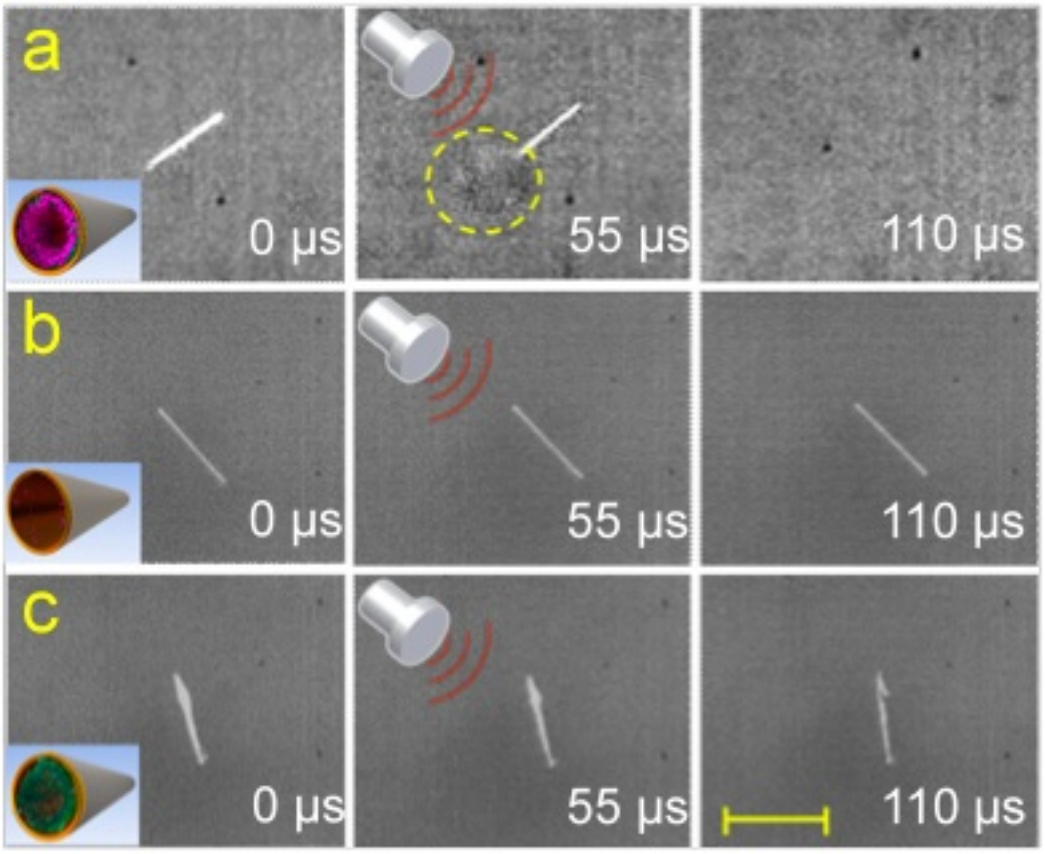

Figure 4.3.1. US triggered MB firing of (a) a fully modified MB, conjugated with cysteamine and containing perfluorohexane emulsion droplets, (b) unmodified MB (without cysteamine) after emulsion incubation, and (c) MB conjugated with cysteamine but without emulsion incubation. Still frame images before, during, and after the 44 µsec, 1.6 MPa US triggering (left to right). All MBs were thoroughly washed in diluted 7.4 pH PBS solution before firing. Images of control MBs (b,c) were taken after every 10 frames to display their negligible movement over a longer time period. A yellow dotted circle accents the emerging bubble during fully conjugated MB firing. Inset images showing the modified microrockets and US triggering were added for clarity. Images were taken at a frame rate of 18,000 fps using a 40X objective. Scale bar = 40 µm.

4.3.3.2 Speed and Force of Microbullets

In order to enhance the visualization of MB movement for subsequent analysis, the MBs were viewed under a low magnification lens (10X) and at times placed in a dtraveling 350 µm from its initial location within 55.6 µs upon vaporization of the

PFH emulsion and formation of a gas bubble. Therefore, the MB traveled at a remarkably high average velocity of 6.3 m/s, corresponding to an ultrafast relative velocity of over 158,000 body-lengths/s. The MB dynamics were analyzed with Stokes' Law and experimental image analysis (see Experimental Methods). The initial microrocket velocity (56.9 m/s), kinetic energy (0.764 nJ) and momentum (2.69e-11) were calculated with Eqs. 1-3 in conjunction with MB parameter values presented in Table SI1 (see Methods for equation derivations and parameter values):

$$v_0 = \frac{\Delta d}{\frac{m}{k}\left(1-\frac{m}{k}e^{-\frac{k\Delta t}{m}}\right)} \quad (1)$$

$$E_k = \frac{1}{2}mv^2 \quad (2)$$

$$p_0 = mv_0 \quad (3)$$

where k is the drag coefficient for a cylinder, m is the mass of the hollow MB (kg), Δd is distance traveled (m), t is time (s), and E_k is kinetic energy (J). The remarkably high initial and average MB velocities associated with US-triggered emulsion vaporization compare favorably with velocities achieved for stochastically moving microparticles propelled by water cavitation.[55]

4.3.3.3 Optimizing Ultrasound Triggered Propulsion

In order to promote highly efficient, single-shot, and controllable MB firings, the US trigger settings (*i.e.*, transducer pressure and pulse length) and MB fabrication (*i.e.*, size, shape, thickness) were optimized. The MB locomotion was observed in four

distinct US pulse settings: long pulse (444 μsec))/low pressure (1.6 MPa), medium length pulse (44 μsec)/high pressure (3.8 MPa), and medium length pulse (44 μsec)/low pressure (1.6 MPa), and short pulse (4.4 μsec)/high pressure (3.8 MPa). Long pulses (1000 cycles) produced streams of bubbles and subsequent circular MB motion. High transducer pressures (3.8 MPa) often caused water cavitation which when delivered in medium length pulses resulted in sustained cavitation and solution mixing that created sporadic MB movement. However, the combination of low pressure/medium pulse and high pressure/short pulse produced linear MB locomotion from ADV without external water cavitation.

While ADV assisted propulsion is possible for a number of different structures in the nano-millimeter range, MBs (40 nm thick, 40 μm long and 2.5 μm in diameter) produced ultrafast curvilinear motion when 180 nm diameter-sized PFH emulsions were utilized. Long MBs (lengths > 100 μm) often rotated uncontrollably in circular motion as streams of ADV induced bubbles expelled from both the front and back MB orifices. Long and slender MBs (60 μm long, 400 nm thick, 3 μm in diameter) exploded upon US triggering. Smaller MBs (8 μm long, 800 nm inner diameter) fired less frequently and experienced stochastic locomotion that can be attributed to smaller surface area for emulsion functionalization and less mass for stability respectively. Additional functionalization tests, revealed that lower boiling point emulsions (perfluoropentane, BP: 30 ºC[54]) did vaporize more consistently at low pressures but were less stable during functionalization and increased MB explosion during US

triggering. Further optimization of the emulsion size and composition could thus be used to tailor US triggered propulsion devices for specific biomedical applications.

4.3.3.3 Microbullet Tissue Penetration

To demonstrate the ability to penetrate through dense materials for potential targeted delivery applications, MBs were fired into tissue sections from a lamb kidney. The image sequence (Figure 4.3.2) and corresponding video 4.3 depicts the deep penetration of the MB into the lamb kidney tissue section after an US pulse. These sequential images illustrate the MB before locomotion (4a), during initial tissue penetration (4b), and after traveling 200 μm into the tissue (4c,d) from a single 44 μsec, 1.6 MPa US pulse. A very short US pulse (4.4 μsec) at high pressure (3.8 MPa) also provided sufficient thrust for the MBs to pierce kidney tissue. Figure 4.3.3 depicts the ability of the US-triggered MB to penetrate, deform, and cleave kidney tissue. Progressive images illustrate the MB capturing, deforming, and transporting a small piece of kidney tissue after a 44 μsec, 1.6 MPa US pulse (Figure 4.3.3b,c). Therefore, the US pulse pressure can be tuned to permit MB tissue piercing, deformation, or deep penetration, depending upon the specifications and tissue degradation restrictions of distinct biomedical applications. Furthermore, the ability to propel multiple MBs from the same US pulse into a tissue section was also shown to be possible. This potential power of multiple US-triggered MBs can be visualized as the MBs increase the tissue cavity area by 120% after the first 4.4 μsec/3.8 MPa US pulse and penetrate the kidney tissue after a second US pulse.

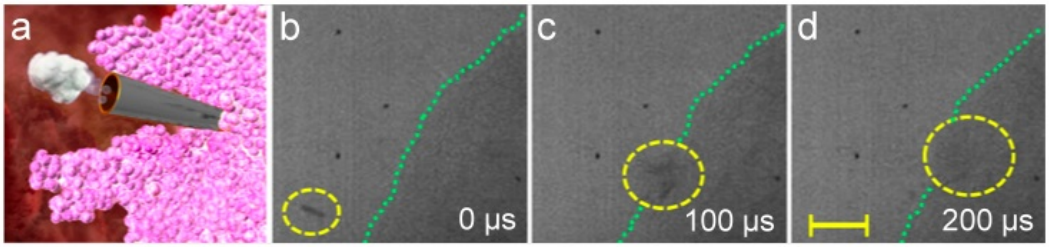

Figure 4.3.2 (a) Illustration of the MB's deep tissue penetration after using a 44 µsec/1.6 MPa US pulse. Sequential images depicting the MB stationary (b), impacting the tissue (c), and travelling through the tissue (d). A dotted yellow circle is added to help track the MB's position, and a green dotted line outlines the tissue. The view of the MB becomes obscured as it penetrates and enters the tissue. Images were taken sequentially at a frame rate of 10,000 fps and 10X objective. Scale bar = 100 µm.

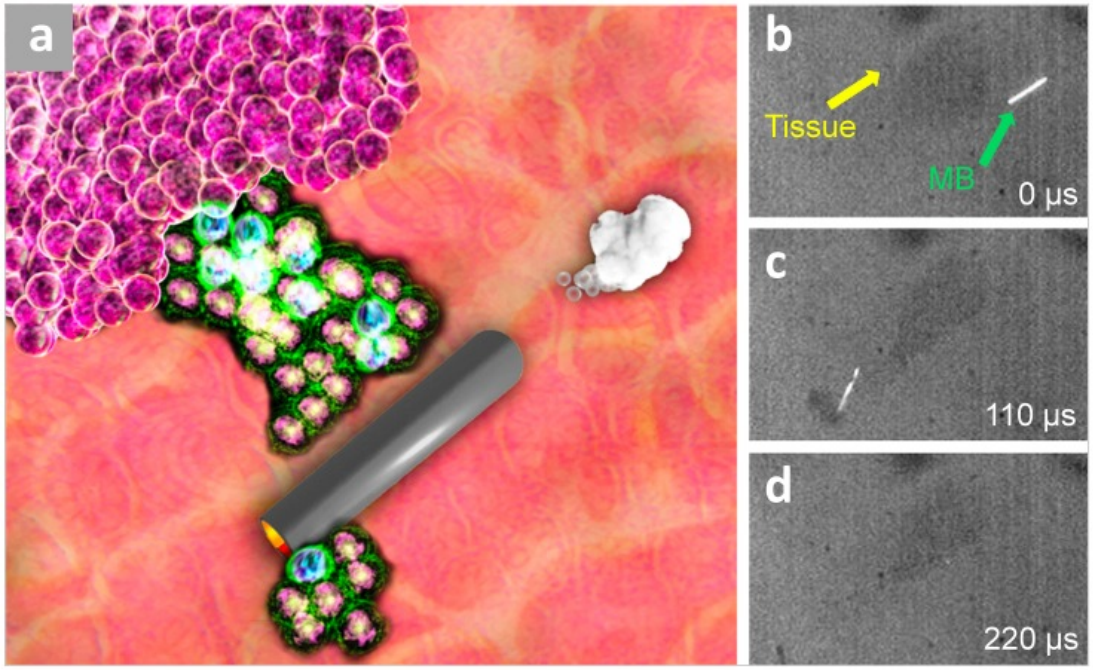

Figure 4.3.3. (a) Computer-aided graphic portraying a MB cleaving apart a diseased tissue section mimicking a nanosurgery operation. Sequential images (b-d) were used to display the MB's ability to cleave apart a tissue sample during impact. The MB and small tissue sample are shown before a 44 µsec/1.6 MPa US pulse (b), while in motion (c) and during deceleration (d). Images were taken sequentially at a frame rate of 10,000 fps (i.e., 0.1 msec intervals) using a 10X objective. Scale bar = 60 µm.

4.3.3 Ultrasound-Triggered Microbullets for Targeted Delivery

Conclusions

The presented ultrasound-triggered microbullet firing technique offers a safe, low-cost, and effective method to project delivery devices into dense tissue or organs. These US-triggered MBs possess the unique ability to accelerate rapidly, acquire significant momentum (2.69 X 10^{-11} Ns), and reach speeds over 6 m/s that are approximately 100 times faster than previous micromachines. This unprecedented MB speed and force enables lamb kidney tissue piercing, deep penetration, deformation, and cleaving—capabilities that, to our knowledge, have never been demonstrated with nanomotors. Furthermore, the MB speed and power can be tailored for diverse applications by adjusting the size and shape of the MBs and the size and composition of the embedded emulsion. Since multiple MBs can be simultaneously fired from a single US pulse, we expect that the US-triggered MB propulsion strategy will have a tremendous impact on diverse biomedical applications (*e.g.*, targeted drug delivery, circulating biolistics, micro-tissue and artery-cleaning/removal schemes, precision nanosurgery, and cancer therapeutics). For example, as an alternative to Bacillus Calmette-Guerin (BCG) treatment for bladder cancer, the US-triggered MBs could be introduced and fired into the bladder to create a natural inflammatory response for fighting cancer cells, similar to the immunoprophylactic effect, to potentially eliminate harmful side effects (*e.g.*, sepsis, dysuria, hematuria, nausea, and fever) associated with BCG.

Chapter 4.1 is based on the material as it appears in Small, 2010, by Daniel Kagan, Rawiwan Laocharoensuk, Maria Zimmerman, Corbin Clawson, Shankar Balasubramanian, Dae Kang, Daniel Bishop, Sirilak Sattayasamitsathit, Liangfang Zhang, and Joseph Wang; Chapter 4.2 is based on the material as it appears in Small, 2012, by Wei Gao, Daniel Kagan, On Shun Pak, Corbin Clawson, Susana Campuzano, Beke Chuluun-Erdene, Eric Shipton, Eric Fullerton, Liangfang Zhang, Eric Lauga, and Joseph Wang; Chapter 4.3 is based on the material submitted to Nature Nanotechnology, 2012, by Daniel Kagan, Mike Benchimol, Jonathan Claussen, Beke Chuluun-Erdene, Sadik Esenser, and Joseph Wang. The dissertation author was the primary investigator and co-author of these papers.

4.4 References

1. Mallouk, T. E.; Sen, A. *Sci. Am.* **2009***, 300*, 72– 77.

2. Wang, J. *ACS Nano* **2009***, 3*, 4– 9.

3. Mirkovic, T.; Zacharia, N. S.; Scholes, G. D.; Ozin, G. A. *ACS Nano* **2010***, 4,* 1782–1789.

4. Davis, M. E.; Chen, Z. G.; Shin, D. M. *Nat. Rev. Drug Discov.* **2008***, 7,* 771.

5. Zhang, L.; Gu, F. X.; Chan, J. M.; Wang, A. Z.; Langer, R. S.; Farokhzad, O. C. *Clin. Pharmacol. Ther.* **2008***, 83,* 761.

6. Jain, R. K. *Cancer Res.* **1987***, 47*, 3039.

7. Peer, D.; Karp, J. M.; Hong, S.; Farokhzad, O. C.; Margalit, R.; Langer, R. *Nat. Nanotechnol.* **2007***, 2,* 751.

8. Golestanian, R.; Liverpool, T. B.; Ajdari, A. *Phys. Rev. Lett.* **2005***, 94,* 220801.

9. Tao, Y-G.; Kapral, R. *J. Chem. Phys.* **2009***, 131,* 024113.

10. Ruckner, G.; Kapral, R.; *Phys. Rev. Lett.* **2007***, 98,* 150603.

11. Moran, J. L.; Wheat, P. M.; Posner, J. D.; *Phys. Rev. E.* **2010***, 8,* 065302.

12. Burdick, J.; Laocharoensuk, R.; Wheat, P. M.; Posner, J. D.; Wang, J. *J. Am. Chem. Soc.* **2008***, 130*, 8164– 8165.

13. Sundararajan, S.; Lammert, P. E.; Zudans, A. W.; Crespi, V. H.; Sen, A. *Nano Lett.* **2008***, 8,* 1271–1276.

14. Sundararajan, S.; Sengupta, S.; Ibele, M. E.; Sen, A. *Small* **2010***, 6,* 1479–1482.

16. Ghosh, A.; Fischer, P.; *Nano Lett.* **2009***, 9,* 2243.

17. Zhang, L.; Abbott, J. J.; Dong, L.; Peyer, K. E.; Kratochvil, B. E.; Zhang, H.; Bergeles, C.; Nelson, B. J. *Nano Lett.* **2009,** *9,* 3663–3667.

18. Torchilin, V. P. *Nat. Rev. Drug Discov.* **2005***, 4,* 145.

19. Laocharoensuk, R.; Burdick, J.; Wang, J. *ACS Nano* **2008***, 2,* 1069.

20. Massart, R. *IEEE T Magn.* **1981***, 17,* 1247.

21. Chaisri, W.; Hennink, W. E.; Okonogi, S. *Curr. Drug. Deliv.* **2009**, 6, 69-75.

22. Nobuto, H; Sugita, T.; Kubo, T.; Shimose, S.; Yasunaga, Y.; Murakami, T.; Ochi, M. *Int. J. Cancer.* **2004***, 109,* 627.

23. Kagan, D.; Laocharoensuk, R.; Zimmerman, M.; Clawson, C.; Balasubramanian, S.; Kang, D.; Bishop, D.; Sattayasamitsathit, S.; Zhang, L.; Wang, J. *Small* **2010***, 6,* 2741– 2747.

24. Mei, Y.; Solovev, A. A.; Sanchez, S.; Schmidt, O. G. *Chem. Soc. Rev*. **2011***, 40,* 2109– 2119..

25. Solovev, A. A.; Sanchez, S.; Pumera, M.; Mei, Y.; Schmidt, O. G. *Adv. Funct. Mater.* **2010***, 20,* 2430– 2435.

26. Zhang, L.; Peyer, K. E.; Nelson, B. J. *Lab Chip* **2010***, 10*, 2203.

27. Balasubramanian, S.; Kagan, D.; Hu, C. J.; Campuzano, S.; Lobo-Castañon, M. J.; Lim, N.; Kang, D. Y.; Zimmerman, M.; Zhang, L.; Wang, J. *Angew. Chem., Int. Ed.* **2011***, 50,* 4161– 4164.

28. Kagan, D.; Campuzano, S.; Balasubramanian, S.; Kuralay, F.; Flechsig, G.-U.; Wang, J. *Nano Lett.* **2011***, 11,* 2083– 2087

29. Zhang, L.; Abbott, J. J.; Dong, L.; Kratochvil, B. E.; Bell, D.; Nelson, B. J. *Appl. Phys. Lett*. **2009***, 94,* 64107.

30. Gao, W.; Manesh, K.M.; Hua, J.; Sattayasamitsathit, S.; Wang, J. *Small* **2011***, 7*, 2047-2051.

31. Gao, W.; Sattayasamitsathit, S.; Manesh, K. M.; Weihs, D.; Wang, J. *J. Am. Chem. Soc.* **2010***, 132,* 14403– 14405.

32. Pak, O. S.; Gao, W.; Wang, J.; Lauga, E. *Soft Matter* **2011***, 7,* 8169.

33. Purcell, E. M. *Am. J. Phys.* **1977***, 45*, 3.

34. Lauga, E.; Powers, T. R. *Rep. Prog. Phys.* **2009***, 72,* 096601.

35. Raz, O.; Leshansky, A. M.; *Phys. Rev. E* **2008***, 77,* 055305(R).

36. Tierno, P.; Güell, O.; Sagués, F.; Golestanian, R.; Pagonabarraga, I. *Phys. Rev. E* **2010***, 81,* 011402.

37. Tierno, P.; Golestanian, R.; Pagonabarraga, I; Sagués, F. *Phys. Rev. Lett.* **2008***, 101,* 218304.

38. Solovev, A. A.; Mei, Y.; Bermudez Urena, E.; Huang, G.; Schmidt, O. G., *Small* **2009,** 5, 1688-1692.

39. Campuzano, S.; Kagan, D.; Orozco, J.; Wang, J., *Analyst* **2011,** 136, 4621-4630.

40. Campuzano, S.; Orozco, J.; Kagan, D.; Guix, M.; Gao, W.; Sattayasamitsathit, S.; Claussen, J. C.; Merkocis, A.; Wang, J., *Nano Lett.* **2012**.

41. Wu, J.; Balasubramanian, S.; Kagan, D.; Manesh, K. M.; Campuzano, S.; Wang, J., *Nat. Commun.* **2010,** 1, 36.

42. Sanchez, S.; Solovev, A. A.; Harazim, S. M.; Schmidt, O. G., *J. Anal. Chem. Soc.* **2011,** 133, (4), 701-703.

43. Fan., D.; Yin, Z., Cheong, R.; Zhu, F.Q.; Cammarata, R.C.; Chien, C.L. Levchenko, L. *Nature Nanotech.* **2010***, 5*, 545-51.

44. Gao, W.; Kagan, D.; Pak, O. S.; Clawson, C.; Campuzano, S.; Chuluun-Erdene, E.; Shipton, E.; Fullerton, E. E.; Zhang, L.; Lauga, E.; Wang, J., *Small* **2011**.

45. Howse, J. R.; Jones, R. A. L.; Ryan, A. J.; Gough, T.; Vafabakhsh, R.; Golestanian, R., *Phys. Rev. Lett.* **2007,** 99, 48102.

46. Gao, W.; Sattayasamitsathit, S.; Orozco, J.; Wang, J., **2011,** 31, 11862-11864.

47. Calvo-Marzal, P.; Sattayasamitsathit, S.; Balasubramanian, S.; Windmiller, J. R.; Dao, C.; Wang, J., *Chem. Comm.* **2010,** 46, (10), 1623-1624.

48. Park, H. C.; Byun, K. T.; Kwak, H. Y., *Chem. Eng. Sci.* **2005,** 60, 1809-1821.

49. Wong, Z. Z.; Kripfgans, O. D.; Qamar, A.; Fowlkes, J. B.; Bull, J. L., *Soft Matter* **2011,** 7, 4009-4016.

50. Kripfgans, O. D.; Fowlkes, J. B.; Miller, D. L.; Eldevik, O. P.; Carson, P. L., *Ultrasound Med. Biol.* **2000,** 26, 1177-1189.

51. Lo, A. H.; Kripfgans, O. D.; Carson, P. L.; Rothman, E. D.; Fowlkes, J. B., *IEEE Transactions on Ultrasonics, Ferroelectrics and Frequency Control* **2007,** 54, 933-946.

52. Noveck, R. J.; Shannon, E. J.; Leese, P. T.; Shorr, J. S.; Flaim, K. E.; Keipert, P. E.; Woods, C. M., *Anesthesia & Analgesia* **2000,** 91, 812.

53. Castro, C. I.; Briceno, J. C., *Artificial Organs* **2010,** 34, 622-634.

54. Le, T. D.; Weers, J. G., *The Journal of Physical Chemistry* **1995,** 99, 6739-6747.

55. Borkent, B. M.; Arora, M.; Ohl, C. D.; De Jong, N.; Versluis, M.; Lohse, D.; MoRch, K. A.; Klaseboer, E.; Khoo, B. C., *Journal of Fluid Mechanics* **2008,** 610, 157-182.

56. Wirde, M.; Gelius, U.; Nyholm, L., *Langmuir* **1999,** 15, 6370-6378.

57. Mezyk, S. P., *J. Phys. Chem.* **1995,** 99, 13970-13975.

58. Paxton, W. F.; Sen, A.; Mallouk, T. E.; *Chem. Eur. J.* **2005***, 11*, 6462-6470.

Chapter 5 Conclusions and Future Directions

Nano/microscale motors continue to possess great potential for a large variety of biological applications ranging for *in vitro* bio-molecular isolation/detection to targeted cellular delivery. New motion-driven sensing protocols, based on different biomolecular interactions and motion transduction principles, are expected in the near future. For example, novel motion-based biosensing platforms, involving the displacement of a nanomotor tracer, could lead to a dramatically amplified signal readout mechanism for ultrasensitive biomarker detection. Here, the recognition event would trigger the release and movement of a surface-tethered nanomotor, potentially offering the detection of single-binding events. The motion-based signal transduction could thus be readily extended to the detection of a broad range of target biomolecules in connection to different biomolecular interactions and motion transduction principles

While the micromachine target isolation concept has been illustrated using DNA, proteins and cancer cell targets, it can be further extended to additional biomaterials (bacteria, viruses) through the use of different surface-confined receptors (lectins, peptides). Recent advances in the collective behavior of multiple motors[4,5,6,9]

should also be of great interest for isolating biological targets and for multiplexing experiments. Progress in the field will likely come from integration of achievements of the latest few years into more complete and functional devices. The attractive analytical features of the new motion-driven bioassays along with the new capabilities of man-made nanomachines offer numerous opportunities in diverse areas, including biomedical diagnostics, forensic analysis, food safety or environmental monitoring. As future nanomachines become more functional and sophisticated they are expected to perform more diverse tasks and demanding activities. One such activity could be there use in treating atherosclerosis by mechanically and chemically breaking down calcified plaques. However, before nanomotor-driven, targeted drug delivery or nanosurgeries become a reality, there is a need development of more biocompatible, powerful, and externally controllable microscale objects.

There are however a few specific biological applications that are worth investigating in the near future:

(1) Modeling of micromotor convective flows to enhance and optimize binding of target cells and biological analyte.

(2) The use of collective behavior for the development of smarter micromachines for autonomous delivery and target analysis.

(3) New nanomotor-based delivery schemes for gene therapy and stem cell delivery.

(4) Ultrasound-triggered microbullets as an alternative treatment for to Bacillus of Calmette and Guerin (BCG) treatment of bladder cancer.

5.1 Modeling of Micromotor Bioisolation

One of the major challenges of current micromotor bio-isolation events is obtaining predictable results. Therefore, one major step moving forward would be to attempt to model the fluid flow behavior around the micromotors to determine the likely-hood of nucleic acid, proteins, and cellular binding events. One way to do that would be to use afluid analysis software such as Comsol Reactions Engineering Lab. Some assumptions when programming the model would be that the microrockets are cylinders, bubbles are exiting at the same speed as the rocket and the formation and dissolution rate are the same, and the graph is symmetrical. We would also want to consider using a transient moving mesh algorithm when running Stoke's flow analysis for the moving microrocket and bubble objects in a stationary, no velocity, no stress, open boundary subdomain. By putting the average velocity on the microrockets and exponentially decaying the bubbles speed over 1.5 microrocket body lengths (as observed in experiments), one could then visualize the movement of the micromotor in a static fluid (Figure 5.1). It is important to note that the bubble formation rate is equal to the dissolution rate and is originating from the back of the microengine, making it appear that a constant stream of bubbles is coming from and traveling with the microengine, which is what is typically observed. Two major challenges with this software that need to be considered is the limitation of the computing power after 0.3 seconds and the inherit emphasis on an incompressible fluid which causes unrealistic effects on the fluid properties far away from the microrocket. Additional assumptions and/or more advanced modeling software maybe required to make a realistic model to

understand the optimum conditions for nanomotor-based, bioisolation assays. A few things to understand would be the role that the microrocket size, microrocket speed, type of bubble spray (single bubble vs. spray), and fluid conditions have on enhancing cellular or biomolecular pickup. It would also be interested to understand optimum locations along the rocket length for pickup, and if pickup in one location enhances or hinders pickup in another location along the microrocket. These simple modeling assumptions are necessary to move forward with the nanomotor-based isolation assays shown in Chapter 3.

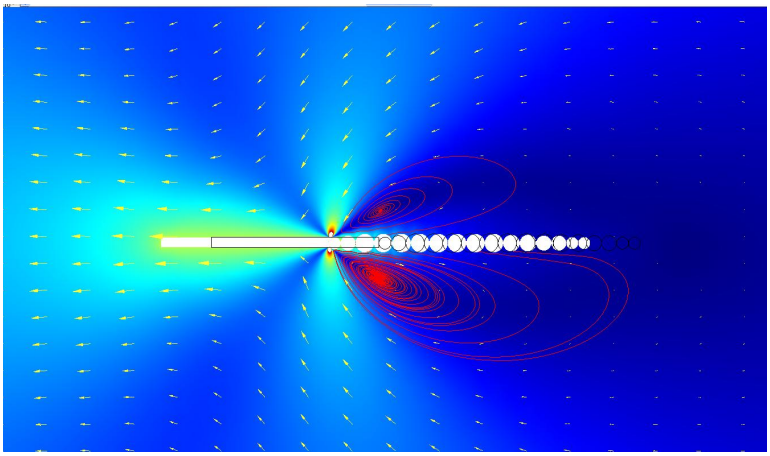

Figure 5.1 An example of a Comsol converged output for a 50 µm long microrocket traveling at 150 µm/s in water with microbubbles extending 1.5 body length from the tail of the microrocket whose speed exponentially decay from a speed equal and opposite to the microrocket. The transient figure shows the microbullet travel 16 µm in 0.3 seconds. Random fluid lines outline the turbulent flow created from the expulsion of the microbubbles from the back of the microrocket. Red indicates areas of highest fluid speed in the model, which occur at the front of the microrocket and where the bubbles are ejecting from the microbullet.

5.2 Nanomotor Collective Behavior

The collective behavior of animals, such as the swarming of bees or schooling of fish, is widely observed in nature. Inspired by animal interactions, the autonomous movement and collective behavior of synthetic nanomaterials are of considerable interest as they have implications for the future in nanomachinery, nanomedicine, and chemical sensing.[1-6] Recently, Whitesides and co-workers[5] illustrated macroscale self-assembly of self-propelled hemicylindrical plates induced through capillary and chiral interactions. Sen et al. and Mallouk and co-workers examined the microfluidic, electrokinetic pumping of tracer particles on bimetallic (Au/Ag or Au/Pd) surfaces as a result of the catalytic decomposition of hydrogen peroxide or hydrazine fuels.[4,7-11] The same groups recently exploited a light-induced self-diffusiophoresis phenomenon for the schooling of inert SiO_2[6] or AgCl[7-11] particles and for the propulsion of TiO_2 and SiO_2/TiO_2 Janus particles.[12] These recent examples indicate the potential to induce swarming of synthetic micro-objects outside living systems.

We have previous shown the ability to organize Au microparticles (Au MPs) in discrete regions by using an electrolyte gradient triggered by adding hydrazine to a hydrogen peroxide solution. We illustrate that the size and shape of the Au MP swarms and the rate of such school formations can be tailored by modifying the catalytic gold surface (with different alkanethiols) or by controlling the MP concentration. This chemically triggered particle organization can also be reversed and repeated through subsequent additions of hydrazine. A hypothetical model for a diffusiophoretic swarming mechanism that is supported by the observed aggregation

behavior of Au MPs. Overall, the observed aggregation is both scalable and versatile enough to be expanded into using biological redox species for the purpose of creating 'intelligent' artificial nanomachines.

Unlike earlier light-driven diffusiophoretic swarming[5-13] (involving particle degradation into ions and radicals), the presented chemically induced swarming is the first to rely on intact, monocomponent Au MPs to catalyze redox reactions. Au MPs in a hydrogen peroxide solution, spiked with hydrazine, move autonomously at speeds up to 16 μm/s. This autonomous motion is caused by the localized electrolyte gradient, which results from the diffusion of ionic species generated from the surface-catalyzed decomposition of hydrazine and hydrogen peroxide. Such a triggered reaction and electrolyte gradient[5-14] leads to a temporal and spatial organization of Au MPs. Figure 5.2 displays time-lapse images showing the gradual formation of Au MP swarms in response to the addition of hydrazine. The electrolyte gradient instantly leads to the formation of small (ca. 5 μm) Au MP clusters within 1 second (Figure 5.2b). The initial formation of 'nuclei' particle clusters draw in neighboring particles to form small swarms which are approximately 15–25 μm wide (Figure 5.2 c). As seen in Figure 5.2d,e these clusters continuously draw in more particles, resulting in larger schools that are hundreds of microns in diameter. Smaller swarms are attracted to larger ones, which are expected to produce significantly more ions and hence a larger electrolyte gradient.

The chemically triggered swarming of Au MPs results from the diffusion of ionic products from the catalytic Au surface. The reaction between H_2O_2 and

hydrazine catalyzed by the gold surface generates H^+, $N_2H_5^+$, and OH^- ions.[15] In any given direction, the diffusion rate of these ionic products ($D_{H^+} = 9.311\times10^{-5}$ cm^2 s^{-1}, $D_{OH^-} = 5.273\times10^{-5}$ cm^2 s^{-1}, and $D_{N2H5+} = 1.571\times10^{-5}$ cm^2 s^{-1}) vary relative to each other, thereby forming an electric field.[6,12] From a mechanistic point of view, we speculate that the resulting electric field acts phoretically on the nearby Au MPs, pulling the particles towards the center of the swarms, where the largest electrolyte gradient exists. This field also acts electroosmotically on the nearby walls of the glass slide, resulting in the micropumping of fluids towards the ion-producing Au MPs using a diffusiophoretic mechanism. A rapid decrease of the pH value from 7.6 to 5.8 is observed (within 4 min) in the presence of these MPs, compared to the minimal change (from 7.6 to 7.4) in their absence suggests that the Au acts as catalyst. This was confirmed, when testing the scalability of this diffusiophoretic phenomenon by monitoring the defined swarming of Au MPs and "inert" silica particles around large 100 μm patterned gold disks. Further, functionalizations of the Au surfaces were used to fine-tune the process, leading to tighter, faster, or delayed swarming.

In summary, the swarming behavior of Au MPs in response to chemical stimuli is an example of the smart behavior necessary for future biological application Such ability to organize Au MPs in discrete regions reflects the asymmetric movement of ionic reaction products generated ("secreted") at the Au catalyst surface and the resulting electrolyte gradient. The size and shape of the metal MP swarms can be controlled by modifying the particle surface (with different alkanethiols) or by controlling the density of particles. The swarming of the Au MPs can be reversed

(with defined transitions between the dispersed and grouping states) through repetitive hydrazine additions. Furthermore, we show that these behaviors work on both the micro- and macroscale. This swarming phenomenon can be used to model the collective behavior of future nanomachines or nanosized objects in connection with other redox species and catalytic particles. One could image the use nanoparticles with enzymes to catalyze similar reaction for *in vivo* applications. It is important to note however, that such reactions would be limited by ionic shielding so such dramatic effects as seen here would likely not be feasible. Regardless, the ability to regulate the collective behavior of synthetic microscale particles (by controlling the surface coating) is promising for the creation of 'intelligent' nanomachines that perform collective tasks.

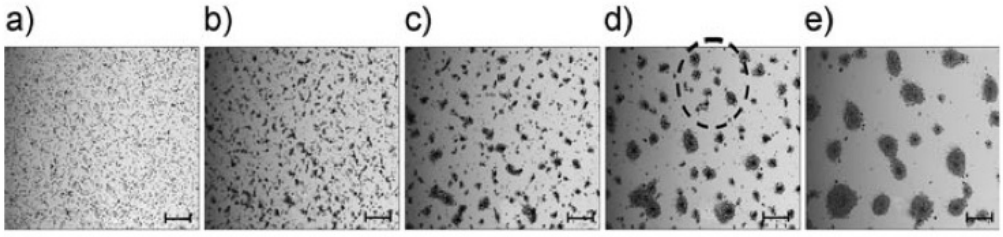

Figure 5.2 Chemically triggered time-dependent organization of Au MPs. Time-lapse optical microscope images demonstrating chemically hydrazine induced swarming behavior of unmodified Au MPs (5 mg mL^{-1}) in a 10 % H_2O_2 aqueous solution. a) Without hydrazine and (b–e) for different times after adding hydrazine: b) 1 s, c) 5 s, d) 10 s and e) 30 s. Scale bar, 50 μm. The dynamic merging of smaller schools is presented in the circled area.

5.3 Targeted Stem Cell Differentiation

In addition to targeted drug delivery, one could image using nano/microscale motors to promote stem cell differentiation. Currently, little is known regarding the impact of localized stimuli on differentiation. Mechanical forces applied to embryonic stem-cell cultures may have the ability to drastically influence the structures' differentiation process.[16] It is known that prolonged microscale stresses on a cellular membrane can promote certain cellular differentiation. Some examples include: cyclic mechanical strain (40min and 2000 microstrains) of rat Mesenchymal Stem Cells (MSCs) induces osteogenic differentiation,[17] 72 hours of a 1 Hz, 30% strain stimulating MSCs to increase proliferation and secrete angiongeic factors,[18] and cyclic loading of mouse MSCs leading to differentiated, fibroblast-like cells[19]. One could image the use magnetically rotating or constantly moving nanoscale objects to target and mechanically differentiated adult stem cells for cell replacement or gene therapy schemes. Nanomotors for the application of local, temporarily and spatially controlled forces onto the cell. Fibronectin functionalized nanomotors would drive to a target MSC using magnetic guidance, bind to cellular surface markers, and would continue to apply cyclic mechanical stains will still under a magnetically field. Some challenges for this technique include the use of completely biocompatible nano-propulsion devices, a controlled method for directing the motors to the stem cells, ensuring that the nanomotor or a collective group can provide the necessary force to promote stem cell differentiation, and understanding the effect of the external magnetic field on the global cellular behavior.

A second scheme for stem cell differentiation, Figure 5.3, could include the use of nano/microscale motors to locally direct and concentrate the differentiation factors that are being released from bound PLGA particles; thereby, targeting individual cells growing in normal environments. The main experiment would be to chemically differentiate cells on a localized level. Motors could transport the differentiation factors via bound magnetically PLGA carrying devices or one could electrostatically stack PLGA particles by adding alternating layers of positive and negatively charged particles. To incorporate the hydrophillic differentiation factor a double emulsion technique could be utilized.[20] The key challenge here is how much differentiation factor can be loaded into the PLGA particles and onto the nanomotors. Additionally, one needs to be concerned with matching the differentiation factor release rate of the PLGA carriers with that of the stem cell differentiation profile. However, the advantage of this method is the ability to locally differentiate a cell, something that is currently a major challenge when translating current *in vitro* petri dish approaches to *in vivo* studies. Therefore, an interesting study would be having two wires with differently-loaded PLGA particles, differentiate two MSCs into different cell morphologies. This study would be facilitated by the nanomotors ability to travel and target specific cells for individual cellular differentiation.

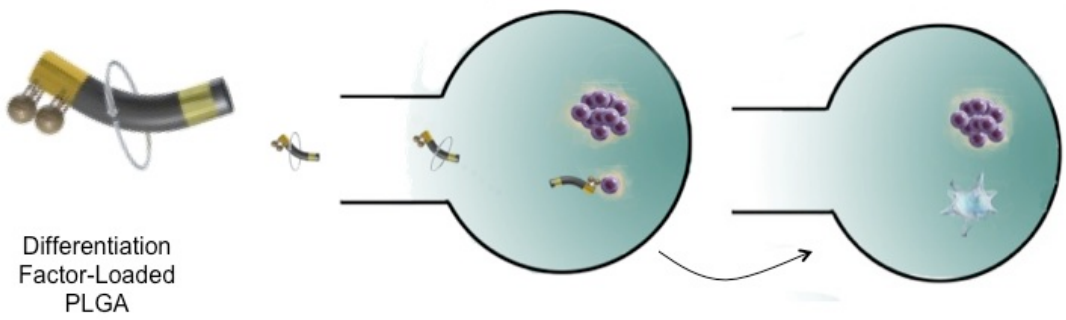

Figure 5.3 The schematic depicts, nanomotor based stem cell differentiation as the magnetically propelled nanomachine travels to a Mesenchymal stem cell. The microrocket has be functionalized to carry PLGA particles carrying selective differentiation factors, thereby differentiating the cell over time.

5.4 Ultrasound Triggered Microbullets for Bladder Cancer Treatment

Externally triggered micro/nanoscale propulsion devices (NMSPDs) hold great promise for a variety of *in vivo* or *in vitro* biomedical applications, such as - but not limited to - targeted drug delivery, circulating gene gun regulation, tissue penetration for triggering immune responses, and micro-tissue removal or cleaning schemes. One major advantage over biological based approaches is that these synthetic micromachines are easily functionalizable, durable, and predictable than biological systems. Additionally, these ultrasound triggered NMSPDs possess the ultra high power and force to penetrate farther and quicker than some diffusion based approaches. As previously, mentioned one example of a biological tissue penetration system is as a substitute for current BCG treatments for bladder cancer patients. For this application, multiple NMSPDs can be fired into the surrounding bladder cancer area to promote a natural inflammatory response to fight the cancer cells. It is very likely that such synthetic treatments may lead to fewer treatments as their presence maybe sustainable. Additionally, many bacteria related side effects such as sepsis will no longer be of concern. Other potential applications include NMSPD sampling by externally triggered devices, microclotting tissue clotting, and of course targeted therapies involving for gene, cellular, nucleic acid, protein, antigen or drug delivery.

An example of a direct future application of these NMSPDs could be as a substitute to Bacillus of Calmette and Guerin (BCG) treatment for bladder cancer

patients. Currently, every year about 13000 patients in the USA will die of bladder cancer. Although typically diagnosed in its early superficial stage as a result of microscopic blood in the urine, the disease has an overall 65% recurrence rate and 30% progression rate, often requiring patients to seek continuous treatment and periodic internal inspections of their bladders[21]. The use of BCG as an intravesical instillation treatment for bladder cancer patients, became widely accepted in 1980 when a controlled study by the Southwest Oncology Group showed that the treatment drastically reduced recurrence rates due to the natural inflammatory response triggered by the BCG bacteria burrowing into the cancerous bladder lining. This immunoprophylactic agent has shown a 50–60% effectiveness against small residual tumors and 70% of patients sustain remission for over 5 years[21]. This treatment however has shown to cause many side effects and the BCG reponse is unpredictable. In general, almost all patients (95%) report dysuria, and many experience hematuria (39%), fever (22%) and nausea (22%)[22]. Life threatening side effects can occur and include BCG sepsis, in which the bacteria infection spreads throughout the body via the bloodstream[23].

Therefore one potential important application of externally triggered micro/nanomaterials would be to modify them with biological antigens (nucleic acids, proteins, etc.) to develop biosynthetic hybrid materials that can similarly act as immunoprophylactic agents. We have already shown that multiple NMSPDs can fire into tissue sections. Previous studies using micromachines for isolation have also shown their capability to be readily modified with biomolecules. Multiple NMSPDs

could therefore be injected and fired into the surrounding bladder cancer area to promote a natural inflammatory response to fight the cancer cells. It is very likely that such synthetic treatments may lead to fewer treatments as their presence maybe more sustainable within the tissue. Additionally, many bacteria related side effects such as sepsis could potentially be eliminated by this technology. This specific example is just one application that externally triggered fuel containing materials can provide. We can also imagine micromachine sampling by ultrasound triggered devices, microclotting tissue clotting, and of course targeted therapies involving for gene, cellular, nucleic acid, protein, antigen or drug delivery.

Chapter 5 is part based in on the material as it appears in Angewandte Chemie, 2011, by Daniel Kagan, Shankar Balasubramanian, and Joseph Wang, and in part based on material submitted to Nature Nanotechnology, 2012, by Daniel Kagan, Mike Benchimol, Jonathan Claussen, Beke Chuluun-Erdene, Sadik Esenser, and Joseph Wang. The dissertation author was the primary investigator and co-author of these papers.

5.5 References

1. Mallouk, T. E.; Sen, A. *Sci. Am.* **2009***, 300*, 72–77.

2. Wang, J. *ACS Nano* **2009***, 3*, 4–9.

3. Y. Hong, D. Velegol, N. Chaturvedi, A. Sen, *Phys. Chem. Chem. Phys.* **2010***, 12*, 1423–1435.

4. Sen, A.; Ibele, M.; Hong, Y.; Velegol, D.. *Faraday Discuss.* **2009***, 143*, 15–27.

5. Ismagilov, R. F.; Schwartz, A.; Bowden, N.; Whitesides, G. M.; *Angew. Chem.* **2002***, 114*, 674–676.

6. Ibele, M.; Mallouk, T. E.; Sen, A. *Angew. Chem.* **2009***, 121*, 3358–3362.

7. Kline, T. R.; Paxton, W. F.; Wang, Y.; Velegol, D.; Mallouk, T. E.; Sen, A. *J. Am. Chem. Soc.* **2005***, 127*, 17150-17151.

8. Kline, T. R.; Iwata, J.; Lammert, P. E.; Mallouk, T. E.; Sen, A.; Velegol, D. *J. Phys. Chem. B* **2006***, 110,* 24513–2452.

9. Ibele, M.; Wang, Y.; Kline, T. R.; Mallouk, T. E.; Sen, A. *J. Am. Chem. Soc.* ***2007****, 129*, 7762–7763.

10. Hong, Y.; Blackman, N. M.; Kopp, N. D.; Sen, A.; Velegol, D. *Phys. Rev. Lett.* **2007***, 99*, 178103.

11. Ibele, M.; Lammert, P. E.; Crespi, V. H.; Sen, A. *ACS Nano* ***2010***, *4,* 4845–4851.

12. Hong, Y.; Diaz, M.; Cordova-Figueroa, U. M.; Sen, A. *Adv. Funct. Mater.* **2010***, 20,* 1–9.

13. Chaturvedi, N.; Hong, Y.; Sen, A.; Velegol, D. *Langmuir* **2010***, 26,* 6308–6313.

14. Howse, J. R.; Jones, R. A. L.; Ryan, A. J.; Gough, T.; Vagabakhsh, R.; Golestanian, R. *Phys. Rev. Lett.* **2007**, *99,* 048102.

15. Audrieth, L. F.; Ogg B. A.; *The Chemistry of Hydrazine*; Wiley: New York, 1951; pp. 115–145.

16. Chowdhury, F; Na, S.; Li, D.; Poh, Y.C; Tanaka, T.S.; Wang, F.; Wang, N. *Nature Materials*, **2010**, *9*, 82-88.

17. Qi, M.C.; Hu, J.; Zou, S.J.; Chen, H.Q.; Zhou, H.X.; Han. L.C. *International Journal of Oral and Maxillofacial Surgery*, **2008**, *37*, 453-458.

18. Kasper, G.; Dankert, N.; Tuischer, J.; Hoeft, M.; Gaber, T.; Glaeser, J. D.; Zander, D.; Tschirschmann, M.; Thompson, M.; Matziolis, G; Duda, G. N. *Stem Cells,* **2007***, 25*, 903–910.

19. Sarraf, C. E.; Otto, W. R.; Eastwood, M.; *Cell Proliferation,* **2011***, 44,* 99–108.

20. Sela, E.C; Chorny, M.; Koroukhov, N.; Danenberg, H.D.; Golomb, G. *Journal of Controlled Release* **2009***, 133*, 90-95.

21. Alexandroff, A.; Jackson, A.; O'Donnell, M.A.; James, K.; *Lancet.* **1999,** *353* 1689-1694.

22. Lamm, D.L.; Thor, D.E.; Harris., S.C.; Reyna, J.A.; Stogdill, V.D.; Radwin, H.M.; *J. Urol.* **1990***, 124,* 38-40.

23. Lamm, D.L.; van der Meiiden, P.M.; Morales, A.; Brosman, S.A.; Catalona, W.J.; Herr, H.W.; Soloway, M.S.; Steg, A.; Debruvne, F.M.; *J. Urol.* **1992**, *147*, 596-60